Title
Development of and Therapeutic Applications for Novel Inhibitors of Deoxycytidine Kinase

Author
Armijo, Amanda Lee

Publication Date
2014

Peer reviewed|Thesis/dissertation

UNIVERSITY OF CALIFORNIA

Los Angeles

Development of and Therapeutic Applications for Novel Inhibitors of Deoxycytidine Kinase

A dissertation submitted in partial satisfaction of the requirements for the degree

Doctor of Philosophy in Molecular and Medical Pharmacology

by

Amanda Lee Armijo

2014

ABSTRACT OF THE DISSERTATION

Development of and Therapeutic Applications for

Novel Inhibitors of Deoxycytidine Kinase

by

Amanda Lee Armijo

Doctor of Philosophy in Molecular and Medical Pharmacology

University of California, Los Angeles, 2014

Professor Caius G. Radu, Chair

Deoxycytidine kinase (dCK), a rate-limiting enzyme in the deoxyribonucleotide salvage pathway, participates in the production of deoxyribonucleoside triphosphates (dNTPs). dCK is highly expressed in hematopoietic tissues and many cancers. In addition, dCK is responsible for the phosphorylation, and thus activation of several antiviral and anticancer nucleoside analog pro-drugs. Austin, Toy, and colleagues have demonstrated that dCK deficient mice (*dCK*$^{-/-}$) have severe developmental defects of the lymphoid and hematopoietic progenitor cells, indicating that dCK is pivotal for their normal development. Further study of the T, B, and erythroid lineages revealed nucleotide pool imbalances resulting in replication stress and cell cycle arrest in the early stages of DNA replication. Dual inactivation of both dCK and thymidine kinase 1 (TK1) *in vivo* supported our hypothesis that salvage of thymidine by TK1 was responsible for the allosteric block of the *de novo* pathway enzyme, ribonucleotide

reductase, consequentially perturbing the nucleotide pools. These findings and the role of dCK in cancer led to our interest in developing a small molecule inhibitor. Positron Emission Tomography and the dCK-specific substrate, ^{18}F-L-1-(2′-deoxy-2′-F luoroarabinofuranosyl) Cytosine, proved useful in the quick identification of top performing dCK inhibitors *in vivo*. Following a high throughput screen and a structure-activity relationship study we successfully identified high potency small molecule inhibitors of dCK (dCKi) (IC_{50} = ∼1−12 nM). The combination of the dCKi with pharmacological perturbations of *de novo* dNTP synthesis, via thymidine, in acute lymphoblastic leukemia cells depletes deoxycytidine triphosphate pools leading to DNA replication stress, cell cycle arrest, and apoptosis *in vivo*, without detectable toxicity to normal tissues. The results from our studies further our understanding of nucleotide metabolism in normal hematopoiesis and hematological malignancies, and identify dCK as a new therapeutic target in hematological malignancies.

The dissertation of Amanda Lee Armijo is approved.

Anastassia Alexandrova

Robert Michael van Dam

Johannes Czernin

Caius G. Radu, Committee Chair

University of California, Los Angeles

2014

DEDICATION

To my parents, Donna and Corky, my siblings, Kristen and JR, and my grandparents, Joe and Nellie, for all the unconditional love and support they have given me throughout the years. Mom and Dad, I will forever be grateful for your advice, encouragement, and patience.

To my best friend, Wayne, for always believing in me, even when I didn't believe in myself.

TABLE OF CONTENTS

LIST OF FIGURES AND TABLES

Chapter 1

Chapter 2

Chapter 3

Chapter 4

ACKNOWLEDGEMENTS

I would first like to thank Dr. Caius Radu for his continued support throughout my graduate career. I would equally like to thank Dr. Johannes Czernin for his continued optimism and support since my undergraduate days at UCLA.

I would also like to thank the members of my doctoral committee: Dr. Anastassia Alexandrova, and Dr. Michael van Dam for their patience, time, and support.

I would like to thank all the members of the Radu/Czernin laboratory, both past and present, for all their assistance and friendship throughout the years. I am extremely grateful to the efforts of Dr. Wayne Austin, Dr. Dean Campbell, Dr. David Nathanson, Dr. Alfred Lee, Dr. Zheng Li, Dr. Jue Wang, and Raymond Gipson. Without all of your help, the work presented in this dissertation would not have been possible to generate.

I would also like to thank our collaborators Dr. Nagichettiar Satyamurthy, Dr. Michael Jung, Dr. Robert Damoiseaux, and Dr. Arnon Lavie for their valuable insight, assistance, and advice regarding the dCK inhibitor project.

I would like to thank Dr. Liu Wei, Larry Pang, Dr. Jason Lee, and Dr. Saman Sadeghi for their help in executing the mPET/CT imaging studies.

I would like to thank Dr. Helen Su and Dr. Wolfgang Weber for all of your patience and inspiration during the earliest stages of my scientific career.

Chapter 2 is a version of Austin, W.R., A.L. Armijo, D.O. Campbell, A.S. Singh, T. Hsieh, D. Nathanson, H.R. Herschman, M.E. Phelps, O.N. Witte, J. Czernin, and C.G. Radu. (2012). Nucleoside salvage pathway kinases regulate hematopoiesis by linking nucleotide metabolism with replication stress. *The Journal of Experimental Medicine* 209:2215-2228.

Chapter 3 is a version of A.L. Armijo, Murphy, J.M., J. Nomme, C.H. Lee, Q.A. Smith, Z. Li, D.O. Campbell, H.I. Liao, D.A. Nathanson, W.R. Austin, J.T. Lee, R. Darvish, L. Wei, J. Wang, Y. Su, R. Damoiseaux, S. Sadeghi, M.E. Phelps, H.R. Herschman, J. Czernin, A.N. Alexandrova, M.E. Jung, A. Lavie, and C.G. Radu. (2013). Development of new deoxycytidine kinase inhibitors and noninvasive in vivo evaluation using positron emission tomography. *Journal of Medicinal Chemistry* 56:6696-6708.

Chapter 4 is a version of Nathanson, D.A., A.L. Armijo, M. Tom, Z. Li, E. Dimitrova, W.R. Austin, J. Nomme, D.O. Campbell, L. Ta, T.M. Le, J.T. Lee, R. Darvish, A. Gordin, L. Wei, H.I. Liao, M. Wilks, C. Martin, S. Sadeghi, J.M. Murphy, N. Boulos, M.E. Phelps, K.F. Faull, H.R. Herschman, M.E. Jung, J. Czernin, A. Lavie, and C.G. Radu. (2014). Co-targeting of convergent nucleotide biosynthetic pathways for leukemia eradication. *The Journal of Experimental Medicine* 211:473-486.

Finally, I would like to acknowledge my funding through the Eugene V. Cota-Robles Fellowship at UCLA.

VITA

2008	B.S., Microbiology, Immunology, and Molecular Genetics University of California, Los Angeles
2008-10	Staff Research Associate University of California, Los Angeles Los Angeles, CA
2010	Eugene V. Cota-Robles Fellowship Awardee University of California, Los Angeles

PUBLICATIONS

Nathanson, D.A., **A.L. Armijo**, M. Tom, Z. Li, E. Dimitrova, W.R. Austin, J. Nomme, D.O. Campbell, L. Ta, T.M. Le, J.T. Lee, R. Darvish, A. Gordin, L. Wei, H.I. Liao, M. Wilks, C. Martin, S. Sadeghi, J.M. Murphy, N. Boulos, M.E. Phelps, K.F. Faull, H.R. Herschman, M.E. Jung, J. Czernin, A. Lavie, and C.G. Radu. (2014). Co-targeting of convergent nucleotide biosynthetic pathways for leukemia eradication. *The Journal of Experimental Medicine* 211:473-486.

Nomme, J., J.M. Murphy, Y. Su, N.D. Sansone, **A.L. Armijo**, S.T. Olson, C. Radu, and A. Lavie. (2014). Structural characterization of new deoxycytidine kinase inhibitors rationalizes the affinity-determining moieties of the molecules. *Acta Crystallographica. Section D, Biological crystallography* 70:68-78.

A.L. Armijo*, Murphy, J.M.*, J. Nomme*, C.H. Lee, Q.A. Smith, Z. Li, D.O. Campbell, H.I. Liao, D.A. Nathanson, W.R. Austin, J.T. Lee, R. Darvish, L. Wei, J. Wang, Y. Su, R. Damoiseaux, S. Sadeghi, M.E. Phelps, H.R. Herschman, J. Czernin, A.N. Alexandrova, M.E. Jung, A. Lavie, and C.G. Radu. (2013). Development of new deoxycytidine kinase inhibitors and noninvasive in vivo evaluation using positron emission tomography. *Journal of Medicinal Chemistry* 56:6696-6708. (*denotes equal contribution)

Austin, W.R., **A.L. Armijo**, D.O. Campbell, A.S. Singh, T. Hsieh, D. Nathanson, H.R. Herschman, M.E. Phelps, O.N. Witte, J. Czernin, and C.G. Radu. (2012). Nucleoside salvage pathway kinases regulate hematopoiesis by linking nucleotide metabolism with replication stress. *The Journal of Experimental Medicine* 209:2215-2228.

Ng, Q.K., H. Su, **A.L. Armijo**, J. Czernin, C.G. Radu, and T. Segura. (2011). Clustered Arg-Gly-Asp peptides enhances tumor targeting of nonviral vectors. *ChemMedChem* 6:623-627.

Ferl, G.Z., R.A. Dumont, I.J. Hildebrandt, **A. Armijo**, R. Haubner, G. Reischl, H. Su, W.A. Weber, and S.C. Huang. (2009). Derivation of a compartmental model for quantifying 64Cu-DOTA-RGD kinetics in tumor-bearing mice. *Journal of Nuclear Medicine : official publication, Society of Nuclear Medicine* 50:250-258.

Wang, H., S. Wang, H. Su, K.J. Chen, A**.L. Armijo**, W.Y. Lin, Y. Wang, J. Sun, K. Kamei, J. Czernin, C.G. Radu, and H.R. Tseng. (2009). A supramolecular approach for preparation of size-controlled nanoparticles. *Angewandte Chemie* 48:4344-4348.

CHAPTER 1:

Introduction

Production of nucleotides for DNA synthesis via two connected pathways

Mammalian cells require a balanced supply of building blocks in order to support replication and repair of the genome. There are two major pathways responsible for the generation of such precursors: the *de novo* pathway that generates nucleotides from glucose and amino acids; and the salvage pathway that recycles nucleosides present in the extracellular environment (Reichard, 1988) (Figure 1.1). These pathways are not independent of one another as they share intermediates and products. In addition, the activity of one pathway can influence the activity of the other (Reichard, 1988).

Regulation of the de novo synthesis pathway by ribonucleotide reductase

De novo synthesis of pyrimidine deoxyribonucleotides (dNTPs) begins with the transport and subsequent phosphorylation of glucose into glucose-6-phosphate, which is then converted into 5-phosphoribosyl-1-pyrophosphate (PRPP). The pyrimidine base, orotate, formed from glutamine and aspartate, combines with PRPP and decarboxylation of the product generates the pyrimidine precursor uridine monophosphate (UMP) (Evans and Guy, 2004; Jones, 1980). UMP can be phosphorylated to uridine diphosphate (UDP) (Van Rompay et al., 2001), a substrate for the enzyme ribonucleotide reductase (RNR) (Reichard, 1988). RNR reduces UDP to deoxyuridine diphosphate (dUDP), which can then be converted into thymidine triphosphate (dTTP) by thymidylate synthase. RNR can also convert cytidine diphosphate (CDP) into deoxycytidine diphosphate (dCDP) following the conversion of UDP into CDP. Subsequent phosphorylation of dCDP contributes to the deoxycytidine triphosphate (dCTP) pools.

RNR has the ability to catalyze the reduction of all four NTP substrates to their dNTP forms (Reichard, 1988). The enzymatic activity and substrate specificity of RNR is highly regulated. Allosteric control of RNR enables the single enzyme to provide a balanced supply of all four dNTPs required to maintain genomic integrity in all cells (Nordlund and Reichard, 2006). RNR contains two distinct allosteric sites both of which are located on the regulatory subunit, ribonucleotide reductase M1 (RRM1): the activity regulation site binds adenosine triphosphate (ATP) to activate the enzyme or deoxyadenosine triphosphate (dATP) to inhibit it; the specificity regulation site binds effectors one at a time and determines the specific nucleotide substrate (Nordlund and Reichard, 2006).

RRM1 is expressed throughout the cell cycle and two units of RRM1 bind to two units of the enzymatic subunit ribonucleotide reductase M2 (RRM2) upon RRM2 transcription and translation during the S-phase of the cell-cycle to form a complete multi-subunit RNR complex (Fairman et al., 2011). RRM1 can also pair with the p53-inducible ribonucleotide reductase M2 B (RRM2B) in the presence of DNA damage (Kolberg et al., 2004). Binding of dNTPs to the specificity regulation site promotes reduction of NDPs at the catalytic site on the enzymatic subunit of RNR. Binding of ATP or dATP promotes reduction of the pyrimidines CDP and UDP, whereas binding of dTTP activates guanine diphosphate (GDP) reduction, while inhibiting CDP reduction. Binding of deoxyguanosine triphosphate (dGTP) promotes reduction of adenosine diphosphate (ADP) and GDP, while inhibiting reduction of CDP and UDP (Logan, 2011). dCTP has no effect on the catalytic activity of RNR (Chimploy and Mathews, 2001).

The nucleoside salvage pathway and deoxycytidine kinase

Salvage of extracellular nucleosides is catalyzed by the cytosolic enzymes deoxycytidine kinase (dCK) and thymidine kinase 1 (TK1) (Arner and Eriksson, 1995). dCK catalyzes the phosphorylation of many substrates, including deoxycytidine (dC), deoxyguanosine (dG), and deoxyadenosine (dA) (Reichard, 1988). Subsequent phosphorylation of the monophosphate nucleotides to their corresponding di- and triphosphate forms are catalyzed by other kinases (Krishnan et al., 2003; Pasti et al., 2003). In addition, dCK is responsible for the phosphorylation of several antiviral and anticancer nucleoside analog prodrugs (e.g. gemcitabine, cytarabine, clofarabine) required for the activation of these drugs (Van Rompay et al., 2003). Nucleotides are effectively trapped within the cell by the addition of the electronegative phosphate group covalently added by the salvage enzymes (Young et al., 2013). dCK is preferentially expressed in hematopoietic and lymphoid tissues and is required for normal hematopoietic development (Toy et al., 2010). In addition, dCK was recently implicated in the regulation of the G2/M checkpoint in cancer cells in response to DNA damage (Yang et al., 2012).

TK1 contributes to dTTP pools by catalyzing the phosphorylation of thymdine to generate thymidine monophosphate (dTMP), which is quickly phosphorylated to its triphosphate form. Binding of dTTP to the specificity site of RNR will prevents the *de novo* synthesis of dCTP (Larsson et al., 2004).

The focus of this thesis is to understand the fundamental role of dCK in DNA replication and repair, to develop a small molecule inhibitor of dCK, and to investigate the efficaciousness of the inhibitor in treating hematological malignancies.

PET imaging as a tool to monitor dCK activity in vivo

Positron emission tomography (PET) is a non-invasive *in vivo* imaging technique that is widely used in clinical oncology diagnostics and treatment monitoring (Czernin et al., 2010; Weber et al., 2008). In addition, PET can be utilized early in the drug discovery and development process to enable non-invasive evaluations of drug pharmacodynamic (PD) and/or pharmacokinetic (PK) properties, thus facilitating faster and more effective decision-making (Hargreaves, 2008). In our quest to develop a small molecule inhibitor of dCK, PET could play a particularly important role given the availability of validated PET biomarkers to assess dCK activity *in vivo*. One of these PET PD biomarkers, ^{18}F-L-1-(2'-deoxy-2'-**F**luoro**A**rabinofuranosyl) **C**ytosine (^{18}F-L-FAC), is a high affinity substrate for dCK and accumulates in tissues in a dCK-specific manner (Figure 1.2) (Shu et al., 2010).

Concluding remarks

Elucidation of the fundamental biological role of dCK in DNA replication and repair in hematopoietic tissues would provide invaluable insight into potential therapeutic applications of a small molecule inhibitor against the enzyme. Austin, Toy, and colleagues generated dCK deficient (*dCK*$^{-/-}$) mice that have a profound phenotype in which the erythroid and lymphoid development are severely impacted, thus demonstrating that dCK plays a critical role in normal hematopoietic development (Toy et al., 2010). The following chapter will describe the cell cycle defects and the presence of active DNA damage responses that occurs in the hematopoietic progenitors from the *dCK*$^{-/-}$ mice. Chapter 3 will document the development of high affinity small molecule

dCK inhibitors and demonstrate their *in vivo* efficacy using ^{18}F-L-FAC PET as a non-invasive and clinically applicable PD biomarker. Chapter 4 will describe the successful use of the dCK inhibitor to eradicate tumor cells in mouse models. The final chapter will include a brief discussion of another potential clinical application of the dCK inhibitor, as well the necessary improvement of the pharmacokinetic properties of the first generation dCK inhibitors.

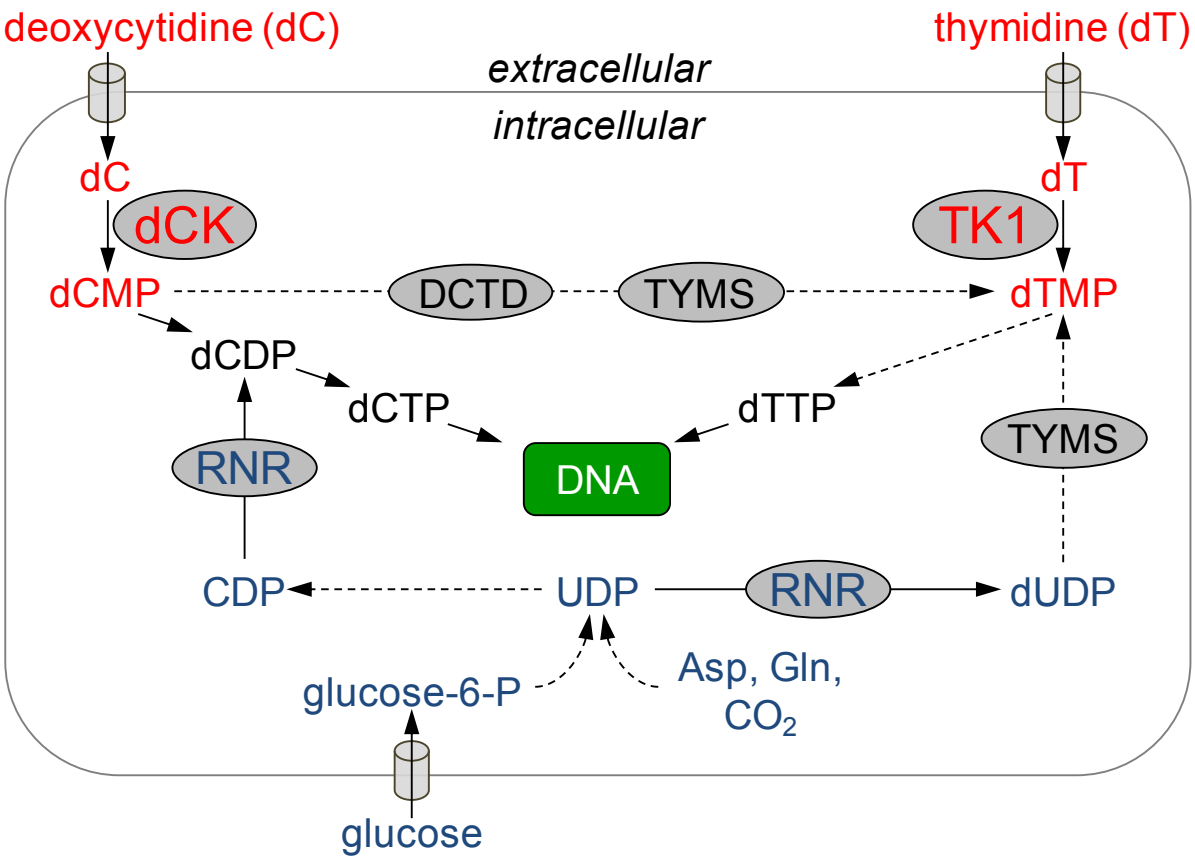

Figure 1.1 *De novo* and salvage synthesis of pyrimidine dNTPs. Schematic of the *de novo* (blue) and the salvage (red) pathway inputs into pyrimidine dNTP pools for DNA synthesis. Solid arrows indicate single-step processes; dashed arrows indicate multi-step processes with intermediates not named/depicted in the schematic. Glucose is transported and phosphorylated into glucose-6-phosphate (glucose-6-P), which can be converted into 5-phosphoribosyl-1-pyrophosphate (PRPP). Glutamine (Gln) and aspartate (Asp) contribute to the formation of the pyrimidine base orotate, which is reacted with PRPP to later form uridine monophosphate (UMP). UMP is phosphorylated once more to become uridine diphosphate (UDP), a substrate of ribonucleotide reductase (RNR). RNR converts UDP into deoxyuridine diphosphate (dUDP), which can later be converted into thymidine triphosphate (dTTP). UDP can also be converted into

cytidine diphosphate (CDP), another substrate of RNR. RNR converts CDP into deoxycytidine diphosphate (dCDP), which is then phosphorylated once more to contribute to deoxycytidine triphosphate (dCTP) pools. dCK contributes to dCTP pools by phosphorylating deoxycytidine to generate deoxycytidine monophosphate (dCMP), an intermediate that is rapidly phosphorylated twice more to generate dCTP. Thymidine kinase 1 (TK1) contributes to dTTP pools by phosphorylating thymidine to generate thymidine monophosphate (dTMP), an intermediate that is rapidly phosphorylated twice more to generate dTTP. Thymidylate synthase (TYMS), dCMP deaminase (DCTD).

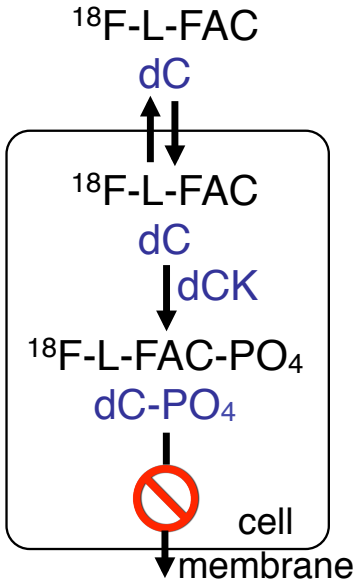

Figure 1.2 Accumulation of deoxycytidine and ^{18}F-L-FAC in dCK expressing cells. Schematic of the mechanism by which dC and ^{18}F-L-FAC accumulate in tissues in a dCK dependent manner. dC and ^{18}F-L-FAC are able to freely influx into and efflux out of the cells through facilitated transport mediated by nucleoside transporters. dCK covalently adds an electronegative phosphate group (-PO_4) preventing the nucleotide or nucleotide analog from being effluxed out of the cell.

References

Arner, E.S., and S. Eriksson. 1995. Mammalian deoxyribonucleoside kinases. *Pharmacology & therapeutics* 67:155-186.

Chimploy, K., and C.K. Mathews. 2001. Mouse ribonucleotide reductase control: influence of substrate binding upon interactions with allosteric effectors. *The Journal of biological chemistry* 276:7093-7100.

Czernin, J., M.R. Benz, and M.S. Allen-Auerbach. 2010. PET/CT imaging: The incremental value of assessing the glucose metabolic phenotype and the structure of cancers in a single examination. *European journal of radiology* 73:470-480.

Evans, D.R., and H.I. Guy. 2004. Mammalian pyrimidine biosynthesis: fresh insights into an ancient pathway. *The Journal of biological chemistry* 279:33035-33038.

Fairman, J.W., S.R. Wijerathna, M.F. Ahmad, H. Xu, R. Nakano, S. Jha, J. Prendergast, R.M. Welin, S. Flodin, A. Roos, P. Nordlund, Z. Li, T. Walz, and C.G. Dealwis. 2011. Structural basis for allosteric regulation of human ribonucleotide reductase by nucleotide-induced oligomerization. *Nature structural & molecular biology* 18:316-322.

Hargreaves, R.J. 2008. The role of molecular imaging in drug discovery and development. *Clinical pharmacology and therapeutics* 83:349-353.

Jones, M.E. 1980. Pyrimidine Nucleotide Biosynthesis in Animals: Genes, Enzymes, and Regulation of UMP Biosynthesis. *Annual review of biochemistry* 49:253-279.

Kolberg, M., K.R. Strand, P. Graff, and K.K. Andersson. 2004. Structure, function, and mechanism of ribonucleotide reductases. *Biochimica et biophysica acta* 1699:1-34.

Krishnan, P., E.A. Gullen, W. Lam, G.E. Dutschman, S.P. Grill, and Y.C. Cheng. 2003. Novel role of 3-phosphoglycerate kinase, a glycolytic enzyme, in the activation of L-nucleoside analogs, a new class of anticancer and antiviral agents. *The Journal of biological chemistry* 278:36726-36732.

Larsson, K.M., A. Jordan, R. Eliasson, P. Reichard, D.T. Logan, and P. Nordlund. 2004. Structural mechanism of allosteric substrate specificity regulation in a ribonucleotide reductase. *Nature structural & molecular biology* 11:1142-1149.

Logan, D.T. 2011. Closing the circle on ribonucleotide reductases. *Nature structural & molecular biology* 18:251-253.

Nordlund, P., and P. Reichard. 2006. Ribonucleotide reductases. *Annual review of biochemistry* 75:681-706.

Pasti, C., S. Gallois-Montbrun, H. Munier-Lehmann, M. Veron, A.M. Gilles, and D. Deville-Bonne. 2003. Reaction of human UMP-CMP kinase with natural and analog substrates. *European journal of biochemistry / FEBS* 270:1784-1790.

Reichard, P. 1988. Interactions between deoxyribonucleotide and DNA synthesis. *Annual review of biochemistry* 57:349-374.

Shu, C.J., D.O. Campbell, J.T. Lee, A.Q. Tran, J.C. Wengrod, O.N. Witte, M.E. Phelps, N. Satyamurthy, J. Czernin, and C.R. Radu. 2010. Novel PET Probes Specific for Deoxycytidine Kinase. *J. Nucl. Med.* 51:1092-1098.

Toy, G., W.R. Austin, H.I. Liao, D. Cheng, A. Singh, D.O. Campbell, T.O. Ishikawa, L.W. Lehmann, N. Satyamurthy, M.E. Phelps, H.R. Herschman, J. Czernin, O.N. Witte, and C.G. Radu. 2010. Requirement for deoxycytidine kinase in T and B lymphocyte development. *Proceedings of the National Academy of Sciences of the United States of America* 107:5551-5556.

Van Rompay, A.R., M. Johansson, and A. Karlsson. 2003. Substrate specificity and phosphorylation of antiviral and anticancer nucleoside analogues by human deoxyribonucleoside kinases and ribonucleoside kinases. *Pharmacology & therapeutics* 100:119-139.

Van Rompay, A.R., A. Norda, K. Linden, M. Johansson, and A. Karlsson. 2001. Phosphorylation of uridine and cytidine nucleoside analogs by two human uridine-cytidine kinases. *Molecular pharmacology* 59:1181-1186.

Weber, W.A., A.L. Grosu, and J. Czernin. 2008. Technology Insight: advances in molecular imaging and an appraisal of PET/CT scanning. *Nature clinical practice. Oncology* 5:160-170.

Yang, C., M. Lee, J. Hao, X. Cui, X. Guo, C. Smal, F. Bontemps, S. Ma, X. Liu, D. Engler, W.B. Parker, and B. Xu. 2012. Deoxycytidine kinase regulates the G2/M checkpoint through interaction with cyclin-dependent kinase 1 in response to DNA damage. *Nucleic acids research* 40:9621-9632.

Young, J.D., S.Y. Yao, J.M. Baldwin, C.E. Cass, and S.A. Baldwin. 2013. The human concentrative and equilibrative nucleoside transporter families, SLC28 and SLC29. *Molecular aspects of medicine* 34:529-547.

CHAPTER 2

Nucleoside Salvage Pathway Kinases Regulate Hematopoiesis by Linking Nucleotide Metabolism with Replication Stress

Abstract

Nucleotide deficiency causes replication stress (RS) and DNA damage in dividing cells. How nucleotide metabolism is regulated in vivo to prevent these deleterious effects remains unknown. In this study, we investigate a functional link between nucleotide deficiency, RS, and the nucleoside salvage pathway (NSP) enzymes deoxycytidine kinase (dCK) and thymidine kinase (TK1). We show that inactivation of dCK in mice depletes deoxycytidine triphosphate (dCTP) pools and induces RS, early S-phase arrest, and DNA damage in erythroid, B lymphoid, and T lymphoid lineages. $TK1^{-/-}$ erythroid and B lymphoid lineages also experience nucleotide deficiency but, unlike their $dCK^{-/-}$ counterparts, they still sustain DNA replication. Intriguingly, dCTP pool depletion, RS, and hematopoietic defects induced by dCK inactivation are almost completely reversed in a newly generated dCK/TK1 double-knockout (DKO) mouse model. Using NSP-deficient DKO hematopoietic cells, we identify a previously unrecognized biological activity of endogenous thymidine as a strong inducer of RS in vivo through TK1-mediated dCTP pool depletion. We propose a model that explains how TK1 and dCK "tune" dCTP pools to both trigger and resolve RS in vivo. This new model may be exploited therapeutically to induce synthetic sickness/lethality in hematological malignancies, and possibly in other cancers.

Introduction

Replication stress (RS), a common source of DNA damage and genomic instability (Halazonetis et al., 2008), can be caused by deoxyribonucleotide triphosphate (dNTP) deficiency. For example, pharmacological modulators of dNTP synthesis such as hydroxyurea and 5-fluorouracil induce RS (Arlt et al., 2011; Gagou et al., 2010). RS is also triggered by overexpression of *ras* and *cyclin E* which promote cell division without sufficient dNTP pools to complete genome replication (Bester et al., 2011). How nucleotide metabolism is regulated in rapidly dividing cells to maintain balanced dNTP pools, and to prevent RS is not well understood.

Mammalian cells synthesize dNTPs either *de novo* or via the nucleoside salvage pathway (NSP) (Fig. 2.1 A) (Reichard, 1988). The *de novo* pathway utilizes glucose and amino acids to generate ribonucleotides that are required for RNA synthesis, energy storage, and signal transduction (Evans and Guy, 2004). A fraction of the cellular pool of ribonucleotides is converted into deoxyribonucleotides by ribonucleotide reductase (RNR) (Fairman et al., 2011). NSP transporters and kinases enable recycling of extracellular deoxyribonucleosides (dNs) originating from DNA degradation in apoptotic cells (Arner and Eriksson, 1995), liver biosynthetic processes (Fustin et al., 2012), and from food intake. The metabolic flux through the NSP is regulated by rate limiting kinases. Deoxycytidine kinase (dCK) phosphorylates deoxycytidine to produce deoxycytidine monophosphate (dCMP), which is a precursor of both dCTP and dTTP pools (Sabini et al., 2008). Deoxyadenosine and deoxyguanosine can also be phosphorylated by dCK, albeit with significantly lower efficacy than deoxycytidine

(Sabini et al., 2008). Thymidine kinase 1 (TK1) phosphorylates thymidine to generate dTMP, a precursor of thymidine triphosphate (dTTP) pools (Arner and Eriksson, 1995).

While *de novo* dNTP synthesis is critically important for normal DNA replication and repair (D'Angiolella et al., 2012; Niida et al., 2010; Poli et al., 2012; Pontarin et al., 2012), the role played by the NSP in maintaining the proliferating capacity and genomic integrity of dividing cells is not well understood. Recent *in vitro* studies using transformed cells and exogenous genotoxic agents have involved both dCK and TK1 in RS and DNA damage responses (DDR) (Chen et al., 2010; Matsuoka et al., 2007). However, the precise mechanisms connecting dCK and TK1 to RS and DDR pathways are yet to be characterized. It is also unknown whether dCK and TK1 function *in vivo* to prevent endogenous RS and DNA damage induction in proliferating primary cells. Preliminary analyses of *dCK*$^{-/-}$ and *TK1*$^{-/-}$ mice (Dobrovolsky et al., 2003; Toy et al., 2010) support the existence of a functional link between the NSP, RS, and hematopoietic development. Studies from our group (Toy et al., 2010) and confirmed independently by Rutschmann and colleagues (Choi et al., 2012) have documented severe developmental abnormalities affecting *dCK*$^{-/-}$ T cell, B cell, and erythroid lineages. *TK1*$^{-/-}$ mice also display hematopoietic defects characterized by slightly abnormal secondary lymphoid structures and by elevated levels of micronucleated erythrocytes (Dobrovolsky et al., 2003; Dobrovolsky et al., 2005).

In this work we sought to elucidate the biochemical and molecular mechanisms responsible for the hematopoietic phenotypes induced by dCK and TK1 inactivation. We measured dNTP pools, cell cycle kinetics, and RS levels in lymphoid and erythroid

lineages from mice lacking dCK or TK1. dNTP deficiency and RS induction were detected in both dCK and TK1 knockout models, prompting us to generate *dCK/TK1* double-knockout mice in order to analyze RS dynamics in highly proliferating NSP deficient hematopoietic precursors. Unexpectedly, concomitant inactivation of both dCK and TK1 ameliorated, rather than aggravated, the *dCK*$^{-/-}$ hematopoietic phenotype. To gain additional mechanistic insight into how TK1 inactivation rescued the *dCK*$^{-/-}$ RS phenotype we analyzed *dCK*$^{-/-}$, *TK1*$^{-/-}$, and DKO T cell precursors in the OP9-DL1 co-culture model system for T lymphocyte development (Taghon et al., 2005). Collectively, our *in vivo* and *in vitro* studies demonstrate an antagonistic functional relationship between dCK and TK1 in regulating dCTP pools *in vivo,* and reveal a previously unappreciated role for endogenous thymidine as a biologically active metabolite linked to the induction of RS in major hematopoietic lineages.

Materials and Methods

***Animals*.** Mice were bred and housed under pathogen-free (SPF) conditions and were treated in accordance with the UCLA Animal Research Committee (ARC) protocol guidelines. The *dCK*$^{-/-}$ mice were generated and bred as previously described and backcrossed to C57Bl/6 for N=7 generations (Toy et al., 2010). *TK1*$^{-/-}$ mice were re-derived from cryopreserved embryonic stem cells stored at the UC Davis Repository (Stock VG18248) and genotyped as previously described (Dobrovolsky et al., 2003). *dCK/TK1* double-knockout mice were generated by first intercrossing *dCK*$^{+/-}$ mice to *TK1*$^{+/-}$ mice to generate *dCK*$^{+/-}$ *TK1*$^{+/-}$ progeny. *dCK*$^{+/-}$ *TK1*$^{+/-}$ mice were then intercrossed together to generate *dCK/TK1* double-knockout mice at potential 1:16 frequency.

***Tissue preparation*.** Single-cell suspensions were prepared from BM by flushing femur, tibia and humerus with DMEM supplemented with 2% FBS using 25 G needles, followed by 70 μm filtration. Whole BM was depleted of mature red blood cells by overlaying cell suspensions on a solution of 16% iodixanol (Sigma-Aldrich, D1556), 0.63% NaCl, 10 mM HEPES (pH 7.4), and 0.1% NaN_3, followed by centrifugation at 900*g* for 15 minutes. The mononuclear cell-containing supernatant was transferred and washed twice prior to antibody staining or dNTP extraction. Single-cell suspensions of thymus were prepared by mechanical dissociation using frosted glass slides in DMEM supplemented with 2% FBS and 50 μg/mL DNaseI (Roche) and passed through 70 μm sterile filters. $CD4^-/CD8^-$ thymocytes were purified from whole thymocyte suspensions using combined CD4 and CD8 negative selection kits (Invitrogen).

Immunophenotyping antibodies. The following antibodies from eBioscience were used for B-cell, erythroid-cell and myeloid-cell phenotyping from whole BM: B220 (Clone RA3-6B2) PE-Cy7 and APC-eFluor780; IgM (Clone II/41) FITC, PerCP-eFluor710; CD43 (Clone eBioR2/60) PE; CD19 (Clone 1D3) APC and PE-Cy7; Ter119 (Clone TER-119) PerCP-Cy5.5 and PE-Cy7; CD71 (Clone R17217) APC and PE; and CD11b (Clone M1/70) APC-eFluor780. The following antibodies from eBioscience were used for thymocyte phenotyping: CD4 (Clone L3T4) FITC, PE, Alexa700, and PE-Cy7; CD8a (Clone 53-6.7) PE, PE-Cy7, and PerCP-eFluor710; CD25 (Clone PC61.5) APC and PE-Cy7; CD44 (Clone IM7) APC-eFluor780; CD27 (Clone LG.7F9) PE; CD45 (Clone 30-F11) PE-Cy7. Hematopoietic stem cell phenotyping from whole BM: Lineage cocktail PE, CD150 PE-Cy5 (Clone TC15-12F12.2), (Biolegend); CD127 APC-eFluor780 (Clone A7R34), Flk2/Flt3 Biotin (Clone A2F10), Sca-1 PerCP-Cy5.5 (Clone D7), c-Kit PE-Cy7 (Clone 2B8), CD34 eFluor660 (Clone RAM34), CD16/32 Alexa700 (Clone 93), (eBioscience); Streptavidin PE-Alexa610 (Invitrogen).

Flow cytometry analyses. All flow cytometry data were acquired on 4- and 5-laser LSRII cytometers (BD Biosciences) for analysis, and FACS-purification of cells was performed on 4-laser BD FACSAriaII cell sorters running BD FACSDiva6 software (BD Biosciences). All cytometry data were analyzed using FlowJo software (TreeStar, Inc.).

***DNA content staining and intracellular detection of BrdU and pH2A.X*.** BrdU (1 mg/mouse) was administered by intraperitoneal injection. Cells were collected,

antibody-stained for surface antigens, and then processed for intracellular detection of BrdU and pH2A.X using a BrdU-FITC kit staining protocol and reagents (BD Biosciences). Cells were then stained with BrdU-FITC and/or pH2A.X antibodies conjugated to FITC (Millipore, Clone JBW301) or Alexa647 (BD Biosciences, Clone N1-431). Total DNA content was assessed by staining with DAPI (Roche) at 1 µg/mL final concentration in PBS containing 2% FBS.

CTV labeling of thymocytes. Single-cell suspensions of thymocytes were resuspended in PBS containing 0.5% FBS at a cell density of $50x10^6$ cells/mL. 5 mM stocks of CTV dye (Invitrogen) dissolved in DMSO were diluted to 50 µM in PBS/0.5% FBS and then added at a dilution of 1:10 to the cell suspension (5 µM final concentration). Cells were mixed well, incubated at 37°C for 20 min, and then washed twice with 40 mL of PBS/5% FBS. Cells were then stained with fluorescent antibodies to identify DN3a thymocytes and purified via FACS.

***OP9-DL1 co-cultures*.** OP9 cells were purchased from ATCC **(**CRL-2749) and transduced by retroviral infection with Delta-like Ligand 1 vector (DL1), kindly provided by Dr. Juan Carlos Zúñiga-Pflücker, and FACS-sorted based on their GFP fluorescence. OP9-DL1 cells were maintained in Minimum Essential Medium, Alpha Modification (Sigma-Aldrich) supplemented with 20% FBS, 100 U/mL penicillin, 100 µg/mL streptomycin. Thymocyte/OP9-DL1 co-cultures were initiated by plating $50x10^3$ OP9-DL1 cells in 250 µL of media/well in 48-well tissue culture dishes at Day -1. On Day 0, DN3a thymocytes were FACS purified and resuspended in OP9-DL1 media

supplemented with 10 ng/mL Flt3-L (Peprotech) and 10 ng/mL IL-7 (Peprotech) at a cell density of 10^5 cells/mL. The single cell suspensions (250 µL) were then plated atop OP9-DL1 monolayers ($25x10^3$ cells, 5 ng/mL final concentrations of Flt3-L and IL-7 in a 500 µL total volume). Co-cultures were incubated for 2 or 4 days. Thymocytes were harvested by forceful pipetting, surface stained for developmental or intracellular markers and analyzed by flow cytometry.

***Western blots*.** Purified hematopoietic cell populations were lysed in 1X RIPA buffer containing 1X Halt Protease/Phosphatase Inhibitor (Pierce, 78440); supernatants were isolated after centrifugation at 17,000*g* for 15 min. Lysates were mixed with 1X Laemmli-SDS loading buffer, boiled, electrophoresed, and transferred to nitrocellulose membranes for immunoblotting. Monoclonal rabbit anti-Phospho-CHK1 (Ser345) (Clone 133D3); monoclonal mouse anti-CHK1 (clone 2G1D5); and monoclonal rabbit anti-Phospho-CHK2 (Thr48) (Clone C13C1) were purchased from Cell Signaling Technology. Monoclonal mouse anti-Actin (Clone MM2/193) was purchased from Sigma-Aldrich.

***Intracellular dNTP pool measurements*.** Purified hematopoietic cell populations were counted and pelleted. Pellets were then suspended in 1 mL of ice-cold 60% methanol, vortexed for 1 min and stored overnight at -20°C. The following day, the lysates were boiled for 3 min and then centrifuged for 15 min at 17,000*g* at 4°C. Supernatants were evaporated overnight in a SVC100H SpeedVac Concentrator (Savant). Dry pellets were resuspended in 100 µL ddH_2O, vortexed and centrifuged for 15 min at 17,000 *g* at 4°C

to clear insoluble debris. 5 µL of concentrated lysate was used in a 25 µL reaction volume. Reactions were carried out for 2 hrs according to previously described protocols (Mathews and Wheeler, 2009).

In vivo measurements of dCK-dependent incorporation of [^{13}C/^{15}N]-deoxycytidine into dCTP and dTTP pools. Mice were injected intraperintoneally with 200 µL of 2.5 mM uniformly-labeled [^{13}C/^{15}N]-deoxycytidine (Cambridge Isotopes). Mice were euthanized 30 min post injection to harvest BM cells and DN thymocytes. Cells were washed with ice cold PBS/2% FBS and then extracted with 60% methanol overnight at -20°C, evaporated, and the dry pellets were resuspended in 100 to 500 µL of 5 mM hexylamine. dTTP/dCTP concentrations were then determined by liquid chromatography-tandem mass spectrometry (LC-MS/MS) using an Agilent 6460 Triple Quad LC/MS system. The stationary phase was a Phenomenex Gemini-NX C18 column (2.0 x 100 mM) with 5 mM hexylamine in ddH_2O and acetonitrile as the mobile phases.

Whole tissue nucleoside concentration measurements. Solid tissues were homogenized at 4°C in acetonitrile:methanol (9:1) using the BulletBlender Tissue Homogenizer (NextAdvance) according to the manufacturer's specifications. BM cells were flushed using ice-cold PBS, filtered into single-cell suspensions, pelleted and resuspended in homogenization buffer. Whole blood was collected in heparinized tubes and then centrifuged to separate plasma and blood cells. Both fractions were extracted directly with the homogenization buffer. Extracted samples were evaporated and the dry pellets were resuspended in ddH_2O. Thymidine concentrations were then determined by

LC-MS/MS. The stationary phase was a Thermo Fisher Hypercarb column (2.1 x 100 mM) with 0.1% formic acid in ddH_2O and 0.1% formic acid in acetonitrile as the mobile phases.

Statistical analyses

All statistics presented as average of biological replicates with standard error of the mean (+SEM). P value significances were calculated using one sample t-test function in GraphPad Prism 5 (GraphPad Software).

Results

dCTP pool depletion, RS induction, early S-phase arrest, and DNA damage in *dCK*$^{-/-}$ lymphoid and erythroid hematopoietic lineages. To investigate the possibility that nucleotide deficiency causes the hematopoietic abnormalities identified in the *dCK*$^{-/-}$ mice (Toy et al., 2010), we quantified dNTP pools in CD4/CD8 double-negative (DN) thymocytes, bone marrow (BM)-resident B-cell progenitors, and in nucleated erythroid progenitors. dCTP pools were significantly reduced in all three *dCK*$^{-/-}$ hematopoietic lineages (Fig. 2.1 B; *, P<0.003; **, P<0.02); dTTP, dGTP and dATP pools were largely unaffected (Fig. 2.1 B; Table 1). Next, we asked whether dCTP deprivation triggers RS in *dCK*$^{-/-}$ hematopoietic lineages by probing for the presence of the activated form of the key ATR effector and replication stress response (RSR) regulator CHK1 kinase (Branzei and Foiani, 2008). Compared to WT cells, *dCK*$^{-/-}$ lineages displayed significantly higher levels of CHK1 phosphorylated on Ser345 (pChk1), indicating exposure to endogenous RS *in vivo* (Fig. 2.1 C).

To examine the functional consequences of dCTP deficiency and RS, we analyzed the cell cycle profiles of highly proliferative sub-populations that we found to be selectively depleted (e.g. T and B-cell precursors) or overrepresented (erythroblast precursors) amongst *dCK*$^{-/-}$ hematopoietic progenitor populations. These highly proliferative subpopulations included DN3b T-cell precursors (CD4^{-}, CD8^{-}, CD44^{-}, CD25$^{med\text{-}lo}$, CD27^{hi} thymocytes) (Taghon et al., 2006), Hardy Fraction B-C B-cell progenitors (IgM^{-}, B220^{+}, CD43^{hi}, CD19^{hi}) (Hardy et al., 2007), and nucleated erythroblast cells (EryA; Ter119^{+}, CD71^{+}, FSC^{hi}) (Liu et al., 2006). *dCK*$^{-/-}$ cells from all

three progenitor populations showed abnormal cell cycle profiles (Fig. 2.1 D), with *dCK*$^{-/-}$ EryA cells displaying the most pronounced increase in the percentage of cells in S-phase. Each of the three subpopulations appeared to be arrested in early S-phase (Fig. 2.1 D).

To unequivocally demonstrate that dCK inactivation triggers early S-phase arrest, we performed kinetic measurements of DNA synthesis *in vivo* by measuring bromodeoxyuridine (BrdU) incorporation into WT and *dCK*$^{-/-}$ DN3b, Hardy B-C, and EryA cells 1 hr after intraperitoneal injection of the probe. We found that the amount of BrdU incorporated per BrdU^{+} cell was reduced significantly in all three *dCK*$^{-/-}$ subpopulations (Fig. 2.1, E and F), a result consistent with impaired DNA synthesis. To confirm this interpretation, we used a BrdU chase approach to analyze productive DNA synthesis *in vivo* (Begg et al., 1985; Terry and White, 2006). Mice were pulsed with BrdU and the free circulating probe was allowed to be eliminated (i.e. chased) for 3 and 5 hrs before analyzing BrdU incorporation. This approach enabled detection and quantification of BrdU chase gaps, which are indicators of productive DNA synthesis (Terry and White, 2006). While BrdU^{+} WT cells synthesized sufficient new DNA during the 3 and 5 hr chase points to generate typical BrdU chase gaps, BrdU^{+} *dCK*$^{-/-}$ cells did not display chase gaps, thus indicating arrested DNA synthesis (Fig. 2.1 G). Consequently, BrdU^{+} *dCK*$^{-/-}$ cells remained stationary in early S-phase (Fig. 2.1 G). Moreover, few *dCK*$^{-/-}$ cells entered the S-phase during the 3 and 5 hr chase periods (Fig. 2.1 G, BrdU^{-} S-phase gates), further confirming that dCK inactivation perturbed cell cycle kinetics. The degree of S-phase arrest triggered by dCK inactivation correlated

with strong upregulation of the RSR/DDR marker histone H2A.X phosphorylated on Ser139 (pH2A.X) in early S-phase cells from all three hematopoietic subpopulations (Fig. 2.1, H and I; *,P<0.0001). While the effects of dCK inactivation were highly penetrant in lymphoid and erythroid progenitor populations that have short S-phases (<7 hrs), myeloid lineage cells which have a longer S-phase (>9 hrs) were significantly less affected (Fig. 2.1, I and J).

Effects of TK1 inactivation on dTTP pools, hematopoietic development, and endogenous RS. Next, we determined whether inactivation of TK1, the other cytosolic NSP kinase expressed in mammalian cells (Fig. 2.1 A), also affected hematopoietic development in a manner similar to dCK inactivation. Unlike the severe defects in hematopoiesis induced by dCK inactivation, lympho- and erythropoiesis appeared significantly less affected in the *TK1*$^{-/-}$ mice. Nonetheless, dTTP levels were significantly decreased in *TK1*$^{-/-}$ B cell and erythroid lineages compared to corresponding WT populations (Fig. 2.2 A; *, P<0.005; **, P=0.0001); dCTP pools were largely unaffected (Fig. 2.2 A).

In contrast to dTTP pool depletions in *TK1*$^{-/-}$ B cell and erythroid lineages, *TK1*$^{-/-}$ DN thymocytes had normal dTTP pools, suggesting the existence of a compensatory mechanism. dCMP produced by dCK can contribute to the dTTP pool through the sequential actions of deoxycytidine monophosphate deaminase (DCTD) and thymidylate synthase (TYMS) (Fig. 2.1 A) (Staub et al., 1988). To determine whether such dCK-dependent contributions occur *in vivo* to potentially help maintain dTTP pools

in the absence of TK1, we measured the relative efficiencies of deoxycytidine to thymidine conversion in WT and *TK1*$^{-/-}$ mice by utilizing [^{13}C/^{15}N]-labeled deoxycytidine ([^{13}C/^{15}N]-dC). Both genotypes were pulsed with [^{13}C/^{15}N]-dC for 30 min and the conversion of [^{13}C/^{15}N]-dC to [^{13}C/^{15}N]-dCTP and to [^{13}C/^{15}N]-dTTP was determined in target hematopoietic populations using liquid chromatography-tandem mass spectrometry (LC-MS/MS) (Fig. 2.2 B). We found that the [^{13}C/^{15}N]-dTTP to [^{13}C/^{15}N]-dCTP ratio was over two-fold higher in *TK1*$^{-/-}$ DN thymocytes than in the corresponding WT subpopulation (7.3:1 *vs*. 3.5:1) (Fig. 2.2 C). Therefore, DN thymocytes may compensate for the loss of the TK1-dependent input in the dTTP pools by converting a larger fraction of dCMP to dTTP (Fig. 2.2 A). In contrast to DN thymocytes, *TK1*$^{-/-}$ BM cells displayed a lower [^{13}C/^{15}N]-dTTP to [^{13}C/^{15}N]-dCTP ratio than WT BM cells (1.3:1 *vs.* 2.1:1) (Fig. 2.2 C). We also observed an approximately four-fold decrease in the amount of [^{13}C/^{15}N]-dTTP in *TK1*$^{-/-}$ BM cells relative to WT controls (Fig. 2.2 C). Collectively, these findings suggest that, compared to *TK1*$^{-/-}$ DN thymocytes, *TK1*$^{-/-}$ BM cells are less able to rely upon dCK to maintain dTTP pools.

The dTTP pool depletion observed in *TK1*$^{-/-}$ BM cells suggested that, similar to their *dCK*$^{-/-}$ counterparts, these cells would also be subjected to RS induction. BM-resident *TK1*$^{-/-}$ hematopoietic populations indeed displayed elevated pChk1 levels while *TK1*$^{-/-}$ DN thymocytes were not affected (Fig. 2.2 D), consistent with the dTTP pool depletion found in BM *TK1*$^{-/-}$ and with the normal dTTP pools in *TK1*$^{-/-}$ thymocytes, respectively (Fig. 2.2 A). Regardless of their dTTP pool status, proliferating *TK1*$^{-/-}$ hematopoietic progenitors did not display detectable changes in the cell cycle profiles

(Fig. 2.2 E). Moreover, in contrast to the highly elevated levels of pH2A.X found in *dCK*$^{-/-}$ DN3b thymocytes and Hardy B-C B-cell progenitors (Fig. 2.1, H and I), corresponding *TK1*$^{-/-}$ lymphoid cells did not upregulate pH2A.X (Fig. 2.2 F). Only *TK1*$^{-/-}$ EryA cells significantly upregulated the expression of this DDR marker (Fig. 2.2 F; *, $P<0.03$), albeit at levels that were 8-fold lower than those observed in *dCK*$^{-/-}$ EryA cells (Fig. 2.1 I).

Blocking thymidine salvage alleviates the RS triggered by dCK inactivation in bone marrow-resident hematopoietic progenitors. To further investigate the mechanistic basis of dNTP pool imbalances and RS phenotypes observed in the *dCK*$^{-/-}$ and *TK1*$^{-/-}$ mice we examined the consequences of concomitant inactivation of these two NSP kinases. *dCK/TK1* double-knockout (DKO) hematopoietic cells should completely lack the ability to salvage dNs from their extracellular environment and must rely exclusively on the *de novo* pathway to produce dNTPs for DNA replication and repair. DKO mice were born at sub-Mendelian frequencies (hazard ratio 1.85) and weighed 30% less than WT, *TK1*$^{-/-}$, and *dCK*$^{-/-}$ littermates at 5 weeks of age (N=7/genotype, $P<0.001$), indicating that the NSP was important to support animal growth. However, combined inactivation of dCK and TK1 did not further aggravate the defects observed in the *dCK* single knockout mice, but rather significantly rescued their hematopoietic development. Thus, relative to *dCK*$^{-/-}$ cells, DKO B-cell progenitors showed greatly improved differentiation past the Hardy B-C stage (Fig. 2.3, A-C). Moreover, the cell cycle profile and pH2A.X expression of DKO Hardy B-C cells appeared normal (Fig. 2.3 A). In the erythroid lineage, dual inactivation of dCK and TK1,

partially reduced the relative abundance of EryA cells in the bone marrow, but DKO EryA cells still displayed an abnormal cell cycle profile with upregulated pH2A.X expression relative to WT and *TK1*$^{-/-}$ cells (Fig. 2.3 D). Nonetheless, these cells were in fact relieved of the early S-phase arrest phenotype characteristic of their *dCK*$^{-/-}$ counterparts (Fig. 2.3 D). Intriguingly, pH2A.X upregulation in DKO EryA cells occurred in mid/late S-phase rather than at the G_1/S border corresponding to early stages of DNA synthesis, as seen following dCK inactivation (Fig. 2.3 D). Altogether, erythropoiesis itself in DKO mice appeared significantly normalized, as further evidenced by the alleviation of the abnormal extramedullary erythropoiesis manifested as splenomegaly in the *dCK*$^{-/-}$ mice (Fig. 2.3E).

Underlying the rescue of early S-phase arrest in DKO B cell and erythroid precursors was a surprising finding concerning the restoration of dCTP pools in *dCK*$^{-/-}$ BM hematopoietic cells following TK1 inactivation. Thus, DKO BM cells had normal dCTP pools, which corresponded to a more than two-fold increase over dCTP pools from *dCK*$^{-/-}$ BM cells (Fig. 2.3 F; *, P<0.001). In contrast to dCTP pools, dTTP pools from DKO BM cells were not restored to WT levels and remained at levels comparable to those of *TK1*$^{-/-}$ BM cells (Fig. 2.3 F).

TK1 inactivation rescues the development of *dCK*$^{-/-}$ T cells. Similar to its effects on the development of *dCK*$^{-/-}$ B cells, TK1 inactivation also rescued *dCK*$^{-/-}$ T cell development. DKO thymi were significantly larger than those from the *dCK*$^{-/-}$ mice due to increased overall cellularity (Fig. 2.4, A and B; *, P<0.001). In DKO mice, the 8-fold

increase in thymic cellularity over *dCK*$^{-/-}$ thymi was accompanied by a striking normalization of a key event in thymic T cell development, specifically the transition from the DN to the CD4/CD8 double-positive (DP) stage (Fig. 2.4 C). Thus, in contrast to the *dCK*$^{-/-}$ thymocytes, which experience a severe block at the DN to DP transition, DKO thymocytes displayed a DN to DP ratio that was nearly indistinguishable from that of their WT and *TK1*$^{-/-}$ counterparts (Fig. 2.4 C). This phenotypic rescue was accompanied by reduced levels of the RSR activation markers pChk1 and CHK2 kinase phosphorylated on Thr68 (pChk2) in DKO DN thymocytes compared to the corresponding *dCK*$^{-/-}$ population (Fig. 2.4 D). Furthermore, both the early S-phase arrest and pH2.AX induction were significantly reduced in DKO cells relative to *dCK*$^{-/-}$ DN3b thymocytes (Fig. 2.4 E). Collectively, these findings indicated that elimination of TK1 activity drastically lowered the levels of RS in DKO versus *dCK*$^{-/-}$ thymocytes, an effect reflected by a dramatic improvement of *dCK*$^{-/-}$ T cell development (Fig. 2.4 A).

Endogenous thymidine plays a critical role in the induction of a RS phenotype in *dCK*$^{-/-}$ thymocytes. Excessive levels of intracellular dTTP have been shown in *in vitro* studies to negatively regulate dCTP pools through allosteric inhibition of RNR-mediated synthesis of deoxycytidine diphosphate (dCDP), the direct precursor of dCTP (Reichard, 1988). It is conceivable that the RS experienced by *dCK*$^{-/-}$ hematopoietic cells *in vivo* can be attributed to concomitant inhibition of both salvage and *de novo* pathways for dCTP production, therefore creating conditions of synthetic sickness/lethality (SSL). As shown in Fig. 2.5 A, hematopoietic progenitors in bone marrow and thymus are exposed to endogenous concentrations of thymidine that are significantly higher than in other

tissues and in plasma. Such high levels of endogenous thymidine may increase dTTP pools via TK1-mediated salvage. Decreased dTTP production caused by TK1 inactivation would relieve the inhibition of RNR's ability to reduce CDP to dCDP in proliferating *dCK*$^{-/-}$ cells residing in bone marrow and thymus. The corresponding increase in the output of the *de novo* pathway would therefore help restore dCTP pools depleted by dCK inactivation. To test the validity of this model we reasoned that if excessive thymidine salvage in thymus and bone marrow was indeed responsible for the *dCK*$^{-/-}$ phenotype, then removal of *dCK*$^{-/-}$ hematopoietic cells from a thymidine-rich *in vivo* environment should relieve their RS phenotype. To test this prediction we modeled T cell development *in vitro* using the OP9-DL1 co-culture system (Taghon et al., 2005). Importantly, LC-MS/MS measurements showed that the OP9-DL1 culture media used in these experiments contained submicromolar amounts of thymidine that are comparable to plasma levels (Fig. 2.5 B), and are much lower than those measured in thymus and bone marrow (Fig. 2.5 A). DN3a thymocytes (CD4^{-}, CD8^{-}, CD44^{-}, CD25^{hi}, CD27^{lo}) from WT, *dCK*$^{-/-}$, *TK1*$^{-/-}$, and DKO mice were subsequently labeled with a fluorescent proliferation dye (CellTrace Violet, CTV), cultured on the OP9-DL1 stroma, and then assessed for cell division four days later by flow cytometric analysis of CTV dye dilution (Fig. 2.5 C). We found that, in contrast to their *in vivo* phenotype, *dCK*$^{-/-}$ DN3a thymocytes proliferated robustly in the *in vitro* co-culture system that contained submicromolar levels of thymidine. Thus, *dCK*$^{-/-}$ cells divided up to 8 times, which was equivalent to the rate of cell division observed for WT, *TK1*$^{-/-}$, and DKO thymocytes over the course of the *in vitro* study (Fig. 2.5 D). These findings indicated that salvage of

endogenous thymidine *in vivo* contributes to the induction of S-phase arrest and RS in *dCK*$^{-/-}$ hematopoietic progenitors.

To confirm this hypothesis, we titrated thymidine into the DN3a/OP9-DL1 co-cultures and determined how this affected the rate of cell proliferation. We found that the addition of 20 μM thymidine to the co-culture media significantly blocked the proliferation of *dCK*$^{-/-}$ cells without affecting WT cells (Fig. 2.5 E, top row). Further increasing the thymidine concentration from 20 to 100 μM completely and specifically blocked the proliferation of *dCK*$^{-/-}$ cells (Fig. 2.5 E, bottom row). As expected, *TK1*$^{-/-}$ and DKO cells were unaffected by thymidine at either concentration (Fig. 2.5 E), because of their inability to salvage this deoxyribonucleoside.

To verify that the thymidine-induced proliferation block was caused by RS induction, we assayed for pH2A.X activation in DN3b/OP9-DL1 co-cultures in response to thymidine concentrations varying from 10 to 200 μM. *dCK*$^{-/-}$ thymocytes strongly induced pH2A.X following exposure to thymidine concentrations as low as 10 μM. pH2A.X expression by *dCK*$^{-/-}$ cells peaked at 20 μM thymidine (Fig. 2.5 F) and higher concentrations of thymidine triggered massive cell death in the *dCK*$^{-/-}$ DN3b/OP9-DL1 co-cultures (percent sub-G_1 cells>80% at 50 μM or greater thymidine concentrations, N=3 independent experiments). WT cells were 10-fold more resistant to thymidine than *dCK*$^{-/-}$ cells while *TK1*$^{-/-}$ and DKO cells were completely resistant to thymidine at all tested concentrations (Fig. 2.5 F).

Lastly, to determine whether *dCK*$^{-/-}$ cells were intrinsically more susceptible to RS induced by nucleotide deprivation via a TK1-independent mechanism, we titrated the RNR inhibitor hydroxyurea into the DN3b/OP9-DL1 co-cultures and then measured RS induction 12 hrs later. WT, *dCK*$^{-/-}$, *TK1*$^{-/-}$, and DKO cells were equally susceptible to hydroxyurea concentrations ranging from 10-200 μM (Fig. 2.5 G), suggesting that dCK plays a specific role in preventing RS induced by thymidine. In conclusion, data from the OP9-DL1 co-culture *in vitro* T cell-development system showed that dCK deficient cells were hypersensitive to RS induced by low amounts of thymidine through a TK1-dependent mechanism.

Discussion

A functional interplay between dCK and TK1 regulates dNTP pools and prevents RS during hematopoietic development. Using genetic models of individual and combined deficiencies in the cytosolic dN kinases dCK and TK1, we demonstrate that the dN salvage pathway contributes to both induction and prevention of RS during hematopoietic development. We also show that endogenous thymidine itself is a highly active metabolite that induces RS *in vivo*, an observation reminiscent of a widely used *in vitro* experimental approach for synchronizing cells in cell cycle known as the “thymidine block” (Xeros, 1962). In the course of a typical thymidine block experiment, cultured cells exposed to high concentrations of thymidine undergo S-phase arrest through a TK1-dependent mechanism (Gagou et al., 2010). It is through the kinase action of TK1 that exogenously added thymidine is trapped in cells, thus enabling its conversion to dTTP in the cytosol. dTTP is not only a precursor of DNA but also a strong allosteric

inhibitor of RNR's affinity for its pyrimidine ribonucleotide substrates CDP and uridine diphosphate (UDP) (Fairman et al., 2011). dTTP-mediated inhibition of CDP conversion to dCDP depletes dCTP pools, thus causing S-phase arrest (Bjursell and Reichard, 1973; Larsson et al., 2004). The thymidine block approach has been thought of traditionally as an *in vitro* "laboratory tool" (Gentry, 1992) with little if any relevance to *in vivo* conditions. Our data challenge this assumption by establishing thymidine block as a metabolic phenomenon that normally occurs in bone marrow and thymus during hematopoiesis. We show that, in the absence of dCK activity, physiological concentrations of thymidine in these tissues are sufficient to induce dCTP deprivation and severe RS in proliferating T cell, B cell, and erythroid precursors. By enabling these cells to salvage deoxycytidine, dCK replenishes dCTP pools depleted by dTTP produced from thymidine via TK1, thereby exerting an important role in hematopoiesis. The two cytosolic dN salvage kinases thus play paradoxically opposing roles; TK1 in the absence of dCK induces RS, while dCK functions to prevent RS in TK1-expressing cells exposed to elevated levels of endogenous thymidine (Fig. 2.6, A and B). Importantly, the degree of dependence on the NSP kinases to avoid endogenous RS varied across different hematopoietic lineages, with the erythroid lineage being most affected, followed by T and B cell progenitors and then by myeloid precursors (Fig. 2.1 J and Fig. 2.6 B).

The causal relationship between TK1 activity, inhibition of *de novo* dCTP production and dependency on dCK to avoid thymidine-induced endogenous RS inevitably leads to the question of why rapidly dividing hematopoietic cells engage in

what at first sight would appear as excessive salvage of thymidine. Further adding to the puzzle of why hematopoietic cells express high levels of TK1 is the fact that our data show that hematopoiesis appears to be much less severely affected by TK1 inactivation than by the loss of dCK1 activity. While additional studies are needed to fully elucidate the biological significance of TK1 by further analyses of the consequences of its inactivation on hematopoiesis, our preliminary data indicate that TK1 may play an important role in regulating the dUTP/dTTP balance. Thus, *TK1*$^{-/-}$ BM cells displayed an approximate 4-fold increase in dUTP/dTTP ratio relative to WT BM cells (WT, 3.11% ± 1.04 SD; *TK1*$^{-/-}$, 0.76% ± 0.06 SD; N=2/genotype). A proper dUTP/dTTP ratio is needed to reduce misincorporation of dUTP into DNA (Melnyk et al., 1999), thereby preventing the formation of U:A pairs. Excessive occurrences of such pairs may have cytotoxic effects (Hagen et al., 2006) and would require the intervention of uracil-DNA glycosylases and of base excision repair (BER) mechanisms to prevent induction of RS. TK1 activity could promote the maintenance of a low dUTP/dTTP ratio in three ways. *First*, through preferential phosphorylation of thymidine *vs.* deoxyuridine due to a 20-fold difference in affinity in favor of thymidine (Munch-Petersen et al., 1991), TK1 is likely to generate significantly more dTMP than dUMP. In turn, this would increase the substrate availability for thymidylate kinase (TMPK), an enzyme recently shown to play an important role in preventing dUTP incorporation into the DNA during DNA repair (Hu et al., 2012). *Second*, by opposing the activity of cytosolic nucleotidases, which dephosphorylate dTMP, TK1 activity will prevent the loss of thymidine containing deoxyribonucleotides from dividing cells (He and Skog, 2002). *Third*, by increasing cytosolic dTTP pools, TK1 would promote the allosteric inhibition of RNR's ability to

reduce not only CDP but also UDP (Fairman et al., 2011) (Fig. 2.6 B) therefore preventing excessive accumulation of dUTP due to high RNR activity in proliferating cells. If confirmed by future studies, this hypothesis may explain why the dTTP-mediated allosteric regulation of RNR's substrate specificity is mostly conserved amongst members of the 3 classes of ribonucleotide reductases despite wide differences in their primary and quaternary structures (CITE Reichard, P. (1993) Science 260, 1773–1777 and Reichard Ann ... Rev. Biochem. 1995.64:1-28).

The role of the deoxyribonucleoside salvage pathway in non-hematopoietic tissues. Our findings indicate that the *de novo* synthesis pathway can maintain dNTP pools at levels that are sufficient to support most hematopoietic proliferation. However, the fact that DKO mice are born at sub-Mendelian frequencies and surviving animals display growth retardation indicates that the NSP is important to support overall growth. It is possible that the growth defects affecting the DKO mice may result from increased stress forced upon other biosynthetic pathways in the absence of the NSP. The utilization of dN salvage for dNTP synthesis requires significantly less ATP and NADPH than does *de novo* synthesis (Lunt and Vander Heiden, 2011). For example, *de novo* synthesis of 1 mole of dCTP or dTTP starting from glucose, glutamine, aspartate, and bicarbonate requires 6 moles of ATP each, while the same amount can be generated via salvage at a cost of 3 moles of ATP (Voet, 2004). ATP and NADPH savings afforded by utilizing pyrimidine salvage instead of *de novo* synthesis could then be spent by cells to generate other essential biomass, such as proteins and phospholipids. An alternative explanation for the growth defects in the DKO mice involves mitochondrial dysfunction

due to imbalances in the dNTP pools in this organelle. Defects in mitochondrially compartmentalized dNTP synthesis have been shown to cause severe developmental abnormalities (Eriksson and Wang, 2008; Gonzalez-Vioque et al., 2011; Zhou et al., 2010; Zhou et al., 2008). Since in cycling cells mitochondrial dNTP pools correlate linearly with the cytoplasmic pools (Gandhi and Samuels, 2011), imbalances in cytosolic dNTP pools resulting from defects in the NSP may impair mitochondrial DNA synthesis and thus trigger mitochondrial stress manifested by embryonic lethality and neonatal growth retardation.

Nucleotide deficiency, cellular transformation and the relationship between the NSP and the RSR pathway. Nucleotide deficiency has been recently shown to promote cellular transformation (Bester et al., 2011). The study by Bester and colleagues described how overexpression of viral E-proteins or of mammalian Cyclin E in cultured human keratinocytes overrides normal cell cycle regulation and triggers premature S-phase entry, which in turn caused RSR pathway activation and subsequent mutation induction. Presumably, this chain of events is initiated by the inability of E-protein/Cyclin E overexpressing keratinocytes to generate sufficient dNTP pools to support DNA replication and repair. The nucleotide deficiency observed here in our *in vivo* genetic systems resembles that induced by Bester et al. in their cell culture system. However, despite the severe nucleotide deficiency and strong activation of the RSR pathway observed in the *dCK*$^{-/-}$ hematopoietic lineages, we did not detect increased rates of cancer in the *dCK*$^{-/-}$ mice when these animals were followed for 12 months after birth. It is possible that the onset of nucleotide deficiency-induced cancer in our model occurs at

an even older age. It is also conceivable that the protective effects of the RSR pathway in *dCK*$^{-/-}$ mice are sufficient to eliminate potentially oncogenic cells, whereas a yet to be defined aspect of the keratinocyte system permits the propagation of cells carrying fixed DNA mutations. Future studies are therefore required to determine the consequences of concomitant inactivation of the NSP and of key components of the RSR pathway. In this context, it is important to note the similarities between the defects in erythropoiesis observed in the NSP deficient mice and defects in this hematopoietic lineage documented in mouse models of ATR-Seckel (Murga et al., 2009) and of *Chk1* haploinsufficiency (Boles et al., 2010).

Therapeutic implications. The demonstration of a functional link between endogenous thymidine, dN kinases, nucleotide deficiency and RS induction highlights a potential therapeutic strategy to induce RS overload, and ultimately cell death, in hyperproliferative diseases such as cancer. Thymidine therapy has been attempted in human malignancies based on the ability of this nucleoside to induce S-phase arrest of cultured cancer cells by inhibiting their *de novo* dCTP synthesis. Although well tolerated in patients, thymidine had limited efficacy when used as single agent therapy in acute lymphoid and myeloid leukemias (Kufe et al., 1980). By demonstrating that dCK, which is frequently overexpressed in hematological malignancies, significantly contributes to dCTP pools *in vivo*, the current study may have revealed an important mechanism of resistance to thymidine and thus explain the failure of thymidine in initial clinical trials. Combining thymidine with a small molecule dCK inhibitor (dCKi) would induce synthetic sickness/lethality (SSL) by blocking both dCTP-producing pathways. Whether an

adequate therapeutic window exists for thymidine/dCKi SSL will be determined in subsequent studies.

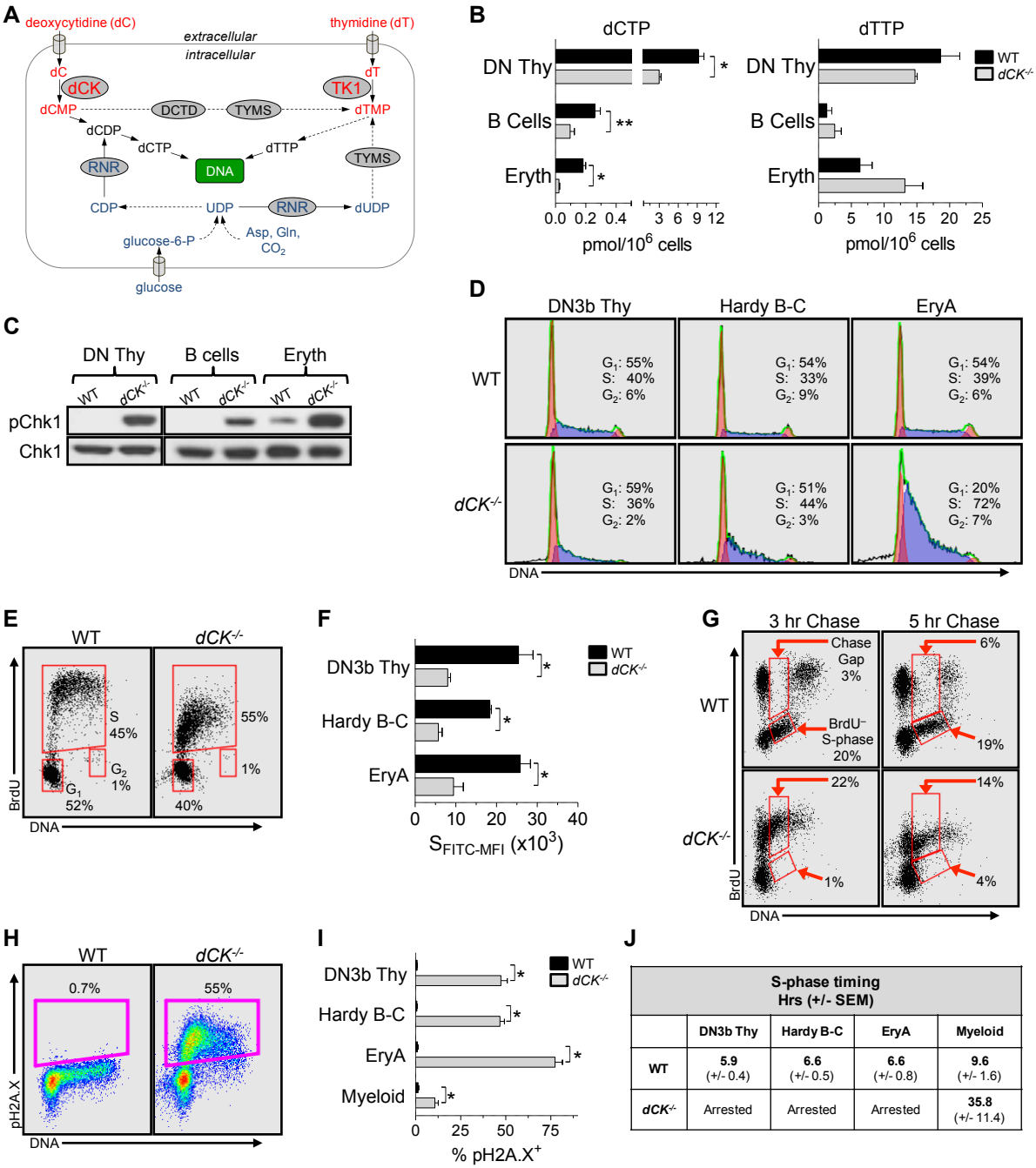

Figure 2.1. dCK inactivation causes severe replication stress (RS) in lymphoid and erythroid lineages. (**A**) Schematic of the *de novo* pathway (blue) and of the nucleoside salvage pathway (NSP, red) inputs into pyrimidine dNTP pools for DNA synthesis. Solid arrows indicate single step processes; dashed arrows indicate multi-step processes with intermediates not named/depicted in the schematic. Gln: glutamine, Asp: aspartate, UDP: uridine diphosphate, CDP: cytidine disphosphate, RNR:

ribonucleotide reductase, TYMS: thymidylate synthase, DCTD: dCMP deaminase. (**B**) dCTP and dTTP pools in WT (black bars) and *dCK*$^{-/-}$ (gray bars) cells; DN Thy: CD4/CD8 double-negative thymocytes; B cells: bone marrow (BM)-resident B-cell progenitors, and Eryth: BM-resident erythroid progenitors. Data are average value + SEM for 3 independent measurements generated from 4 pooled mice per genotype during each independent measurement. *, P<0.003; **, P<0.02. (**C**) Western blot detection of pChk1 (phosphorylated on Ser345) in lysates from lymphoid and erythroid progenitors. Total CHK1 protein was used as a loading control. (**D**) Representative examples of total DNA content staining and percentage of cells in G_1, S and G_2/M phases in WT and *dCK*$^{-/-}$ DN3b thymocytes, Hardy Fraction B-C cells, and EryA cells. (**E**) Representative bromodeoxyuridine (BrdU) incorporation into WT and *dCK*$^{-/-}$ DN3b thymocytes 1 hr after injection of BrdU. Percent of cells in G_1, S, and G_2 phases of the cell cycle are indicated. (**F**) Average of anti-BrdU FITC mean fluorescent intensities of S-phase ($S_{FITC\text{-}MFI}$) WT and *dCK*$^{-/-}$ DN3b thymocytes, Hardy Fraction B-C cells, and EryA cells. Data are average value + SEM, N=4 mice/genotype. *, P<0.01. (**G**) Representative BrdU detection in WT and *dCK*$^{-/-}$ DN3b thymocytes after 3 and 5 hrs of BrdU chase (N=4 mice/genotype). Percentages of cells present in chase gap and BrdU^{-} S-phase gates are indicated. (**H**) Detection of H2A.X phosphorylated on Ser139 (pH2A.X) in DN3b thymocytes by flow cytometry. Percentages of pH2A.X-positive cells are indicated. (**I**) Quantification of pH2A.X-positive staining in DN3b thymocytes, Hardy B-C cells, and EryA cells from WT (black bars) and *dCK*$^{-/-}$ (gray bars) mice. N=7 mice/genotype; *, P<0.0001. (**J**) S-phase durations in hrs calculated using 5 hr BrdU chase conditions in DN3b thymocytes, Hardy B-C cells, EryA cells, and BM-resident myeloid cells (CD11b^{+}) from WT and *dCK*$^{-/-}$ mice. Data are average value in Hrs + SEM, N=4 mice/genotype.

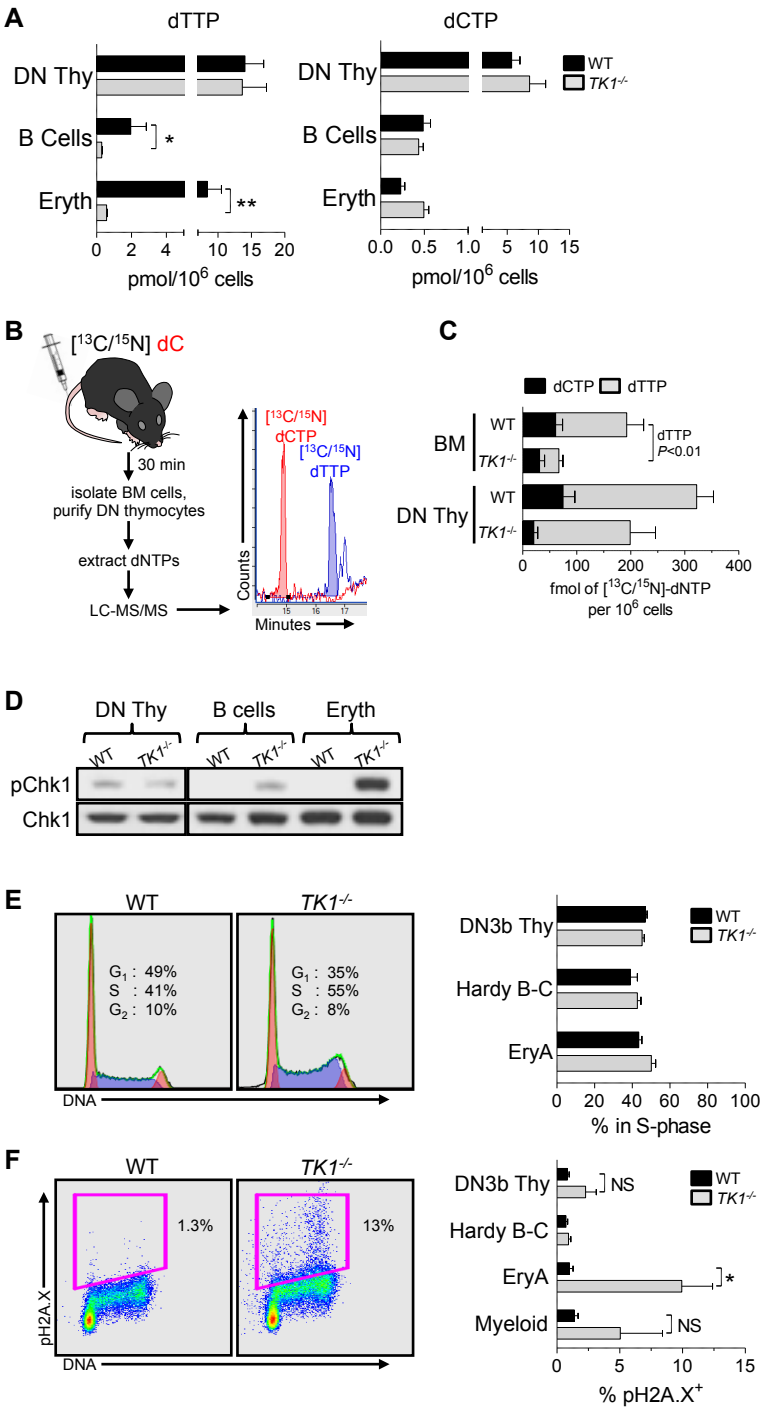

Figure 2.2. Inactivation of thymidine kinase (TK1) causes minor RS in hematopoietic cells. (**A**) dTTP and dCTP pools from WT (black bars) and *TK1*$^{-/-}$ (gray bars) DN Thymocytes, BM-resident B-cell progenitors, and BM-resident erythroid progenitors. Data are average value + SEM for 3 independent measurements, N=4 mice/genotype/replicate. *, *P*<0.005; **, *P*=0.0001. (**B**) Schematic of *in vivo*

measurements of dCK-dependent incorporation of [^{13}C/^{15}N]-deoxycytidine ([^{13}C/^{15}N]-dC) into free cellular dCTP and dTTP pools. [^{13}C/^{15}N]-dC was injected intraperintoneally and 30 minutes later mice were sacrificed to isolate nucleated BM cells and DN thymocytes for dNTP extraction. Concentrations of [^{13}C/^{15}N]-labeled nucleotides were determined using LC-MS/MS. (**C**) Concentrations (fmol per 10^6 cells) of [^{13}C/^{15}N]-dCTP (black bars) and [^{13}C/^{15}N]-dTTP pools (gray bars) from WT and *TK1*$^{-/-}$ nucleated BM cells and DN thymocytes. Data are average + SEM from N=5 (WT) and N=4 (*TK1*$^{-/-}$) mice from 2 independent experiments. (**D**) Western blot detection of pChk1 in lysates from lymphoid and erythroid progenitors. Total CHK1 protein was used as a loading control. (**E**) Representative example of total DNA content staining in EryA cells from WT and *TK1*$^{-/-}$ cells, and quantification of percentage of DN3b thymocytes, Hardy B-C cell, EryA cells in S-phase as determined by total DNA content staining. Data are average value + SEM, N=3 mice/genotype. (**F**) Representative example of pH2A.X detection in WT and *TK1*$^{-/-}$ EryA cells. (**G**) Quantification of pH2A.X-positive staining in DN3b thymocytes, Hardy B-C cell, EryA cells from WT (black bars) and *TK1*$^{-/-}$ (gray bars) mice. N=4 mice/genotype. NS, $P>0.05$; *, $P<0.03$.

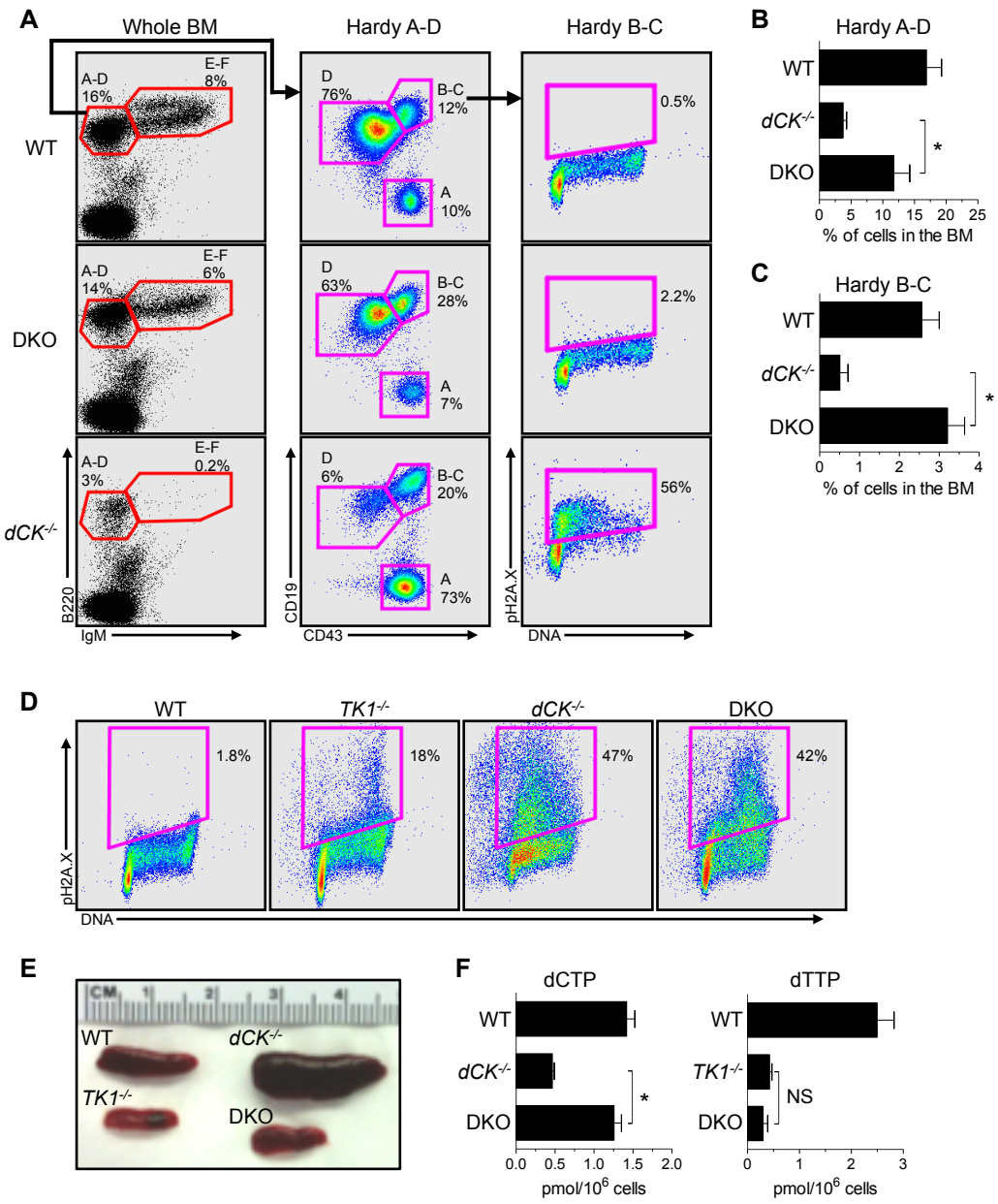

Figure 2.3. TK1 inactivation relieves the early S-phase RS in *dCK*$^{-/-}$ developing B and erythroid cells. (**A**) Representative examples of B-cell development staining of BM samples from WT, *dCK*$^{-/-}$, and *dCK/TK1* double-knockout (DKO) mice. IgM and B220 staining of whole BM cells identify Hardy Fraction A-D (B220^{+} IgM^{-}) and Hardy Fraction E-F (B220^{+} IgM^{+}) populations. Hardy Fraction A-D cells are sub-gated using CD43 and CD19 expression to identify Hardy Fraction A (CD43^{hi}, CD19^{-}), B-C (CD43^{hi}, CD19^{+}), and D (CD43^{lo}, CD19^{+}). Hardy Fraction B-C cells are then analyzed for cell cycle position and pH2A.X expression. Plots are representative of N=3 mice/genotype. (**B-C**)

Quantification of percentage of total BM cells that are phenotypically Hardy Fraction A-D (**B**), and Hardy Fraction B-C (**C**) populations from WT, *dCK*$^{-/-}$, and DKO mice. Data are average value + SEM for N=3/genotype; *, *P*<0.04; **, *P*<0.01. (**D**) Representative examples of pH2A.X detection in EryA cells from WT, *dCK*$^{-/-}$, *TK1*$^{-/-}$, and DKO mice. N=4 mice/genotype. (**E**) Representative images of spleens from WT, *dCK*$^{-/-}$, *TK1*$^{-/-}$, and DKO mice. (**F**) dCTP and dTTP pool measurements from nucleated BM cells from WT, *dCK*$^{-/-}$, *TK1*$^{-/-}$, DKO mice. Data are average value + SEM. N=4 mice/genotype. *, *P*<0.001.

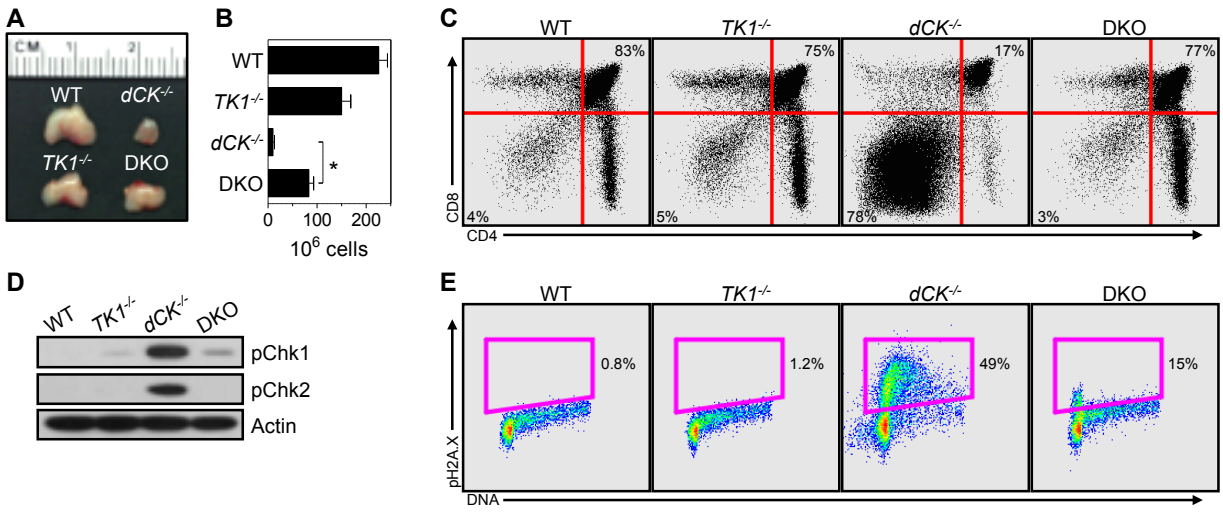

Figure 2.4. TK1 inactivation normalizes the development of *dCK*$^{-/-}$ T cells. (**A-B**) Gross thymus size (**A**), and total viable thymocytes recovered (**B**), from WT, *dCK*$^{-/-}$, *TK1*$^{-/-}$, and DKO mice. Data are average value + SEM. N=5 mice/genotype. *, *P*<0.001. (**C**) Representative example of CD4 and CD8 staining of total thymocytes from WT, *dCK*$^{-/-}$, *TK1*$^{-/-}$, and DKO mice. (**D**) Western blot detection of pChk1 and Chk2 phosphorylated on Thr68 (pChk2) in DN thymocytes. Actin was used as a loading control. (**E**) Representative examples of pH2A.X detection in DN3b thymocytes from WT, *dCK*$^{-/-}$, *TK1*$^{-/-}$, and DKO mice.

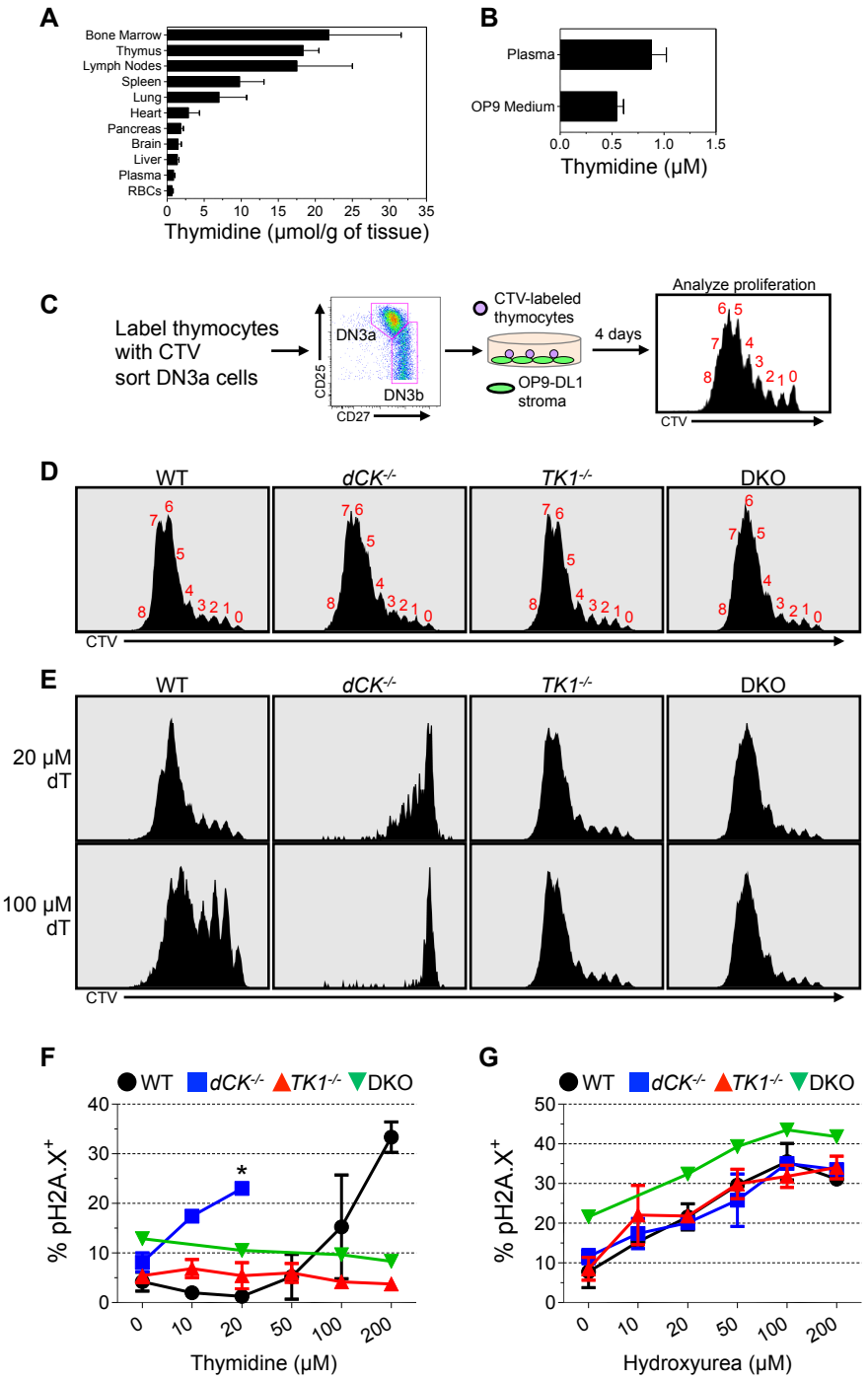

Figure 2.5. Thymidine induces RS in cultured *dCK*$^{-/-}$ thymocytes. (**A**) Relative thymidine abundance in various tissues from C57Bl/6 mice as determined by LC-MS/MS. Concentrations given in μmol/g of whole tissue. Data are average + SEM; N=5/tissue type. (**B**) Concentrations of thymidine given in μM from C57Bl/6 plasma and from standard OP9-DL1 culture medium as determined by LC-MS/MS. Data are

average + SEM; Plasma, N=7; Media, N=3. (**C**) Schematic of the OP9-DL1 co-culture system for *in vitro* proliferation of DN3a thymocytes. Red numbers in the schematic of flow cytometry analysis reflect the total number of completed cell divisions as determined by the generation of CellTrace Violet (CTV) peaks of diluted dye intensity. (**D**) Representative CTV dye dilution curves from WT, *dCK*$^{-/-}$, *TK1*$^{-/-}$, and DKO DN3a thymocytes stimulated on OP9-DL1 stroma for 4 days without thymidine supplementation in the medium. WT, *dCK*$^{-/-}$ and *TK1*$^{-/-}$, N=4; DKO, N=1. (**E**) CTV dye dilution curves after 4 days of stimulation in the presence of 20 and 100 μM thymidine added to the culture medium. WT, *dCK*$^{-/-}$, and *TK1*$^{-/-}$, N=4; DKO, N=1. (**F**) pH2A.X detection in WT, *dCK*$^{-/-}$, *TK1*$^{-/-}$, and DKO DN3b thymocytes after 48 hours of stimulation in increasing concentrations of thymidine. WT, *dCK*$^{-/-}$ and *TK1*$^{-/-}$, N=2; DKO, N=1. *, Cessation of pH2A.X measurement due to >80% sub-G_1 staining in concentrations of 50 μM thymidine or greater. (**G**) pH2A.X expression in WT, *dCK*$^{-/-}$, *TK1*$^{-/-}$, and DKO DN3b thymocytes after 12 hrs of exposure to increasing concentrations of hydroxyurea 36 hrs after plating on OP9-DL1 stroma. WT, *dCK*$^{-/-}$, and *TK1*$^{-/-}$, N=2; DKO, N=1.

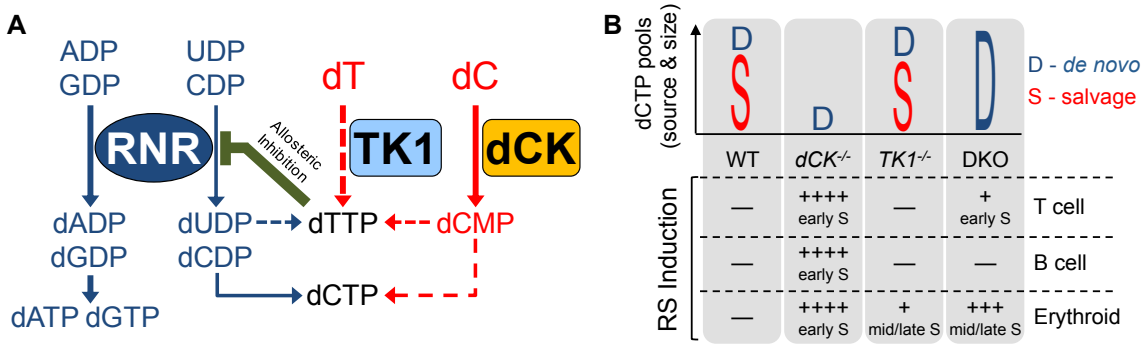

2ure 2.6. Deoxyribonucleoside salvage kinases induce and resolve RS during hematopoiesis. (**A**) Under normal conditions, the ribonucleotide reductase (RNR) complex reduces purine ribonucleotide diphosphates (ADP, GDP) and pyrimidine ribonucleotide diphosphates (CDP, UDP) to contribute to dNTP pools (dATP, dGTP, dTTP, dCTP). While in hematopoietic cells RNR appears to be solely responsible for producing purine dNTP pools, the majority of dTTP pools are produced from salvaged thymidine, which is present in abundant amounts in thymus and bone marrow. dCK may also contribute to dTTP pools as shown in Fig. 2.1 A and Fig. 2.2 C. Elevated dTTP levels prevent RNR from reducing CDP to dCDP and possibly UDP to dUDP via allosteric inhibition. To maintain dCTP pools, rapidly dividing hematopoietic cells rely on deoxycytidine salvage via dCK. (**B**) Graphical representation of the source (D-*de novo*, S-salvage) and size (height of D or S) of dCTP pools in various hematopoietic lineages. In the absence of dCK activity (***dCK*$^{-/-}$ column**), dCTP pools become insufficient, leading to severe RS (++++) and DNA synthesis arrest in early S-phase in T cell, B cell, and erythroid cell precursors. In the absence of TK1 activity (***TK1*$^{-/-}$ column**), dCTP pools are unaffected and only mild RS (+) occurs in late S-phase in erythroid precursors. The mild RS may be due to an imbalanced dUTP/dTTP ratio in the absence of TK1. When both dCK and TK1 are inactivated (**DKO column**), *de novo* dCDP production is de-repressed and subsequently dCTP pools are restored to WT levels. DKO thymocytes have measurable, but overall mild levels of RS (+) in early S-phase. The absence of NSP is well tolerated by B cell precursors, but it results in severe late S-phase RS (+++) in erythroid precursors.

dATP pmol/10^6 cells (+/- SEM)				dGTP pmol/10^6 cells (+/- SEM)			
	DN Thy	**B cells**	**Erythroid**		**DN Thy**	**B cells**	**Erythroid**
WT	**1.08** (+/- 0.62)	**0.64** (+/- 0.37)	**3.71** (+/- 2.15)	**WT**	**3.93** (+/- 2.27)	**0.76** (+/- 0.44)	**1.47** (+/- 0.85)
***dCK*$^{-/-}$**	**0.80** (+/- 0.46)	**1.19** (+/- 0.69)	**2.32** (+/- 1.34)	***dCK*$^{-/-}$**	**2.00** (+/- 1.16)	**0.69** (+/- 0.40)	**2.10** (+/- 1.21)

Table 2.1.

dATP and dGTP pools (pmol/10^6 cells) in WT and *dCK*$^{-/-}$ cells; DN Thy: CD4/CD8 double-negative thymocytes; B cells: bone marrow (BM)-resident B-cell progenitors, and Eryth: BM-resident erythroid progenitors. Data are average value + SEM for 3 independent measurements generated from 4 pooled mice per genotype during each independent measurement.

References

Arlt, M.F., A.C. Ozdemir, S.R. Birkeland, T.E. Wilson, and T.W. Glover. 2011. Hydroxyurea induces de novo copy number variants in human cells. *Proceedings of the National Academy of Sciences of the United States of America* 108:17360-17365.

Arner, E.S., and S. Eriksson. 1995. Mammalian deoxyribonucleoside kinases. *Pharmacology & therapeutics* 67:155-186.

Begg, A.C., N.J. McNally, D.C. Shrieve, and H. Karcher. 1985. A method to measure the duration of DNA synthesis and the potential doubling time from a single sample. *Cytometry* 6:620-626.

Bester, A.C., M. Roniger, Y.S. Oren, M.M. Im, D. Sarni, M. Chaoat, A. Bensimon, G. Zamir, D.S. Shewach, and B. Kerem. 2011. Nucleotide deficiency promotes genomic instability in early stages of cancer development. *Cell* 145:435-446.

Bjursell, G., and P. Reichard. 1973. Effects of thymidine on deoxyribonucleoside triphosphate pools and deoxyribonucleic acid synthesis in Chinese hamster ovary cells. *The Journal of biological chemistry* 248:3904-3909.

Boles, N.C., S. Peddibhotla, A.J. Chen, M.A. Goodell, and J.M. Rosen. 2010. Chk1 haploinsufficiency results in anemia and defective erythropoiesis. *PloS one* 5:e8581.

Branzei, D., and M. Foiani. 2008. Regulation of DNA repair throughout the cell cycle. *Nature reviews* 9:297-308.

Chen, Y.L., S. Eriksson, and Z.F. Chang. 2010. Regulation and functional contribution of thymidine kinase 1 in repair of DNA damage. *The Journal of biological chemistry* 285:27327-27335.

Choi, O., D.A. Heathcote, K.K. Ho, P.J. Muller, H. Ghani, E.W. Lam, P.G. Ashton-Rickardt, and S. Rutschmann. 2012. A deficiency in nucleoside salvage impairs murine lymphocyte development, homeostasis, and survival. *Journal of immunology* 188:3920-3927.

D'Angiolella, V., V. Donato, F.M. Forrester, Y.T. Jeong, C. Pellacani, Y. Kudo, A. Saraf, L. Florens, M.P. Washburn, and M. Pagano. 2012. Cyclin F-mediated degradation of ribonucleotide reductase M2 controls genome integrity and DNA repair. *Cell* 149:1023-1034.

Dobrovolsky, V.N., T. Bucci, R.H. Heflich, J. Desjardins, and F.C. Richardson. 2003. Mice deficient for cytosolic thymidine kinase gene develop fatal kidney disease. *Molecular genetics and metabolism* 78:1-10.

Dobrovolsky, V.N., L.J. McGarrity, L.S. VonTungeln, R.A. Mittelstaedt, S.M. Morris, F.A. Beland, and R.H. Heflich. 2005. Micronucleated erythrocyte frequency in control and azidothymidine-treated Tk+/+, Tk+/- and Tk-/- mice. *Mutation research* 570:227-235.

Eriksson, S., and L. Wang. 2008. Molecular mechanisms of mitochondrial DNA depletion diseases caused by deficiencies in enzymes in purine and pyrimidine metabolism. *Nucleosides, nucleotides & nucleic acids* 27:800-808.

Evans, D.R., and H.I. Guy. 2004. Mammalian pyrimidine biosynthesis: fresh insights into an ancient pathway. *The Journal of biological chemistry* 279:33035-33038.

Fairman, J.W., S.R. Wijerathna, M.F. Ahmad, H. Xu, R. Nakano, S. Jha, J. Prendergast, R.M. Welin, S. Flodin, A. Roos, P. Nordlund, Z. Li, T. Walz, and C.G. Dealwis. 2011. Structural basis for allosteric regulation of human ribonucleotide reductase by nucleotide-induced oligomerization. *Nature structural & molecular biology* 18:316-322.

Fustin, J.M., M. Doi, H. Yamada, R. Komatsu, S. Shimba, and H. Okamura. 2012. Rhythmic nucleotide synthesis in the liver: temporal segregation of metabolites. *Cell reports* 1:341-349.

Gagou, M.E., P. Zuazua-Villar, and M. Meuth. 2010. Enhanced H2AX phosphorylation, DNA replication fork arrest, and cell death in the absence of Chk1. *Molecular biology of the cell* 21:739-752.

Gandhi, V.V., and D.C. Samuels. 2011. A review comparing deoxyribonucleoside triphosphate (dNTP) concentrations in the mitochondrial and cytoplasmic compartments of normal and transformed cells. *Nucleosides, nucleotides & nucleic acids* 30:317-339.

Gentry, G.A. 1992. Viral thymidine kinases and their relatives. *Pharmacology & therapeutics* 54:319-355.

Gonzalez-Vioque, E., J. Torres-Torronteras, A.L. Andreu, and R. Marti. 2011. Limited dCTP availability accounts for mitochondrial DNA depletion in mitochondrial neurogastrointestinal encephalomyopathy (MNGIE). *PLoS genetics* 7:e1002035.

Hagen, L., J. Pena-Diaz, B. Kavli, M. Otterlei, G. Slupphaug, and H.E. Krokan. 2006. Genomic uracil and human disease. *Experimental cell research* 312:2666-2672.

Halazonetis, T.D., V.G. Gorgoulis, and J. Bartek. 2008. An oncogene-induced DNA damage model for cancer development. *Science (New York, N.Y* 319:1352-1355.

Hardy, R.R., P.W. Kincade, and K. Dorshkind. 2007. The protean nature of cells in the B lymphocyte lineage. *Immunity* 26:703-714.

He, Q., and S. Skog. 2002. Involvement of a substrate cycle between thymidine and thymidylate in the regulation of DNA precursor pool in ehrlich ascites tumour. *Cellular physiology and biochemistry : international journal of experimental cellular physiology, biochemistry, and pharmacology* 12:305-314.

Hu, C.M., M.T. Yeh, N. Tsao, C.W. Chen, Q.Z. Gao, C.Y. Chang, M.H. Lee, J.M. Fang, S.Y. Sheu, C.J. Lin, M.C. Tseng, Y.J. Chen, and Z.F. Chang. 2012. Tumor Cells Require Thymidylate Kinase to Prevent dUTP Incorporation during DNA Repair. *Cancer cell* 22:36-50.

Kufe, D.W., P. Beardsley, D. Karp, L. Parker, A. Rosowsky, G. Canellos, and E. Frei, 3rd. 1980. High-dose thymidine infusions in patients with leukemia and lymphoma. *Blood* 55:580-589.

Larsson, K.M., A. Jordan, R. Eliasson, P. Reichard, D.T. Logan, and P. Nordlund. 2004. Structural mechanism of allosteric substrate specificity regulation in a ribonucleotide reductase. *Nature structural & molecular biology* 11:1142-1149.

Liu, Y., R. Pop, C. Sadegh, C. Brugnara, V.H. Haase, and M. Socolovsky. 2006. Suppression of Fas-FasL coexpression by erythropoietin mediates erythroblast expansion during the erythropoietic stress response in vivo. *Blood* 108:123-133.

Lunt, S.Y., and M.G. Vander Heiden. 2011. Aerobic glycolysis: meeting the metabolic requirements of cell proliferation. *Annual review of cell and developmental biology* 27:441-464.

Mathews, C.K., and L.J. Wheeler. 2009. Measuring DNA precursor pools in mitochondria. *Methods in molecular biology (Clifton, N.J* 554:371-381.

Matsuoka, S., B.A. Ballif, A. Smogorzewska, E.R. McDonald, 3rd, K.E. Hurov, J. Luo, C.E. Bakalarski, Z. Zhao, N. Solimini, Y. Lerenthal, Y. Shiloh, S.P. Gygi, and S.J. Elledge. 2007. ATM and ATR substrate analysis reveals extensive protein networks responsive to DNA damage. *Science (New York, N.Y* 316:1160-1166.

Melnyk, S., M. Pogribna, B.J. Miller, A.G. Basnakian, I.P. Pogribny, and S.J. James. 1999. Uracil misincorporation, DNA strand breaks, and gene amplification are associated with tumorigenic cell transformation in folate deficient/repleted Chinese hamster ovary cells. *Cancer letters* 146:35-44.

Munch-Petersen, B., L. Cloos, G. Tyrsted, and S. Eriksson. 1991. Diverging substrate specificity of pure human thymidine kinases 1 and 2 against antiviral dideoxynucleosides. *The Journal of biological chemistry* 266:9032-9038.

Murga, M., S. Bunting, M.F. Montana, R. Soria, F. Mulero, M. Canamero, Y. Lee, P.J. McKinnon, A. Nussenzweig, and O. Fernandez-Capetillo. 2009. A mouse model of ATR-Seckel shows embryonic replicative stress and accelerated aging. *Nature genetics* 41:891-898.

Niida, H., M. Shimada, H. Murakami, and M. Nakanishi. 2010. Mechanisms of dNTP supply that play an essential role in maintaining genome integrity in eukaryotic cells. *Cancer science* 101:2505-2509.

Poli, J., O. Tsaponina, L. Crabbe, A. Keszthelyi, V. Pantesco, A. Chabes, A. Lengronne, and P. Pasero. 2012. dNTP pools determine fork progression and origin usage under replication stress. *The EMBO journal* 31:883-894.

Pontarin, G., P. Ferraro, L. Bee, P. Reichard, and V. Bianchi. 2012. Mammalian ribonucleotide reductase subunit p53R2 is required for mitochondrial DNA replication and DNA repair in quiescent cells. *Proceedings of the National Academy of Sciences of the United States of America*

Reichard, P. 1988. Interactions between deoxyribonucleotide and DNA synthesis. *Annual review of biochemistry* 57:349-374.

Sabini, E., S. Hazra, S. Ort, M. Konrad, and A. Lavie. 2008. Structural basis for substrate promiscuity of dCK. *Journal of molecular biology* 378:607-621.

Staub, M., T. Spasokukotskaja, M. Benczur, and F. Antoni. 1988. DNA synthesis and nucleoside metabolism in human tonsillar lymphocyte subpopulations. *Acta oto-laryngologica. Supplementum* 454:118-124.

Taghon, T., M.A. Yui, R. Pant, R.A. Diamond, and E.V. Rothenberg. 2006. Developmental and molecular characterization of emerging beta- and gammadelta-selected pre-T cells in the adult mouse thymus. *Immunity* 24:53-64.

Taghon, T.N., E.S. David, J.C. Zuniga-Pflucker, and E.V. Rothenberg. 2005. Delayed, asynchronous, and reversible T-lineage specification induced by Notch/Delta signaling. *Genes & development* 19:965-978.

Terry, N.H., and R.A. White. 2006. Flow cytometry after bromodeoxyuridine labeling to measure S and G2+M phase durations plus doubling times in vitro and in vivo. *Nature protocols* 1:859-869.

Toy, G., W.R. Austin, H.I. Liao, D. Cheng, A. Singh, D.O. Campbell, T.O. Ishikawa, L.W. Lehmann, N. Satyamurthy, M.E. Phelps, H.R. Herschman, J. Czernin, O.N. Witte, and C.G. Radu. 2010. Requirement for deoxycytidine kinase in T and B lymphocyte development. *Proceedings of the National Academy of Sciences of the United States of America* 107:5551-5556.

Voet, D., Voet J.G. 2004. Biochemistry. J. Wiley & Sons, Hoboken, NJ.

Xeros, N. 1962. Deoxyriboside control and synchronization of mitosis. *Nature* 194:682-683.

Zhou, X., M. Johansson, N. Solaroli, B. Rozell, A. Grandien, and A. Karlsson. 2010. Hematopoiesis in the thymidine kinase 2 deficient mouse model of mitochondrial DNA depletion syndrome. *Journal of inherited metabolic disease* 33:231-236.

Zhou, X., N. Solaroli, M. Bjerke, J.B. Stewart, B. Rozell, M. Johansson, and A. Karlsson. 2008. Progressive loss of mitochondrial DNA in thymidine kinase 2-deficient mice. *Human molecular genetics* 17:2329-2335.

CHAPTER 3

Development of new deoxycytidine kinase inhibitors and non-invasive *in vivo* evaluation using Positron Emission Tomography

Abstract

Combined inhibition of ribonucleotide reductase and deoxycytidine kinase (dCK) in multiple cancer cell lines depletes deoxycytidine triphosphate pools leading to DNA replication stress, cell cycle arrest and apoptosis. Evidence implicating dCK in cancer cell proliferation and survival stimulated our interest in developing small molecule dCK inhibitors. Following a high throughput screen of a diverse chemical library, a structure-activity relationship study was carried out. Positron Emission Tomography (PET) using ^{18}F-L-1-(2'-deoxy-2'-**F**luoro**A**rabinofuranosyl) **C**ytosine (^{18}F-L-FAC), a dCK-specific substrate, was used to rapidly rank lead compounds based on their ability to inhibit dCK activity *in vivo.* Evaluation of a subset of the most potent compounds in cell culture (IC_{50} = ~1 – 12 nM) using the ^{18}F-L-FAC PET pharmacodynamic assay identified compounds demonstrating superior *in vivo* efficacy.

Introduction

Mammalian cells rely on two major pathways for the production and maintenance of deoxyribonucleotide triphosphates (dNTPs) for DNA replication and repair: the *de novo* pathway and the nucleoside salvage pathway (Reichard, 1988). The *de novo* pathway produces dNTPs from glucose and amino acids. The nucleoside salvage pathway produces dNTPs from preformed deoxyribonucleosides present in the extracellular environment (Reichard, 1988). The first enzymatic step in the cytosolic deoxyribonucleoside salvage pathway is catalyzed by deoxycytidine kinase (dCK) and by thymidine kinase 1 (TK1) (Arner and Eriksson, 1995). dCK catalyzes 5'-phosphorylation of deoxycytidine (dC), deoxyguanosine (dG) and deoxyadenosine (dA) to their monophosphate forms, exhibiting the highest affinity for dC (Sabini et al., 2008). The monophosphate deoxyribonucleotides are subsequently phosphorylated to their corresponding di- and triphosphate forms by other kinases (Krishnan et al., 2003; Pasti et al., 2003). We have shown that dCK and TK1 play important roles in hematopoiesis by regulating dNTP biosynthesis in lymphoid and erythroid progenitors (Austin et al., 2012; Toy et al., 2010). In addition to its physiological role in nucleotide metabolism, dCK phosphorylates several clinically important antiviral and anticancer nucleoside analog prodrugs (e.g. gemcitabine, decitabine, fludarabine, cytarabine, clofarabine); phosphorylation by dCK is critically required for the activation of these prodrugs (Van Rompay et al., 2003). Recently, dCK was implicated in the regulation of the G2/M checkpoint in cancer cells in response to DNA damage (Yang et al., 2012). The role of dCK in hematopoiesis and cancer has led to our interest in developing a small molecule inhibitor of this kinase. Such dCK inhibitors could represent new therapeutic agents for

malignancies and immune disorders. To our knowledge, few dCK inhibitors have been reported (Tarver et al., 2009; Ward and Baker, 1977; Yu et al., 2010), and only one (Jessop et al., 2009) has been demonstrated to inhibit dCK activity *in vivo*.

Positron emission tomography (PET) is a non-invasive *in vivo* imaging technique widely used for diagnosing, staging, restaging and therapy monitoring of various diseases (Czernin et al., 2010; Weber et al., 2008). While PET using the radiotracer 2-^{18}F-fluoro-2-deoxy-D-glucose (^{18}F-FDG) (Gambhir, 2002; Rigo et al., 1996) has become an important diagnostic and treatment monitoring tool in cancer (Jadvar et al., 2009; Oriuchi et al., 2006; Weber, 2006; Wood et al., 2007), another emerging application of PET concerns its use in drug discovery and development. Thus, by facilitating faster and more effective decision-making early in the drug discovery/development process, PET could accelerate the advancement of promising candidates and reduce failures (Hargreaves, 2008; Wagner et al., 2008; Wang and Maurer, 2005). For instance, PET can be used to demonstrate the need to modify lead candidates early in the drug discovery process by enabling non-invasive evaluations of drug pharmacodynamic (PD) and/or pharmacokinetic (PK) properties. In the specific context of our drug discovery and development program centered on dCK, PET could play a particularly important role given the availability of validated PET biomarkers to assess dCK activity *in vivo*. These PET PD biomarkers of dCK activity include a series of ^{18}F-Fluoro-arabinofuranosylcytosine analogs substrates of dCK developed by our group (Laing et al., 2009) which include ^{18}F-1-(2'-deoxy-2'-**F**luoro**A**rabinofuranosyl) **C**ytosine (^{18}F-FAC) (Radu et al., 2008) and ^{18}F-L-1-(2'-deoxy-2'-**F**luoro**A**rabinofuranosyl) **C**ytosine (^{18}F-L-

FAC) (Shu et al., 2010). Herein we describe the development of potent dCK inhibitors and demonstrate their *in vivo* efficacy using ^{18}F-L-FAC PET as a non-invasive and clinically applicable PD biomarker.

Materials and Methods

High-throughput Screen. Recombinant human dCK at a concentration of 1 μM was incubated with 10 μM of drug, 10 μM of dC and 0.5 μM ATP with 50 mM Tris (pH 7.6), 5 mM $MgCl_2$, 2 mM DTT. The reaction was incubated at 37°C for 4 hours before adding CellTiter-Glo (Promega): Briefly, 40 μL dCK enzyme were dispensed into 384 well plates (Greiner, Bahlingen, Germany) using a multidrop 384 (Thermo, Turku, Finnland) at concentration of 12.5 μg/ml; compounds were added using a Beckman-Coulter Biomek FX (Beckman Coulter, Brea, CA) equipped with a 500 nL custom pin tool (V&P Scientific, San Diego, CA). Columns 1, 2, 23 and 24 received only DMSO instead of any drugs. In addition, no dCK was added to column 23 and 24 as these columns served as additional controls (see below). After 30 min incubation at 37°C, dC and ATP were added to a final concentration of 10 μM and 0.5 μM, respectively for columns 1-22 using the multidrop in a volume of 10 μL. For column 23 and 24 the following controls were used: 10 μl of a 2.5 μM ATP solution containing the following additional controls was added: for wells A-D23, 1 μM dCTP, for wells E-H23 10 μM dCTP, for wells I-L23 10 μM L-FAC, for wells F-P23: 10 μM FAC, for wells A-D24: 0.5 μM ATP standard, for wells E-H24: 0.1 μM ATP standard, for wells I-L24 1 μM DCK only and for wells F-P24 10 μM UTP was added, respectively. These controls were included on each plate to exclude equipment failure. This was followed by a 4 hour incubation at 37°C and addition of 25 μL Cell titer glo reagent (Promega, Fitchburg, WI) by multidrop followed by reading on an Acquest plate reader (Molecular Devices, Sunnyvale, CA). The libraries used were custom sets of compounds from the compound manufacturers Asinex (Winston-Salem, NC) and Enamine (Monmouth Jct., NJ). These sets consisted of compounds selected

extensively for drug-likeness using the Lipinski rule of five, rotatable bonds and maximal diversity using custom clustering algorithms.

Chemistry. ***General Procedures:*** Unless otherwise noted, reactions were carried out in oven-dried glassware under an atmosphere of nitrogen using commercially available anhydrous solvents. Solvents used for extractions and chromatography were not anhydrous. 4,6-Diamino-2-mercapto-pyrimidine was obtained from drying the hydrate over dynamic vacuum at 110 ^{o}C for 20 hours. All other reagents obtained from commercial suppliers were reagent grade and used without further purification unless specified. Reactions and chromatography fractions were analyzed by thin-layer chromatography (TLC) using Merck precoated silica gel 60 F_{254} glass plates (250 μm). Visualization was carried out with ultraviolet light, vanillin stain, permanganate stain, or *p*-anisaldehyde stain. Flash column chromatography was performed using E. Merck silica gel 60 (230-400 mesh) with compressed air. ^{1}H and ^{13}C NMR spectra were recorded on ARX500 (500 MHz) or Avance500 (500 MHz) spectrometers. Chemical shifts are reported in parts per million (ppm, δ) using the residual solvent peak as the reference. DMSO-d_6 (δ 2.50 ppm for ^{1}H; δ 39.5 ppm for ^{13}C) was used as the solvent and reference standards unless otherwise noted. The coupling constants, *J*, are reported in Hertz (Hz) and the resonance patterns are reported with notations as the following: br (broad), s (singlet), d (doublet), t (triplet), q (quartet), and m (multiplet). Electrospray mass spectrometry data were collected with a Waters LCT Premier XE time of flight instrument controlled by MassLynx 4.1 software. Samples were dissolved in methanol and infused using direct loop injection from a Waters Acquity UPLC into the

Multi-Mode Ionization source. The purity of all final compounds was determined to be >95%. Analytical HPLC analysis was performed on a Knauer Smartline HPLC system with a Phenomenex reverse-phase Luna column (5 µm, 4.6 x 250 mm) with inline Knauer UV (254 nm) detector. Mobile phase: A: 0.1% TFA in H_2O, B: 0.1% TFA in MeCN. Eluent gradient is specified for each described compound in the supporting information. All chromatograms were collected by a GinaStar (raytest USA, Inc.; Wilmington, NC, USA) analog to digital converter and GinaStar software (raytest USA, Inc.).

General Procedure for the Synthesis of Compounds 15a – c. 3-(2-fluoroethoxy)-4-methoxybenzonitrile (20). To a solution of 3-hydroxy-4methoxybenzonitrile **19** (3.0 g, 20.1 mmol) in DMF (100 mL) was added Cs_2CO_3 (10.5 g, 32.2 mmol) and 1-bromo-2-fluoroethane (5.1 g, 40.2 mmol). The mixture was stirred for 18 h at 50 ^oC. After concentration to remove residual solvent, the resulting residue was washed with brine and extracted with ethyl acetate. The organic layer was washed with water three times, dried over anhydrous $MgSO_4$ and concentrated *in vacuo* to yield crude **20** (3.91 g, 20.03 mmol, 99%) as an cream-colored solid. ^1H NMR (500 MHz, $CDCl_3$) δ: 7.28 (dd, J = 8.5, 2.0 Hz, 1H), 7.10 (d, J = 2.0 Hz, 1H), 6.90 (d, J = 8.5 Hz, 1H), 4.83 – 4.81 (m, 1H), 4.73 – 4.71 (m, 1H), 4.28 – 4.26 (m, 1H), 4.23 – 4.21 (m, 1H), 3.89 (s, 3H); ^{13}C NMR (125 MHz, $CDCl_3$) δ: 153.6, 148.1, 127.3, 119.1, 116.5, 111.9, 103.8, 82.3 (d, J_{CF} = 170.5 Hz), 68.7 (d, J_{CF} = 20.3 Hz), 56.1.

3-(2-fluoroethoxy)-4-methoxybenzothioamide (21). To a mixture of **20** (3.86 g, 19.8 mmol) in pyridine (41 mL) and triethylamine (3 mL) was added ammonium sulfide solution (20% wt. in H_2O, 13.52 mL, 39.6 mmol). The mixture was stirred for 18 h at 60

^{o}C. The reaction mixture was cooled and concentrated *in vacuo* to remove residual solvent. The resulting residue was washed with brine and extracted with ethyl acetate. The organic layer was dried over anhydrous $MgSO_4$ and concentrated *in vacuo* to yield **21** (4.5 g, 19.8 mmol, quantitative) as a yellow-orange solid. ^{1}H NMR (500 MHz, acetone-d_6) δ: 8.81 (brs, 1H), 8.74 (brs, 1H), 7.73 (s, 1H), 7.72 (dd, *J* = 8.5, 2.0 Hz, 1H), 7.00 (d, *J* = 8.0 Hz, 1H), 4.79 (dt, *J* = 48.0, 4.0 Hz, 2H), 4.32 (dt, *J* = 29.5, 4.0 Hz, 2H), 3.89 (s, 3H); ^{13}C NMR (125 MHz, acetone-d_6) δ: 200.4, 152.9, 147.2, 131.8, 121.5, 113.6, 110.8, 82.7 (d, J_{CF} = 167.3 Hz), 68.5 (d, J_{CF} = 19.6 Hz), 55.4.

Ethyl 2-(3-(2-fluoroethoxy)-4-methoxyphenyl)-5-methylthiazole-4-carboxylate (22a). A mixture of thioamide **21** (1.50 g, 6.5 mmol) and ethyl 3-bromo-2-oxobutanoate (2.72 g, 13.0 mmol) in ethanol (32 mL) was stirred under refluxing conditions for 2.5 h. The resulting mixture was cooled and concentrated *in vacuo* to remove residual solvent. The crude residue was purified by flash column chromatography over silica gel (10:3 hexanes:ethyl acetate) to yield the desired thiazole intermediate **22a** (1.45 g, 4.3 mmol, 65%) as a light brown solid. ^{1}H NMR (500 MHz, DMSO-d_6) δ: 7.40 (dd, *J* = 8.5, 2.0 Hz, 1H), 7.37 (d, *J* = 2.0 Hz, 1H), 7.04 (d, *J* = 8.5 Hz, 1H), 4.72 (dt, *J* = 48.0, 4.0 Hz, 2H), 4.31 – 4.22 (m, 2H), 4.28 (q, *J* = 7.0 Hz, 2H), 3.81 (s, 3H), 2.67 (s, 3H), 1.28 (t, *J* = 7.0 Hz, 3H); ^{13}C NMR (125 MHz, DMSO-d_6) δ: 162.9, 162.1, 151.4, 148.2, 143.9, 141.9, 125.5, 120.5, 112.6, 110.8, 83.1 (d, J_{CF} = 165.9 Hz), 68.3 (d, J_{CF} = 19.0 Hz), 60.8, 56.0, 14.5, 13.3.

(2-(3-(2-fluoroethoxy)-4-methoxyphenyl)-5-methylthiazol-4-yl)methanol (23a). To a stirred solution of intermediate **22a** (860 mg, 2.5 mmol) in CH_2Cl_2 (30 mL) cooled to 0 ^{o}C was added slowly diisobutylaluminum hydride (1.0M in THF, 10 mmol, 10 mL). The

reaction was allowed to warm to 23 ^{o}C and stirred for 1 h. The mixture was cooled to 0 ^{o}C and slowly quenched with a saturated aqueous solution of Rochelle's salt. The cloudy solution was stirred for 1 h at 23 ^{o}C until the solution became clear again. The resulting solution was extracted with ethyl acetate, washed with brine, dried over anhydrous magnesium sulfate and concentrated *in vacuo* to give the desired alcohol **23a** (654 mg, 2.2 mmol, 88%) as a pale yellow solid. ^{1}H NMR (500 MHz, DMSO-d_6) δ: 7.39 (d, *J* = 2.0 Hz, 1H), 7.36 (dd, *J* = 8.5, 2.0 Hz, 1H), 7.02 (d, *J* = 8.5 Hz, 1H), 5.04 (t, *J* = 5.5 Hz, 1H), 4.73 (dt, *J* = 48.0, 3.5 Hz, 2H), 4.46 (d, *J* = 5.5 Hz, 2H), 4.25 (dt, *J* = 30.0, 3.5 Hz, 2H), 3.79 (s, 3H), 2.41 (s, 3H); ^{13}C NMR (125 MHz, DMSO-d_6) δ: 162.7, 153.2, 150.8, 148.2, 129.5, 126.5, 119.8, 112.5, 110.4, 83.1 (d, J_{CF} = 165.9 Hz), 68.4 (d, J_{CF} = 18.5 Hz), 57.3, 55.9, 11.2.

4-(bromomethyl)-2-(3-(2-fluoroethoxy)-4-methoxyphenyl)-5-methylthiazole (24a). To a solution of **23a** (1.90 g, 6.4 mmol) in acetonitrile (30 mL) was added PPh_3 (2.5 g, 9.6 mmol) followed by hexabromoacetone (1.70 g, 3.2 mmol) at 23 ^{o}C. The mixture was stirred for 1 h at 40 ^{o}C when, by TLC analysis, all starting material had been consumed. The solvent was removed *in vacuo* and the crude residue was purified by flash column chromatography over silica gel (10:3 hexanes:ethyl acetate) to give the desired bromide **24a** (1.84 g, 5.1 mmol, 80%) as a light brown solid. ^{1}H NMR (500 MHz, $CDCl_3$) δ: 7.50 (d, *J* = 2.0 Hz, 1H), 7.40 (dd, *J* = 8.5, 2.0 Hz, 1H), 6.88 (d, *J* = 8.0 Hz, 1H), 4.81 (dt, *J* = 47.0, 4.0 Hz, 2H), 4.59 (s, 2H), 4.36 (dt, *J* = 27.5, 4.0 Hz, 2H), 3.90 (s, 3H), 2.46 (s, 3H); ^{13}C NMR (125 MHz, $CDCl_3$) δ: 164.1, 151.2, 148.1, 148.0, 131.7, 126.4, 120.4, 111.6, 111.5, 82.4 (d, J_{CF} = 169.9 Hz), 68.4 (d, J_{CF} = 20.5 Hz), 55.9, 25.8, 11.4.

2-(((2-(3-(2-fluoroethoxy)-4-methoxyphenyl)-5-methylthiazol-4-yl)methyl)thio)pyrimidine-4,6-diamine (15a). 4,6-diamino-2-mercaptopyrimidine (336 mg, 2.36 mmol) and NaOH (94 mg, 2.36 mmol) were stirred in ethanol (20 mL) for 10 min at 23 ^{o}C. To the reaction mixture was added a solution of bromide **24a** (710 mg, 1.97 mmol) in hot ethanol (16 mL) and the resulting mixture was stirred for 3 h at 70 ^{o}C. The solution was cooled, concentrated in vacuo and purified by flash column chromatography over silica gel (100:5 dichloromethane:methanol) to give the desired product **15a** (590 mg, 1.40 mmol, 71%) as a pale yellow solid. ^{1}H NMR (500 MHz, DMSO-d_6) δ: 7.36 (s, 1H), 7.34 (d, *J* = 8.0 Hz, 1H), 7.02 (d, *J* = 8.5 Hz, 1H), 6.09 (brs, 4H), 5.12 (s, 1H), 4.72 (dt, *J* = 48.0, 3.5 Hz, 2H), 4.32 (s, 2H), 4.25 (dt, *J* = 30.5, 3.5 Hz, 2H), 3.78 (s, 3H), 2.43 (s, 3H); ^{13}C NMR (125 MHz, DMSO-d_6) δ: 168.3, 163.9 (2), 163.3, 150.9, 149.5, 148.3, 129.1, 126.4, 119.9, 112.7, 110.5, 83.2 (d, J_{CF} = 165.9 Hz), 79.5, 68.5 (d, J_{CF} = 18.7 Hz), 56.1, 27.9, 11.7; HRMS-ESI (*m/z*) $[M + H]^+$ calcd for $C_{18}H_{20}FN_5O_2S_2$ H, 422.1121; found 422.1136.

2-(((5-ethyl-2-(3-(2-fluoroethoxy)-4-methoxyphenyl)thiazol-4-yl)methyl)thio)pyrimidine-4,6-diamine (15b). ^{1}H NMR (500 MHz, DMSO-d_6) δ: 7.37 (dd, *J* = 8.0, 2.0 Hz, 1H), 7.36 (s, 1H), 7.02 (d, *J* = 8.5 Hz, 1H), 6.13 (brs, 4H), 5.13 (s, 1H), 4.72 (dt, *J* = 47.5, 4.0 Hz, 2H), 4.34 (s, 1H), 4.25 (dt, *J* = 30.5, 4.0 Hz, 2H), 3.79 (s, 3H), 2.87 (q, *J* = 7.5 Hz, 2H), 1.17 (t, *J* = 7.5 Hz, 3H); ^{13}C NMR (125 MHz, DMSO-d_6) δ: 168.2, 163.8 (2), 163.5, 151.0, 148.4, 148.3, 136.9, 126.5, 119.9, 112.7, 110.5, 83.3 (d, J_{CF} = 165.9 Hz), 79.5, 68.5 (d, J_{CF} = 18.8 Hz), 56.1, 28.0, 19.9, 17.1; HRMS-ESI (*m/z*) $[M + H]^+$ calcd for $C_{19}H_{22}FN_5O_2S_2$ H, 436.1277; found 436.1263.

2-(((2-(3-(2-fluoroethoxy)-4-methoxyphenyl)-5-propylthiazol-4-yl)methyl)thio)pyrimidine-4,6-diamine (15c). ^{1}H NMR (500 MHz, acetone-d_6) δ: 7.53 (d, *J* = 2.0 Hz, 1H), 7.46 (dd, *J* = 8.5, 2.0 Hz, 1H), 7.03 (d, *J* = 8.5 Hz, 1H), 5.63 (brs, 4H), 5.38 (s, 1H), 4.80 (dt, *J* = 48.0, 4.0 Hz, 2H), 4.45 (s, 2H), 4.34 (dt, *J* = 29.5, 4.0 Hz, 2H), 3.87 (s, 3H), 2.91 (t, *J* = 7.5 Hz, 1H), 1.66 (qt, *J* = 7.5, 7.5 Hz, 2H), 0.97 (t, *J* = 7.5 Hz, 3H); ^{13}C NMR (125 MHz, acetone-d_6) δ: 169.2, 164.0 (2), 163.9, 163.6, 151.4, 149.0, 148.5, 134.6, 126.9, 119.8, 112.1, 111.1, 82.8 (d, J_{CF} = 167.5 Hz), 79.5, 68.6 (d, J_{CF} = 19.5 Hz), 55.3, 28.1, 25.2, 13.0; HRMS-ESI (*m/z*) $[M + H]^+$ calcd for $C_{20}H_{24}FN_5O_2S_2$ H, 450.1434; found 450.1432.

1-(5-(4-(((4,6-diaminopyrimidin-2-yl)thio)methyl)-5-propylthiazol-2-yl)-2-methoxyphenoxy)-2-methylpropan-2-ol (36). ^{1}H NMR (500 MHz, MeOD) δ: 7.51 (d, *J* = 2.0 Hz, 1H), 7.39 (dd, *J* = 8.5, 2.0 Hz, 1H), 7.00 (d, *J* = 8.5 Hz, 1H), 5.48 (s, 1H), 5.32 (s, 1H), 4.48 (s, 2H), 3.89 (s, 3H), 3.86 (s, 2H), 2.88 (t, *J* = 7.5 Hz, 2H), 1.67 (qt, *J* = 7.5, 7.5 Hz, 2H), 1.33 (s, 6H), 0.98 (t, *J* = 7.5 Hz, 3H); ^{13}C NMR (125 MHz, MeOD) δ: 168.8, 165.2, 163.8 (2), 151.2, 148.9, 148.0, 135.4, 126.4, 119.7, 111.8, 110.7, 79.2, 77.0, 69.6, 55.2, 48.4, 27.9, 27.8, 25.0, 24.9, 12.6; HRMS-ESI (*m/z*) $[M + H]^+$ calcd for $C_{22}H_{29}N_5O_3S_2$ H, 476.1790; found 476.1772.

N-(2-(5-(4-(((4,6-diaminopyrimidin-2-yl)thio)methyl)-5-propylthiazol-2-yl)-2-methoxyphenoxy)ethyl)methanesulfonamide (37). ^{1}H NMR (500 MHz, DMSO-d_6) δ: 7.41 (dd, *J* = 7.5, 2.0 Hz, 1H), 7.39 (s, 1H), 7.25 (t, *J* = 6.0 Hz, 1H), 7.05 (d, *J* = 8.5 Hz, 1H), 6.13 (brs, 4H), 5.15 (s, 1H), 4.39 (s, 2H), 4.07 (t, *J* = 5.5 Hz, 2H), 3.80 (s, 3H), 3.36 (dt, *J* = 5.5, 5.5 Hz, 2H), 3.15 (d, *J* = 5.5 Hz, 1H), 2.98 (s, 3H), 2.84 (t, *J* = 7.5 Hz, 2H), 1.58 (qt, *J* = 7.5, 7.5 Hz, 2H), 0.91 (t, *J* = 7.5 Hz, 3H); ^{13}C NMR (125 MHz, DMSO-d_6) δ:

168.3, 163.9 (2), 163.7, 151.1,149.1, 148.3, 135.0, 126.5, 119.9, 112.7, 110.6, 79.5, 68.3, 60.2, 42.4, 31.2, 28.2, 28.0, 25.4, 13.9; HRMS-ESI (*m/z*) $[M + H]^+$ calcd for $C_{21}H_{28}N_6O_4S_3$ H, 525.1412; found 525.1404.

dCK Uptake Assay Performed in Cell Culture. The murine leukemic line L1210 was a gift from Charles Dumontet (Université Claude Bernard Lyon I, Lyon, France). The human lymphoma line CCRF-CEM was provided by Margaret Black (Washington State University). All L1210 and CCRF-CEM cell lines were cultured in RPMI medium 1640, supplemented with 5% FCS in a 5% CO_2 37 °C incubator. For the uptake assays cells were seeded at a density of 50,000 cells/well in Millipore MultiScreen GV 96 well plates. 0.25 μCi of ^{3}H-dC (Moravek Biochemicals) were added to the cells simultaneously with concentrations of dCK inhibitor at a final volume of 100 μL/well. After 1 h at 37 °C, cells were washed four times with ice cold phosphate-buffered saline (PBS) using the Millipore Vacuum Manifold. The amount of incorporated probe was measured by scintillation counting with the PerkinElmer Microbeta.

Protein expression and purification. Details on C4S S74E dCK variant expression and purification are detailed in Nomme et *al.*

Crystallization, X-ray Data Collection, and Refinement. Crystallization, data collection and structure determination of dCK in complex with **15a** and **36** were performed following the general procedure as detailed in Nomme *et al*. Specifically for compound **36**, crystals of dCK in complex with UDP, $MgCl_2$ and a 2.5-fold excess of the

36 inhibitor were grown using the hanging drop vapor diffusion method at 12 ºC. The reservoir solution contained 0.9 - 1.5 M trisodium citrate dehydrate and 25 mM HEPES (pH 7.5). Diffraction data were collected at the Advanced Photon Source, Argonne National Laboratory on Life Sciences-Collaborative Access Team (LS-CAT) beamlines 21 ID-G.

Kinetic assay. Steady state kinetic assay and data fitting were performed as described in Nomme *et al.*

Computational Modeling. All simulations were performed using the *MCPRO 2.0* package (Jorgensen and Tirado-Rives, 2005). Initial coordinates were obtained from the X-ray structure of dCK in complex with compound **15c**. The protein was solvated in a 30 Å water cap, represented by the TIP4P (Jorgensen et al., 1983) classical water model. Solute atoms were represented by the OPLS-AA force field (Jorgensen et al., 1996) was used. Equilibrations were performed using Metropolis Monte Carlo (MC) in the NPT ensemble at 25 ^{o}C and 1 atm. The backbone of the protein and all bond lengths within the protein were fixed; angles and torsions within 11 Å from the center of the bound molecule were sampled. All degrees of freedom of the inhibitor compound were sampled during equilibration simulations. Equilibration consisted of 5 x 10^6 configurations of sampling in which only solvent moves were allowed, and of 10 x 10^6 subsequent configurations for the protein-inhibitor complex and for the lone inhibitor in solution. The equilibrated systems were then subject to free energy perturbation (FEP)/MC simulations. These simulations consisted of 14 perturbing steps of double-

wide sampling. During FEP, the system underwent 5 x 10^6 configurations of solvent equilibration, followed by 10 x 10^6 configurations of full equilibration, and 25 x 10^6 configurations of data collection. All degrees of freedom of the inhibitor were sampled except those bonds undergoing perturbation. The perturbed bond lengths were systematically varied from the original to the final length.

***In Vivo* MicroPET/CT Imaging Studies.** Animal studies were approved by the UCLA Animal Research Committee and were carried out according to the guidelines of the Department of Laboratory Animal Medicine at UCLA. For the PET liver assay, C57BL/6 mice were intraperitoneally (i.p.) injected with the indicated amounts of dCK inhibitor (resuspended in 40% Captisol) 4 hours prior to intravenous injection of 70 μCi of ^{18}F-L-FAC. For the tumor xenograft assay, NOD scid IL-2 receptor gamma chain knockout (NSG) bearing subcutaneous CCRF-CEM tumor xenografts were injected with 50 mg/kg of compound **36** or vehicle. Four hours post-treatment mice were injected intravenously with 70 μCi of ^{18}F-L-FAC. For all mPET/CT studies, a 1 h interval was allowed between probe administration and mPET/CT scanning (Inveon, Siemens Medical Solutions USA Inc.; microCAT, Imtek Inc.). Static mPET images were acquired for 600s. Images were analyzed using OsiriX Imaging Software Version 3.8.

Pharmacokinetic Studies. C57Bl/6 female mice, 8 weeks of age, were injected with a single dose of indicated compounds (50 mg/kg, i.p.). Blood samples (approximately 70 μL) were collected through retro-orbital bleeding into heparinized tubes at 5 min, 15 min, 30 min, 35 min, 40 min, 45 min, 1 h, 2 h, 4 h, and 6 h. The blood samples were

centrifuged at 20,000 x g for 5 min to isolate plasma. 1 mL of acetonitrile was added to 30 µL of plasma. The supernatant was transferred to new tubes and was evaporated using a SpeedVac. Samples were then resuspended in 50 µL of neat DMSO and supernatant was transferred to LC/MS sample vials. Samples were then run on an Agilent 6460 Triple Quad LC/MS.

Statistical analyses. All statistics presented as means of biological replicates with standard error of the mean (± SEM), standard deviation (± SD), or box plots with max and min whiskers. P-value significances were calculated using one sample Student's *t* test function in GraphPad Prism 5 (GraphPad Software).

Results

Identification of Lead Compound 15c

To identify new small molecule inhibitors of dCK, we performed a high throughput screen (HTS) of a set of selected chemical libraries totaling ~90,000 small molecules. We screened the library for dCK inhibitory function using a Firefly luciferase-coupled assay with recombinant human dCK enzyme.(Fan and Wood, 2007) In this assay, inhibition of dCK prevents ATP depletion by dCK, thus resulting in higher luminescent signals in positive wells. The screen yielded two hit compounds, **1** and **2**, which were validated to inhibit the uptake of tritiated deoxycytidine (^{3}H-dC) with micromolar potency in the L1210 murine leukemia cell line (Figure 3.1).

Based on these results, five commercially available compounds containing similar structural scaffolds were tested; their IC_{50} values against L1210 cells were determined by measuring inhibition of ^{3}H-dC uptake (Figure 3.1). Strikingly, compounds **6** and **7** were inactive, suggesting that the bis-amino functionality on the pyrimidine ring is crucial for dCK inhibition. Based on these results, we initiated a structure-activity relationship (SAR) study to develop a lead structure, which could be further optimized to compounds with potent *in vivo* activity.

We initially studied two main structural classes of compounds, pyrimidines and 1,3,5-triazines (Table 3.1). Two cell lines were used to determine the IC_{50} values: the L1210 murine leukemia cells and the CCRF-CEM human acute T-lymophoblastic leukemia cells. In nearly all cases, substitution of the pyrimidine ring with the 1,3,5-triazine motif reduced dCK inhibitory activity; in some instances an approximate 2-fold reduction in potency was observed. Consequently, the pyrimidine motif was utilized as

the preferred scaffold to advance. At this stage of the SAR, the presence of a fluoroethoxy side-chain on the phenyl ring was considered for eventual ^{18}F-radiolabeling purposes. Substitutions around the phenyl ring with respect to the position of the fluoroethoxy side-chain were also examined. Moving the fluoroethoxy side-chain from the para position in **8a** to the meta position in **9a** increased the inhibitory activity approximately 2-fold. It was also apparent that alkoxy substituents in the para position were better than alkyl moieties, since compound **11a** had substantially lower activity than either the methoxy **9a** or ethoxy **10a** analogs. Compound **12a**, which contains a side-chain that was extended by one carbon to give a fluoropropoxy group at the meta position, gave slightly greater inhibitory activity, albeit not a significant increase from compounds **9a** and **10a**. Substitution at the ortho position of the phenyl ring, e.g. in compounds **13a** and **14a**, resulted in substantially lower dCK inhibitory activity, an approximate 10-fold decrease in potency was observed for compound **14a** when compared to **9a**.

While the presence of fluorine in the small molecule may eventually enable the synthesis of an ^{18}F-isotopolog of the dCK inhibitor, fluorine introduction also affects nearly all the physical and ADME (adsorption, distribution, metabolism, and excretion) properties of a compound.(Müller et al., 2007) The capacity of fluorine to enhance metabolic stability has become increasingly apparent in recent years.(Park et al., 2001) Thus, a series of compounds were synthesized which contained fluorine attached directly on the aromatic ring of the inhibitors rather than linked by an ethoxy side-chain (compounds **16** - **18**, Table 3.2). For each compound in this series, a set of three derivatives (**a** - **c**) were synthesized; in each case the group on the 5-position of the

thiazole was either a methyl, ethyl or propyl substituent. For compounds **15a** - **c** the fluoroethoxy side-chain was retained at the meta position of the phenyl ring, as was a methoxy group at the para position due to the favorable inhibitory results from the initial SAR in Table 3.1.

Increasing non-polar functionality at the 5-position of the thiazole resulted in increasing inhibitory activity (Table 3.2). The IC_{50} values in CCRF-CEM cells illustrate the same trend in potency as observed in L1210 cells with one exception; set **16** shows little difference between the methyl, ethyl or propyl substituents. However, for all compounds tested against L1210 cells, the propyl substituent yielded better inhibitory activity than the corresponding methyl derivatives. The best example in L1210 cells was the 12-fold increase in activity when comparing compound **15c** to compound **15a**. In addition, comparisons between the propyl substituents against their respective methyl derivatives in CCRF-CEM cells also showed an increasing inhibitory trend in activity: 6-fold (compare **17c** to **17a**) or 3-fold (compare **18c** to **18a**). The most drastic effect from modifications at the 5-position of the thiazole ring was the change exhibited from **9a** in Table 3.1 to **15c** in Table 3.2, where the substitution of a hydrogen for a propyl moiety resulted in a 180-fold increase in potency in L1210 cells. In addition, removal of the fluoroethoxy side-chain (e.g. compound series **16** - **18**) resulted in a significant decrease in potency in both cell lines. Compound **15c**, the most potent compound in this series, contains both the fluoroethoxy side-chain at the meta position on the phenyl ring and also a propyl group at the 5-position of the thiazole ring.

Synthesis

Compounds **15a** - **c** were synthesized in six steps (Scheme 3.1). The commercially available 3-hydroxy-4-methoxybenzonitrile **19** was functionalized via alkylation with 1-bromo-2-fluoroethane in DMF with cesium carbonate as the base to obtain the nitrile **20** in 99% yield. Subjection of **20** to an aqueous ammonium sulfide solution under basic conditions afforded the thioamide **21** in excellent yield (Crane et al., 2004). Cyclization to form the thiazole core of **15a** - **c** was achieved via condensation of thioamide **21** with the respective ethyl 3-bromo-2-oxoalkanoate (Okonya et al., 2002) in refluxing ethanol (Trullinger et al.). Reduction of the resulting compounds with diisobutylaluminum hydride afforded the respective alcohols **23a** - **c** in 88 - 99% yield. The alcohols **23a** - **c** were converted to the respective bromides **24a** - **c** under mild conditions (Joseph and Larraza-Sanchez, 2011) in 74 - 80% yield. Finally, nucleophilic displacement of the bromide with 4,6-diamino-2-mercaptopyrimidine (Laxer et al., 2001) generated the desired products **15a** - **c** in 71 - 87% yield.

X-ray Crystal Structure of Compound 15a Bound to Human dCK

X-ray crystallographic studies of compound **15a** were initiated to obtain information about its binding to dCK. Detailed analysis of the dCK-inhibitor interactions for this series of compounds was performed (Nomme et al., 2014). In short, the crystal structure of the dCK:**15a** complex was solved at 1.9 Å resolution (Figure 3.2). Human dCK, a dimer of two identical subunits with a molecular weight of ~30 kDa per monomer, can bind either ATP or UTP as the phosphoryl donor for catalysis; in addition, dCK can adopt an open or closed conformation (Chottiner et al., 1991; Sabini et al.,

2008; Shewach et al., 1992). In complex with **15a**, the enzyme adopts the open conformation. We observed two **15a** molecules in each protomer of the dimeric enzyme (shown in blue (**15a-I**) and cyan (**15a-II**), Figure 3.2A). Note that binding of **15a** to dCK does not preclude nucleotide binding (UDP is shown in red, Figure 3.2A). The parallel orientation between **15a-I** and **15a-II** allows for optimal π-π stacking interactions between the phenyl and thiazole rings of each molecule.

While two molecules of **15a** bind in the active site, it appears that **15a-I** forms more key interactions and shorter hydrogen bond distances than **15a-II** (Figure 3.2B). The extensive hydrogen-bond network that exists between the pyrimidine moiety of **15a-I** and residues E53, Q97 and D133 in the dCK nucleoside binding site are illustrated in Figure 3.2B. Figure 3.2C illustrates the hydrophobic pocket that exists, via V55, L82 and F96, around the methyl group of compound **15a**. This figure demonstrates that the pocket will accept larger substituents, explaining the increased trend in potency obtained for compounds **15b** and **15c**.

Monte Carlo-based Computational Modeling

A Monte Carlo(Metropolis and Ulam, 1949) (MC)-based computational modeling approach using the free energy perturbation (FEP) method (Jorgensen and Thomas, 2008; Zwanzig, 1954) was used to further investigate the inhibitory effects of alkyl chain lengthening at the 5-position of the thiazole. FEP allows calculation of the difference in binding energy of two molecules. The perturbation of molecule **A** into molecule **B** in a complex with a protein [$\Delta G_{protein}(A \rightarrow B)$] and in solution alone [$\Delta G_{water}(A \rightarrow B)$] is part of

a complete thermodynamic cycle (Figure 3.3A). Because the sum of all components in such a cycle must equal zero, the binding energy difference may be calculated as the difference in free energies:

$$\Delta\Delta G_{binding} = \Delta G_{binding}(B) - \Delta G_{binding}(A) = \Delta G_{protein}(A \rightarrow B) - \Delta G_{water}(A \rightarrow B)$$

Models of structures **15b** and **15c** (Figure 3.3B) each in a monomeric complex with dCK and in solution alone were equilibrated using MC. The equilibrated structure of **15c** was subsequently perturbed into the structure of **15b** ("shrinking" the propyl chain into an ethyl) and vice versa ("growing" the ethyl chain into a propyl) using FEP. These calculations were performed using the MCPRO 2.0 (Jorgensen and Tirado-Rives, 2005) software package. The free energy changes for these perturbations are illustrated in Figure 3.3C. Averaging the $\Delta\Delta G_{binding}$ obtained from the two simulations indicates that the propyl chain of **15c** confers a 1.210 kcal/mol more favorable free energy of binding in comparison to the ethyl chain of **15b**; this favorable effect is due to desolvation. The change in free energy upon extension of the alkyl chain is unfavorable both in the complex with the protein and in water alone (positive ΔG for chain lengthening, negative ΔG for chain shortening); however, the magnitude of the unfavorable ΔG is larger in solvent. The fact that this produces an overall favorable $\Delta\Delta G$ of binding suggests that the propyl chain is better able to exclude water from the interior cavity of the protein, allowing a greater association between the protein and the inhibitor.

Lead Optimization and SAR

Based on the potency trend in Table 3.2 and the existence of a hydrophobic pocket around the 5-position of the thiazole ring of **15a**, all further compounds in the SAR were made with the propyl chain installed at that position, to increase non-polar interactions between the dCK enzyme pocket and the inhibitors. The fluorine atom terminating the ethoxy side-chain was substituted for a hydroxyl or sulfonamide group, with the goal of improving the molecule's solubility properties as well as potential hydrogen bonding interactions that might exist in the active site. Moreover, since inhibitory activity in L1210 and CCRF-CEM cells demonstrated the same trend in potency, the SAR for all subsequently synthesized compounds were examined only in CCRF-CEM cells. The results are summarized in Table 3.3.

Compounds **25** - **27** showed excellent (1 - 2 nM) potency against CCRF-CEM cells (Table 3.3). Substitution of the end-chain hydroxyl for a methyl sulfonamide resulted in a decrease in inhibitory activity of about 3-fold (compare **27** to **29**) or 5-fold (compare **25** to **28**). The initial SAR in Table 3.1 indicated that the presence of an alkoxy substituent at the para position led to increased inhibitory activity; therefore, the methoxy group was reinstalled at the para position. As expected, removal of the ethoxy side-chain (e.g. compound **31**) resulted in a substantially lower inhibitory activity, reinforcing the data observed for compounds **16** - **18** (Table 3.2). The presence of the methoxy moiety at the para position, in addition to the hydroxylethoxy side chain at the meta position, generated compound **33,** which has an inhibitory potency of 1 nM. To our surprise, removal of one of the amino groups from the pyrimidine ring led to a mere 2.5-fold decrease in inhibitory activity (compare **33** to **34**). Initially, we observed that

removal of both amino groups from the pyrimidine ring resulted in complete loss of inhibitory activity (compounds **6** and **7**, Figure 3.1); however, the presence of one amino group can provide suitable key hydrogen bonding interactions to inhibit the enzyme. Compound **32**, which contains a side-chain that has been extended by one carbon to give a hydroxylpropoxy group, was also synthesized. However, this modification resulted in slightly decreased inhibitory activity in comparison with the hydroxylethoxy group. While compound **33** was a potent compound in cell culture, the presence of a primary hydroxyl group in the molecule raised concerns of a metabolic liability as a consequence of potential oxidation or glucuronidation (Shu et al., 2008). Thus, compounds **35** - **37** were synthesized to decrease the possibility of metabolic degradation of **33**. Eight of these compounds in Table 3.3, whose IC_{50} values were lower than **15a** and whose structural properties suggested that they would have the best *in vivo* efficacy, were selected for further investigation.

Steady-state Kinetic Analysis of Selected dCK Inhibitors

In order to confirm that the cell-based values truly reflect the potency of the compounds we also determined the Ki^{app} values for select compounds using steady state kinetic assays. The cell-based assays indicated that compound **15a** was 6 - 12 fold (depending on the cell line used for the assay) less potent than compound **15c** (Table 3.2). Correspondingly, the steady state data showed a 6-fold higher Ki^{app} value for compound **15a** (Table 3.4). Likewise, the low nanomolar IC_{50} observed in CEM cells for compounds **36** and **37** (Table 3.3) was recapitulated in the steady-state kinetics derived Ki^{app} values for these compounds (Table 3.4). Hence, we conclude that our

cell-based assays are providing us with relatively accurate data as to the strength of the interactions between the compounds and dCK.

Evaluation of *In Vivo* Inhibition of dCK Activity Via a New PET PD Assay

The nucleoside analog PET probe ^{18}F-L-FAC is a high affinity substrate for dCK, which can be used to non-invasively estimate dCK enzymatic activity *in vivo* (Shu et al., 2010). A schematic depicting the mechanism by which ^{18}F-L-FAC accumulates in cells in a dCK-specific manner is shown in Figure 3.4A. We reasoned that ^{18}F-L-FAC PET could be used to rapidly identify the most potent dCK inhibitors based on their effectiveness at inhibiting the accumulation of the ^{18}F-labeled dCK substrate PET tracer in various tissues. For the *in vivo* PET PD assay we selected dCK inhibitors that demonstrated 1 – 12 nM inhibitory activity in the cell culture ^{3}H-dC uptake assay (Table 3.3). Mice were treated with a single dose (50 mg/Kg) of a given dCK inhibitor administered by intraperitoneal injection. Control mice received vehicle (40% Captisol in water) injections. Four hours later, treated mice were injected intravenously with ^{18}F-L-FAC; one hour after probe injection, mice were imaged by mPET/CT. The readout for the PET PD assay was the reduction in the accumulation of ^{18}F-L-FAC in dCK-positive tissues in dCK inhibitor versus vehicle treated mice. Previously, we showed that ^{18}F-L-FAC accumulates in a dCK-dependent manner into various tissues such as the thymus, spleen, bone marrow and liver (Shu et al., 2010). Accumulation in the bladder is a result of non-enzymatic renal clearance of the unmetabolized probe. Since the reproducibility in the dCK-dependent tissue retention of ^{18}F-L-FAC was most consistent in the liver (Shu et al., 2010), we chose to quantify ^{18}F-L-FAC liver retention in order to

compare the *in vivo* efficacy of the various dCK inhibitors. Optimal conditions for the PET PD assay were determined by performing a dose escalation and time course study using compound **33**.

Results from the ^{18}F-L-FAC mPET/CT scans are summarized in Figure 3.4. Transverse PET images of the ^{18}F-L-FAC liver scans for mice treated with either vehicle or compounds **15a**, **36** or **37** are shown in Figure 3.4B. Figure 3.4C illustrates the uptake of ^{18}F-L-FAC in the livers of mice treated dCK inhibitors. The more efficacious compounds induced a greater reduction in the ^{18}F-L-FAC uptake relative to vehicle treatment, as a result of their greater inhibition of dCK-mediated phosphorylation of its ^{18}F-labeled substrate. Note the approximate 30% decrease in ^{18}F-L-FAC signal compared to vehicle control induced by compounds **28**, **29**, **36** and **37**, indicating their superior *in vivo* efficacy relative to the other dCK inhibitor candidates. In addition, compounds **30** and **32** show about a 20% decrease in probe uptake. Compound **33**, one of the most potent dCK inhibitors in the cell culture assay (Table 3.3) showed poor *in vivo* efficacy in the ^{18}F-L-FAC liver PET assay, presumably due to its poor PK properties. As hypothesized, substitution of the hydroxyl group at the end of the ethoxy chain (e.g. compound **33**) for the metabolically stable methylsulfonamide (compounds **28**, **29** and **37**) or hindering the hydroxyl group (compound **36**) proved advantageous for *in vivo* efficacy. Compounds **36** and **37** have the lowest IC_{50} values amongst all the efficacious compounds and were chosen for further study. Here we focus on compound **36** while compound **37** is described in Nathanson et *al*.

Next we determined the efficacy of compound **36** at inhibiting dCK activity in tumor tissues *in vivo*. Mice bearing CCRF-CEM tumor xenografts were treated with

compound **36** four hours prior to injection of ^{18}F-L-FAC (Figure 3.4D). One hour after the ^{18}F-L-FAC injection, mice were imaged by mPET/CT. The retention of ^{18}F-L-FAC in tumor xenografts from mice treated with compound **36** was reduced by about 30% compared to the retention of ^{18}F-L-FAC in tumors from vehicle treated mice (Figure 3.4D). To complement the PET assay, the pharmacokinetics of compound **36** was determined using standard analytical techniques and the approximated values are reported in Figure 3.5.

X-ray Crystal Structure of Compound 36 Bound to Human dCK

X-ray crystallographic studies of compound **36** were initiated to obtain information about its binding to dCK. The crystal structure of the dCK:**36** complex was solved at 1.94 Å resolution (Figure 3.6 and Table 3.5). Similar to our observations for compound **15a** (Figure 3.2), in the case of **36**, the enzyme also adopts the open conformation. We observed one **36** molecule (green) in each protomer of the dimeric enzyme (Figure 3.6A). This is contrast to the observation of two molecules bound per active site when the substituent at the 5-position is smaller than the propyl present in **36** (Figure 3.2, determinants of single versus double molecule binding to the dCK active site was analyzed in Nomme et *al*.). Note that binding of **36** to dCK does not preclude nucleotide binding (UDP is shown in red, Figure 3.6A). The specific dCK:**36** interactions are shown in Figure 3.6B. These include an extensive hydrogen-bond network between the pyrimidine moiety of **36** and residues E53, Q97 and D133 in the dCK nucleoside binding site, as well as several hydrophobic interactions.

Discussion

The identification of potent small molecule human dCK inhibitors that demonstrate *in vivo* target inhibition is reported. Optimization of inhibitory activity was achieved by extending an alkyl chain from the 5-position of the thiazole ring. *In vivo* efficacy was improved by manipulation of the ethoxy side-chain present at the meta position of the phenyl ring. The utility of PET as a powerful tool for non-invasive measure of target inhibition and, consequently, as a measure of *lack* of target inhibition (most likely due to substrate metabolism *in vivo*), is also presented. Although the major clinical applications of PET are primarily for central nervous system (CNS) and oncology-based diagnostics/therapeutics, PET is playing an increasingly important role in drug development, given the capability of this molecular imaging platform to address key challenges that include evaluation of biodistribution, absorption, target affinity, plasma binding, metabolism, and dosing (Bhattacharyya, 2012). Here we used the radiotracer ^{18}F-L-FAC as a PET PD biomarker to compare the *in vivo* efficacies of candidate dCK inhibitors, first identified and characterized by potency in cell culture assays. Moreover, we used PET to provide estimates of *in vivo* target inhibition in CCRF-CEM xenograft mouse models by one of our most promising compounds, **36**. The ability of another promising compound, **37**, to elicit a significant pharmacological response against CCRF-CEM tumors with minimal toxicity to normal tissues was evaluated by our group and is described in a separate publication. Further optimization offering improvements to the PK and solubility properties of our best dCK inhibitors will be addressed in subsequent studies. In addition, the presence of fluorine on the aromatic ring of one of our most promising dCK inhibitors, **29**, makes it amenable to ^{18}F

radiolabeling. Synthesizing a small molecule dCK inhibitor with an ^{18}F radioisotope could generate a positron-emitting version of the therapeutic candidate that can be detected and quantified non-invasively throughout the body of living individuals by PET imaging. This work will be the subject of a future communication.

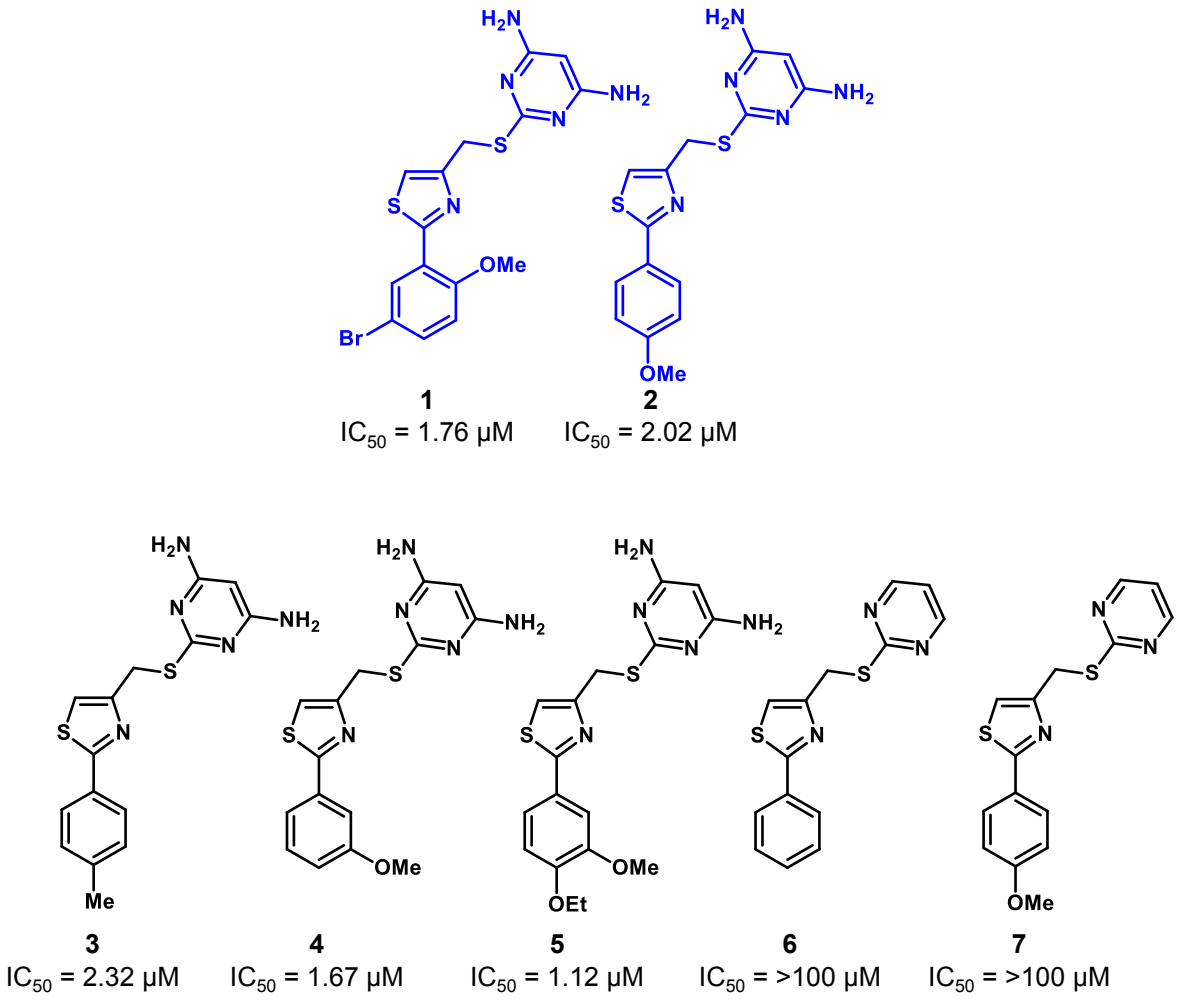

Figure 3.1. Structures and IC_{50} values determined using the ^{3}H-deoxycytidine (^{3}H-dC) uptake assay in L1210 cells for the initial HTS hits (**1** and **2**) and for commercially available compounds containing similar structural scaffolds (**3** - **7**).

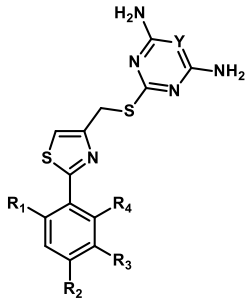

Compound	R_1	R_2	R_3	R_4	IC_{50} (μM) L1210 cells		IC_{50} (μM) CEM cells	
					a Y = CH	**b** Y = N	**a** Y = CH	**b** Y = N
8	H	OCH_2CH_2F	OCH_3	H	0.808 (± 0.406)	1.612 (± 0.543)	0.421 (± 0.075)	0.534 (± 0.012)
9	H	OCH_3	OCH_2CH_2F	H	0.538 (± 0.014)	0.528 (± 0.015)	0.230 (± 0.042)	0.506 (± 0.138)
10	H	OCH_2CH_3	OCH_2CH_2F	H	0.513 (± 0.100)	1.226 (± 0.450)	0.251 (± 0.020)	0.512 (± 0.409)
11	H	CH_3	OCH_2CH_2F	H	2.381 (± 0.042)	3.201 (± 0.566)	1.960 (± 1.001)	1.922 (± 0.573)
12	H	OCH_3	$OCH_2CH_2CH_2F$	H	0.330 (± 0.160)	0.603 (± 0.140)	0.197 (± 0.109)	0.297 (± 0.020)
13	OCH_3	H	OCH_2CH_2F	H	1.445 (± 0.060)	2.649 (± 0.902)	1.041 (± 0.084)	0.849 (± 0.183)
14	H	OCH_2CH_2F	H	OCH_3	5.469 (± 1.336)	ND[b]	2.367 (± 0.238)	ND[b]

Table 3.1. ***In vitro*** **biological data in L1210 and CEM cells for compounds 8 - 14.**

Inhibitory activity measured by ^{3}H-dC uptake in murine L1210 cells and in CCRF-CEM human cells. Values reported are the mean ± SD of at least n = 2 independent experiments. [b]ND = not determined (compound was not synthesized).

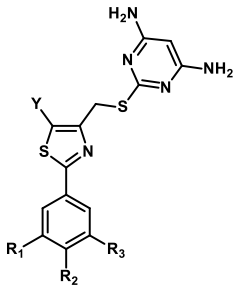

Compound	R_1	R_2	R_3	IC_{50} (μM) L1210 cells			IC_{50} (μM) CEM cells		
				a Y = Me	**b** Y = Et	**c** Y = Pr	**a** Y = Me	**b** Y = Et	**c** Y = Pr
15	H	OCH_3	OCH_2CH_2F	0.035 (± 0.015)	0.030 (± 0.077)	0.003 (± 0.000)	0.018 (± 0.012)	0.007 (± 0.002)	0.003 (± 0.000)
16	F	H	F	0.595 (± 0.163)	0.620 (± 0.170)	0.385 (± 0.262)	0.150 (± 0.099)	0.162 (± 0.019)	0.173 (± 0.157)
17	H	F	H	0.395 (± 0.134)	0.265 (± 0.163)	0.170 (± 0.099)	0.230 (± 0.134)	0.083 (± 0.043)	0.037 (± 0.020)
18	H	H	F	0.255 (± 0.021)	0.510 (± 0.014)	0.175 (± 0.007)	0.092 (± 0.048)	0.011 (± 0.038)	0.031 (± 0.024)

Table 3.2. ***In vitro*** **biological data in L1210 and CEM cells for compounds 15 – 18** Inhibitory activity measured by ^{3}H-dC uptake in murine L1210 and in CCRF-CEM human cells. Values reported are the mean ± SD of at least n = 2 independent experiments.

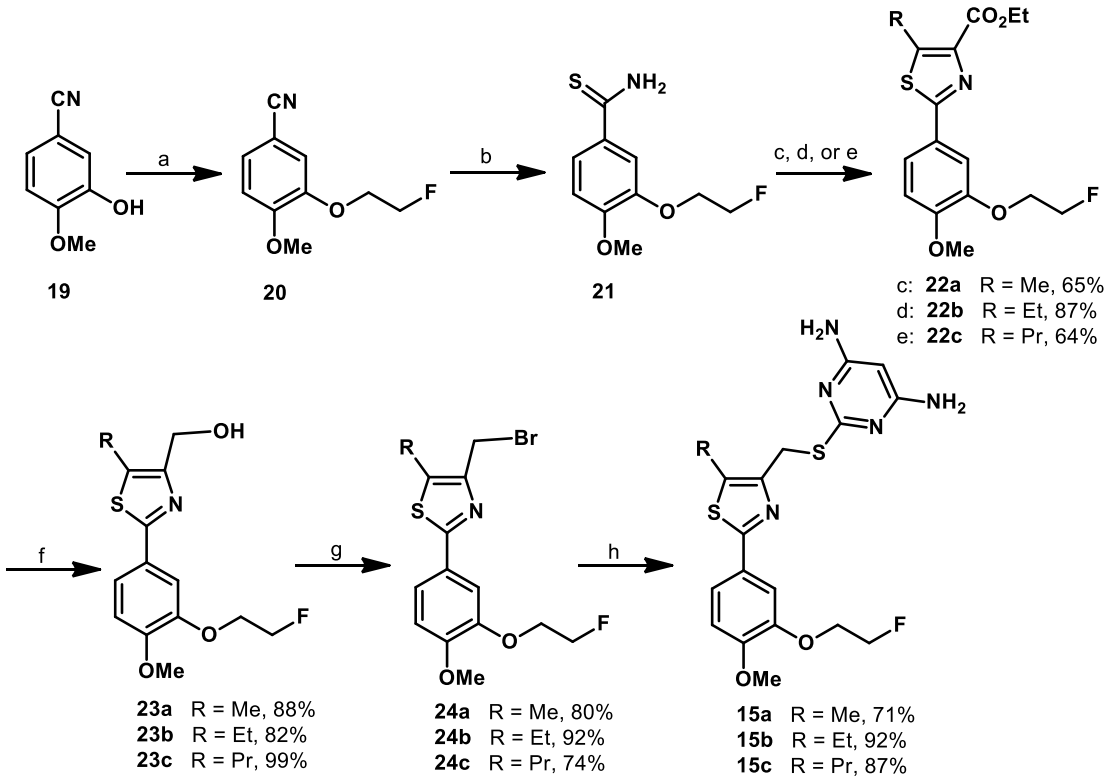

Scheme 3.1. Synthesis of compounds 15a – c

Reagents and conditions: (a) 1-bromo-2-fluoroethane, Cs_2CO_3, DMF, 99%; (b) $(NH_4)_2S$ (20% in H_2O), pyridine, Et_3N, quantitative; (c) ethyl 3-bromo-2-oxobutanoate, EtOH; (d) ethyl 3-bromo-2-oxopentanoate, EtOH; (e) ethyl 3-bromo-2-oxohexanoate, EtOH; (f) DIBAL-H, CH_2Cl_2; (g) 1,1,1,3,3,3-hexabromoacetone, PPh_3, CH_3CN; (h) 4,6-diamino-2-mercaptopyrimidine, NaOH, EtOH.

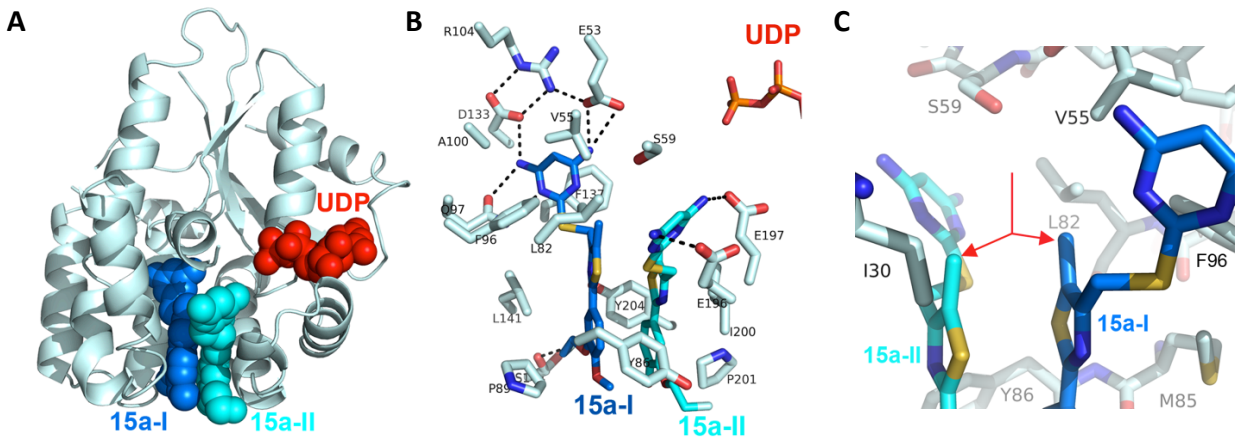

Figure 3.2. Binding of 15a to human dCK. (A) Ribbon diagram of a dCK monomer (light blue) with the two observed molecules of **15a** bound (blue and cyan spheres, respectively) at the active site. The nucleotide UDP (red) was also present in the complex. (B) The interactions between **15a** and dCK. Polar interactions are indicated as broken black lines. The two phosphate groups of UDP (top right) demonstrate the relative orientation of **15a-I** (blue) and **15a-II** (cyan) to the nucleotide. (C) The methyl group of the **15a-I** and **15a-II** thiazole ring (red arrows) stack against each other, occupying a hydrophobic pocket.

A

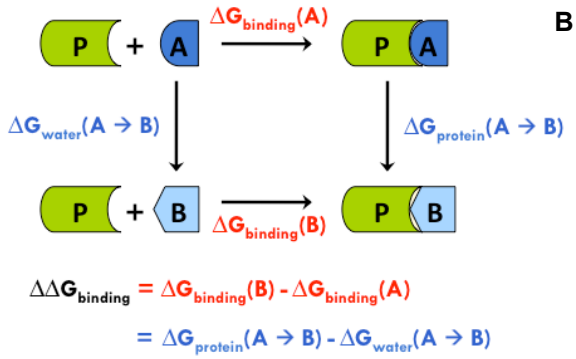

B

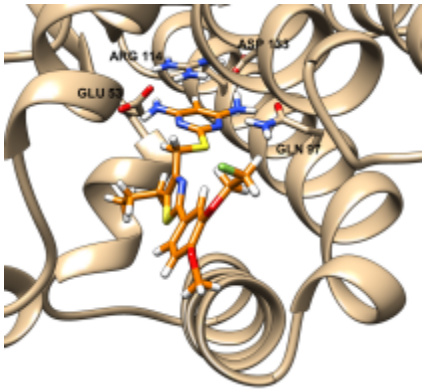

C

	$\Delta G_{protein}$	ΔG_{water}	$\Delta\Delta G_{binding}$
15b to **15c**	1.964 ± 0.050	2.802 ± 0.046	-0.838 ± 0.068
15c to **15b**	-1.251 ± 0.029	-2.832 ± 0.046	1.581 ± 0.054
Average			1.210 in favor of **15c**

Figure 3.3. (A) The complete thermodynamic cycle relating the binding energies to the perturbation of molecule A into molecule B. ΔGprotein(A → B) denotes the change in free energy upon perturbation of A into B in the solvated inhibitor-protein complex, while ΔGwater(A → B) denotes the free energy change when the perturbation takes place in water alone. The difference in free energies of binding, ΔΔGbinding, is equal to the change in free energy when molecule A binds with the protein [ΔGbinding(A)] subtracted from the change in free energy when molecule B binds [ΔGbinding(B)]. Because the sum of all components in a complete thermodynamic cycle must equal zero, ΔΔGbinding is therefore also equivalent to ΔGprotein(A → B) - ΔGwater(A → B). (B) Computational model of compound 15c (orange) in complex with dCK. Binding pocket residues Glu 53, Gln 97, Arg 114, and Asp 133 are shown explicitly, while the remainder of the protein is illustrated as a ribbon structure. (C) Free energy changes (kcal/mol) associated with the perturbation of the alkyl chain at the 5-position of the

thiazole. ΔGprotein is the change in free energy for the solvated inhibitor-protein complex. ΔGwater is the free energy change for the inhibitor in water alone. The change in free energy upon binding is denoted as ΔΔGbinding.

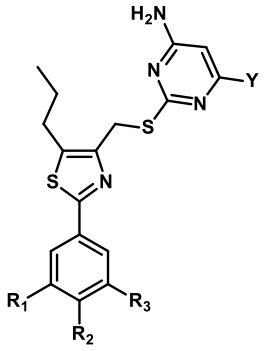

Compound	R_1	R_2	R_3	Y	IC_{50} (nM) CEM cells
25	H	H	OCH_2CH_2OH	NH_2	2.45 (± 0.778)
26	H	F	OCH_2CH_2OH	NH_2	1.07 (± 0.230)
27	F	H	OCH_2CH_2OH	NH_2	2.83 (± 1.628)
28	H	H	$OCH_2CH_2NHSO_2CH_3$	NH_2	11.58 (± 3.353)
29	F	H	$OCH_2CH_2NHSO_2CH_3$	NH_2	8.01 (± 0.230)
30	H	OCH_2CH_2OH	OCH_2CH_2OH	NH_2	2.59 (± 1.146)
31	H	OCH_3	OH	NH_2	18.62[b]
32	H	OCH_3	$OCH_2CH_2CH_2OH$	NH_2	1.55 (± 0.354)
33	H	OCH_3	OCH_2CH_2OH	NH_2	1.15 (± 0.762)
34	H	OCH_3	OCH_2CH_2OH	H	2.90 (± 0.300)
35	H	OCH_3	$OCH_2CH(CH_3)OH$	NH_2	2.85 (± 0.071)
36	H	OCH_3	$OCH_2C(CH_3)_2OH$	NH_2	1.44 (± 0.538)
37	H	OCH_3	$OCH_2CH_2NHSO_2CH_3$	NH_2	4.89 (± 2.014)

Table 3.3. *In vitro* biological data in CEM cells for compounds **25**- **37.** Inhibitory activity measured by ^{3}H-deoxycytidine (^{3}H-dC) uptake in CCRF-CEM human cells. Values reported are the mean ± SD of at least n = 2 independent experiments. [b]Value reported for n = 1.

Compound	Ki ^{app} (nM)	Error (nM)	R^2
15a*	9.5	2.3	0.974
15c*	1.5	0.3	0.998
36	0.8	0.7	0.982
37	0.5	0.5	0.988

* Data from Nomme *et al.*

Table 3.4. Steady state kinetics of selected dCK inhibitors

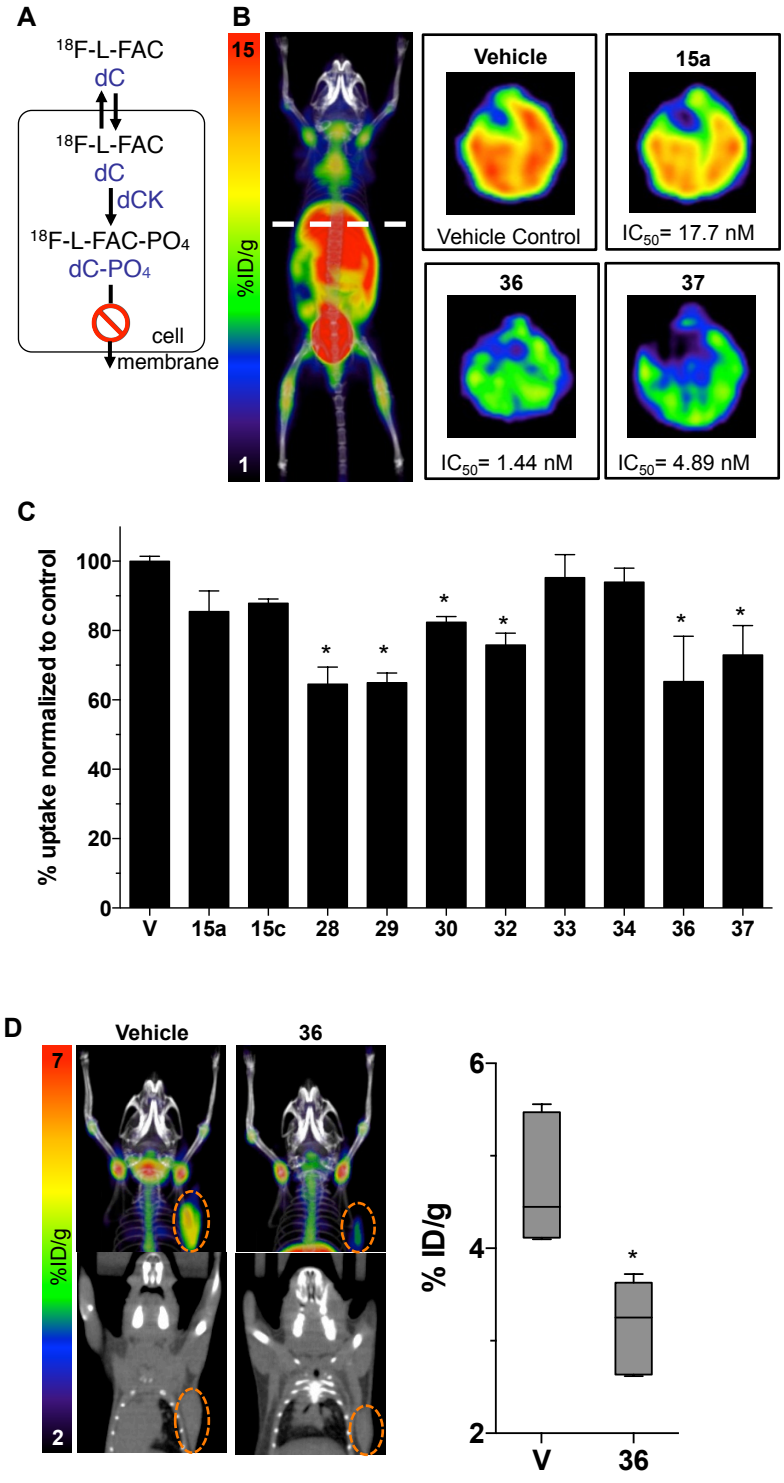

Figure 3.4. ***In vivo*** **evaluation of dCK inhibitors via PET analysis.** (A) Schematic of the mechanism by which ^{18}F-L-FAC accumulates in dCK expressing cells. (B)

Representative transverse images of ^{18}F-L-FAC PET/CT liver scans of C57Bl/6 mice treated with compounds **15a**, **36**, and **37**. (C) Quantification of ^{18}F-L-FAC uptake in the liver for a sample of inhibitors with low nanomolar *in vitro* potency. Data are mean values ± SEM for at least n = 3 mice/group. *, $P < 0.03$. (D) Representative images and quantification of ^{18}F-L-FAC PET/CT scans of CCRF-CEM tumor bearing NSG mice that were treated with vehicle, or compound **36**. Data are displayed as box and whisker plots for at least n = 4 mice/group. *, $P < 0.0012$.

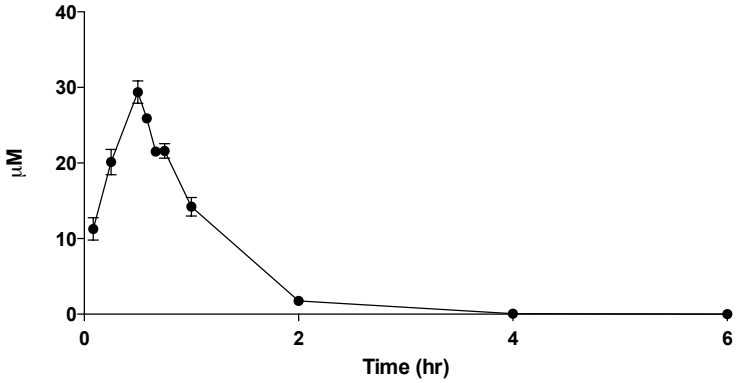

	Dose (mg/kg)	$AUC_{(0-t)}$ (mg/ml x min)	$T_{1/2}$ (min)	T_{max} (min)	C_{max} (μM)
36	50	.832	30	30	30

Figure 3.5. **Pharmacokinetic profile of compound 36.** C57Bl/6 female mice were dosed with compound **36** via intraperitoneal injection. Dose formulation: 10% DMSO and 40% Captisol in water. Data are mean values ± SEM for n = 4 mice/time point.

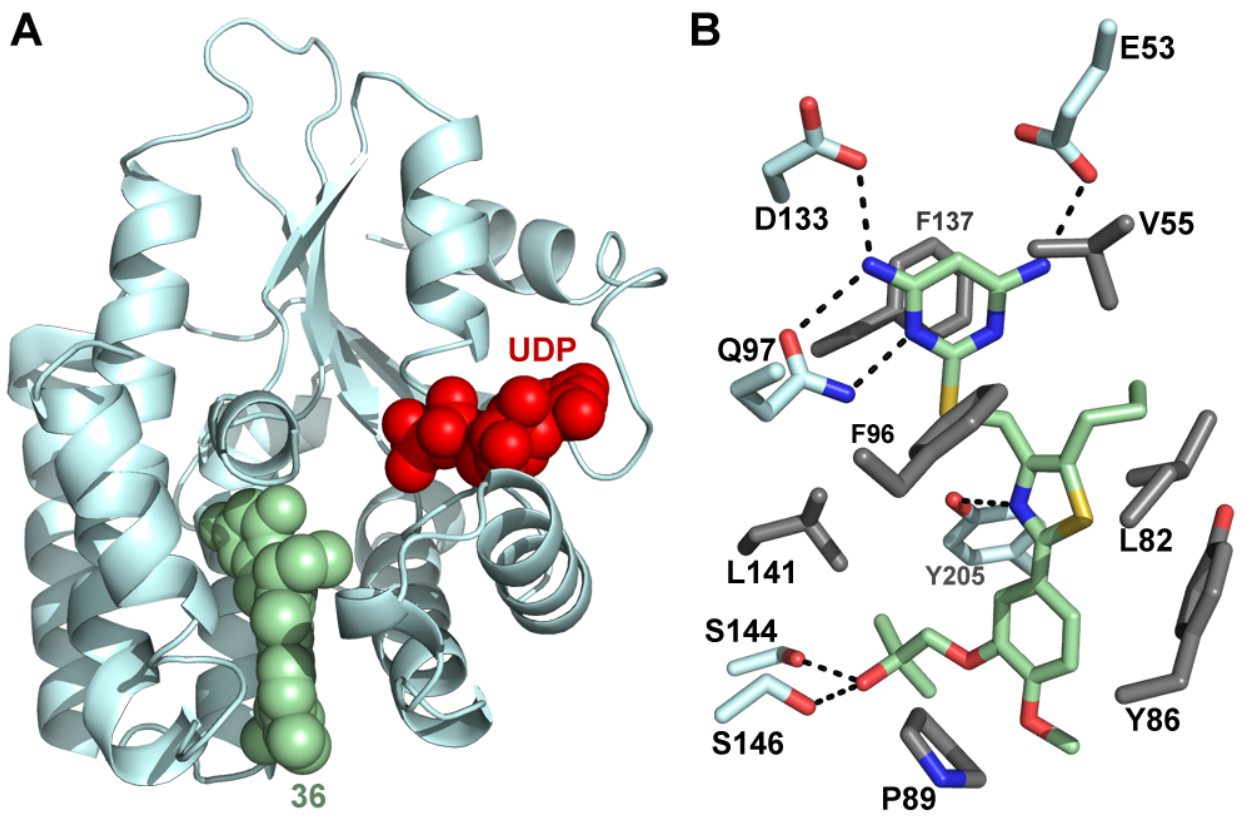

Figure 3.6. Crystal structure of dCK:36 complex. (A) Ribbon diagram of a dCK monomer (light blue) with the single observed molecule of **36** bound (green spheres) at the active site. The nucleotide UDP (red spheres) was also present in the complex. (B) Detail of the interactions between **36** and dCK. dCK residues involved in polar and hydrophobic interactions with **36** are colored in light blue and gray, respectively. Polar interactions are indicated as broken black lines.

References

Arner, E.S.J., and S. Eriksson. 1995. Mammalian Deoxyribonucleoside Kinases. *Pharmac. Ther.* 67:155-186.

Austin, W.R., A.L. Armijo, D.O. Campbell, A.S. Singh, T. Hsieh, D. Nathanson, H.R. Herschman, M.E. Phelps, O.N. Witte, J. Czernin, and C.G. Radu. 2012. Nucleoside Salvage Pathway Kinases Regulate Hematopoiesis by Linking Nucleotide Metabolism with Replication Stress. *J. Exp. Med.* 209:2215-2228.

Bhattacharyya, S. 2012. Application of Positron Emission Tomography in Drug Development. *Biochem. Pharmacol.* 1:1000e1128.

Chottiner, E.G., D.S. Shewach, N.S. Datta, E. Ashcraft, D. Gribbin, D. Ginsburg, I.H. Fox, and B.S. Mitchell. 1991. Cloning and Expression of Human Deoxycytidine Kinase cDNA. *Proc. Natl. Acad. Sci. U.S.A.* 88:1531-1535.

Crane, L.J., M. Anastassiadou, J.-L. Stigliani, G. Baziard-Mouysset, and M. Payard. 2004. Reactions of Some Ortho and Para Halogenated Aromatic Nitriles with Ethylenediamine: Selective Synthesis of Imidazolines. *Tetrahedron* 60:5325-5330.

Czernin, J., M.R. Benz, and M.S. Allen-Auerbach. 2010. PET/CT Imaging: The Incremental Value of Assessing the Glucose Metabolic Phenotype and the Structure of Cancers in a Single Examination. *Eur. J. Radiol.* 73:470-480.

Fan, F., and K.V. Wood. 2007. Bioluminescent assays for high-throughput screening. *Assay Drug Dev Technol* 5:127-136.

Gambhir, S.S. 2002. Molecular Imaging of Cancer with Positron Emission Tomography. *Nat. Rev. Cancer* 2:683-693.

Hargreaves, R.J. 2008. The Role of Molecular Imaging in Drug Discovery and Development. *Clin. Pharmacol. Ther.* 83:349-353.

Jadvar, H., A. Alavi, and S.S. Gambhir. 2009. ^{18}F-FDG Uptake in Lung, Breast, and Colon Cancers: Molecular Biology Correlates and Disease Characterization. *J. Nucl. Med.* 50:1820-1827.

Jessop, T.C., J.E. Tarver, M. Carlsen, A. Xu, J.P. Healy, A. Heim-Riether, Q. Fu, J.A. Taylor, D.J. Augeri, M. Shen, T.R. Stouch, R.V. Swanson, L.W. Tari, M. Hunger, I. Hoffman, P.E. Keyes, X.-C. Yu, M. Miranda, Q. Liu, J.C. Swaffield, S.D. Kimball, A. Nouraldeen, A.G.E. Wilson, A.M.D. Foushee, K. Jhaver, R. Finch, S.

Anderson, T. Oravecz, and K.G. Carson. 2009. Lead Optimization and Structure-based Design of Potent and Bioavailable Deoxycytidine Kinase Inhibitors. *Bioorg. Med. Chem. Lett.* 19:6784-6787.

Jorgensen, W.L., J. Chandrasekhar, J.D. Madura, R.W. Impey, and M.L. Klein. 1983. Comparison of Simple Potential Functions for Simulating Liquid Water. *J. Chem. Phys.* 79:926-935.

Jorgensen, W.L., D.S. Maxwell, and J. Tirado-Rives. 1996. Development and Testing of the OPLS All-Atom Force Field on Conformational Energetics and Properties of Organic Liquids. . *J. Am. Chem. Soc.* 118:11225-11236.

Jorgensen, W.L., and L.L. Thomas. 2008. Perspective on Free-Energy Perturbation Calculations for Chemical Equilibria. *J. Chem. Theory Comput* 4:869-876.

Jorgensen, W.L., and J. Tirado-Rives. 2005. Molecular Modeling of Organic and Biomolecular Systems Using BOSS and MCPRO. *J. Comput. Chem.* 26:1689-1700.

Joseph, K.M., and I. Larraza-Sanchez. 2011. Synthesis of Benzyl Bromides with Hexabromoacetone: an Alternative Path to Drug Intermediates. *Tetrahedron Lett.* 52:13-16.

Krishnan, P., E.A. Gullen, W. Lam, G.E. Dutschman, S.P. Grill, and Y.C. Cheng. 2003. Novel Role of 3-Phosphoglycerate Kinase, a Glycolytic Enzyme, in the Activation of L-Nucleoside Analogs, a new class of Anticancer and Antiviral Agents. *J. Biol. Chem.* 278:36726-36732.

Laing, R.E., M.A. Walter, D.O. Campbell, H.R. Herschman, N. Satyamurthy, M.E. Phelps, J. Czernin, O.N. Witte, and C.R. Radu. 2009. Noninvasive Prediction of Tumor Responses to Gemcitabine using Positron Emission Tomography. *Proc. Natl. Acad. Sci. U.S.A.* 106:2847-2852.

Laxer, A., D.T. Major, H.E. Gottlieb, and B. Fischer. 2001. ($^{15}N_5$)-Labeled Adenine Derivatives: Synthesis and Studies of Tautomerism by ^{15}N NMR Spectroscopy and Theoretical Calculations. *J. Org. Chem.* 66:5463-5481.

Metropolis, N., and S. Ulam. 1949. The Monte Carlo Method. *J. Am. Statistical Assn.* 44:335-341.

Müller, K., C. Faeh, and F. Diederich. 2007. Fluorine in Pharmaceuticals: Looking Beyond Intuition. *Science* 317:1881-1886.

Nomme, J., J.M. Murphy, Y. Su, N.D. Sansone, A.L. Armijo, S.T. Olson, C. Radu, and A. Lavie. 2014. Structural characterization of new deoxycytidine kinase inhibitors rationalizes the affinity-determining moieties of the molecules. *Acta crystallographica. Section D, Biological crystallography* 70:68-78.

Okonya, J.F., R.V. Hoffman, and M.C. Johnson. 2002. Synthesis of 2-Oxazolone-4-Carboxylates from 3-Nosyloxy- and 3-Bromo-2-ketoesters. *J. Org. Chem.* 67:1102-1108.

Oriuchi, N., T. Higuchi, T. Ishikita, M. Miyakubo, H. Hanaoka, Y. Iida, and K. Endo. 2006. Present Role and Future Prospects of Positron Emission Tomography in Clinical Oncology. *Cancer Sci.* 97:1291-1297.

Park, B.K., N.R. Kitteringham, and P.M. O'Neill. 2001. Metabolsim of Fluorine-containing Drugs. *Annu. Rev. Pharmacol. Toxicol.* 41:443-470.

Pasti, C., S. Gallois-Montbrun, H. Munier-Lehmann, M. Vernon, A.M. Gilles, and D. Deville-Bonne. 2003. Reaction of Human UMP-CMP Kinase with Natural and Analog Substrates. *Eur. J. Biochem.* 270:1784-1790.

Radu, C.G., C.J. Shu, E. Nair-Gill, S.M. Shelly, J.R. Barrio, N. Satyamurthy, M.E. Phelps, and O.N. Witte. 2008. Molecular Imaging of Lymphoid Organs and Immune Activation by Positron Emission Tomography with a new [^{18}F]-labeled 2'-deoxycytidine Analog. *Nat. Med.* 14:783-788.

Reichard, P. 1988. Interactions between deoxyribonucleotide and DNA synthesis. *Annu. Rev. Biochem.* 57:349-374.

Rigo, P., P. Paulus, B.J. Kaschten, R. Hustinx, T. Bury, G. Jerusalem, T. Benoit, and J. Foidart Willems. 1996. Oncological Application of Positron Emission Tomography with Fluorine-18. *Eur. J. Nucl. Med.* 23:1641-1674.

Sabini, E., S. Hazra, S. Ort, M. Konrad, and A. Lavie. 2008. Structural Basis for Substrate Promiscuity of dCK. *J. Mol. Biol.* 378:607-621.

Shewach, D.S., K.K. Reynolds, and L. Hertel. 1992. Nucleotide Specificity of Human Deoxycytidine Kinase. *Mol. Pharmacol.* 42:518-524.

Shu, C.J., D.O. Campbell, J.T. Lee, A.Q. Tran, J.C. Wengrod, O.N. Witte, M.E. Phelps, N. Satyamurthy, J. Czernin, and C.R. Radu. 2010. Novel PET Probes Specific for Deoxycytidine Kinase. *J. Nucl. Med.* 51:1092-1098.

Shu, Y.Z., B.M. Johnson, and T.J. Yang. 2008. Role of biotransformation studies in minimizing metabolism-related liabilities in drug discovery. *AAPS* 10:178-192.

Tarver, J.E., T.C. Jessop, M. Carlsen, D.J. Augeri, Q. Fu, J.P. Healy, A. Heim-Riether, A. Xu, J.A. Taylor, M. Shen, P.E. Keyes, S.D. Kimball, X.-C. Yu, M. Miranda, Q. Liu, J.C. Swaffield, A. Nouraldeen, A.G.E. Wilson, R. Rinch, K. Jhaver, A.M.D. Foushee, S. Anderson, T. Oravecz, and K.G. Carson. 2009. 5-Fluorocytosine Derivatives as Inhibitors of Deoxycytidine Kinase. *Bioorg. Med. Chem. Lett.* 19:6780-6783.

Toy, G., W.R. Austin, H.-I. Liao, D. Cheng, A. Singh, D.O. Campbell, T.-o. Ishikawa, L.W. Lehmann, N. Satyamurthy, M.E. Phelps, H.R. Herschman, J. Czernin, O.N. Witte, and C.G. Radu. 2010. Requirement for Deoxycytidine Kinase in T and B Lymphocyte Development. *Proc. Natl. Acad. Sci. U.S.A.* 107:5551-5556.

Trullinger, T.K., R. Hunter, N. Garizi, M.C.H. Yap, A.M. Buysse, D. Pernich, T.C. Johnson, K. Bryan, C. Deamicis, Y. Zhang, N.M. Niyaz, C.L. McLeod, R. Ross, Y. Zhu, P.L. Johnson, J.D. Eckelbarger, and M.H. Parker. Pesticidal Compositions. Patent application US 2010/0292253 A1.

Van Rompay, A.R., M. Johansson, and A. Karlsson. 2003. Substrate Specificity and Phosphorylation of Antiviral and Anticancer Nucleoside Analogs by Human Deoxyribonucleoside Kinases and Ribonucleoside Kinases. *Pharmacol. Ther.* 100:119-139.

Wagner, C.C., M. Muller, G. Lappin, and O. Langer. 2008. Positron Emission Tomography for Use in Microdosing Studies. *Curr. Opin. Drug Discov. Devel.* 11:104-110.

Wang, J.L., and L. Maurer. 2005. Positron Emission Tomography: Applications in Drug Discovery and Drug Development. *Curr. Top. Med. Chem.* 5:1053-1075.

Ward, A.D., and B.R. Baker. 1977. Irreversible Enzyme Inhibitors: Active-Site-Directed Inhibitors of Deoxycytidine Kinase. *J. Med. Chem.* 20:88-92.

Weber, W.A. 2006. Positron Emission Tomography as an Imaging Biomarker. *J. Clin. Oncol.* 24:3282-3292.

Weber, W.A., A.L. Grosu, and J. Czernin. 2008. Technology Insight: Advances in Molecular Imaging and an Appraisal of PET/CT Scanning. *Nat. Clin. Prac. Oncol.* 5:160-170.

Wood, K.A., P.J. Hoskin, and M.I. Saunders. 2007. Positron Emission Tomography in Oncology: A Review. *Clin. Oncol.* 19:237-255.

Yang, C., M. Lee, J. Hao, X. Cui, X. Guo, C. Smal, F. Bontemps, S. Ma, X. Liu, D. Engler, W.B. Parker, and B. Xu. 2012. Deoxycytidine kinase regulates the G2/M checkpoint through interaction with cyclin-dependent kinase 1 in response to DNA damage. *Nucleic Acids Res* 40:9621-9632.

Yu, X.-C., M. Miranda, Z. Liu, S. Patel, N. Nguyen, K. Carson, Q. Liu, and J.C. Swaffield. 2010. Novel Potent Inhibitors of Deoxycytidine Kinase Identified and Compared by Multiple Assays. *J. Biomol. Screening* 15:72-79.

Zwanzig, R.W. 1954. High-Temperature Equation of State by a Perturbation Method. *J. Chem. Phys.* 22:1420-1426.

CHAPTER 4

Co-targeting of Convergent Nucleotide Biosynthetic Pathways for Leukemia Eradication

Abstract

Pharmacological targeting of metabolic processes in cancer must overcome redundancy in biosynthetic pathways. Deoxycytidine triphosphate (dCTP) can be produced both by the *de novo* pathway (DNP) and by the nucleoside salvage pathway (NSP). However, the role of the NSP in dCTP production and DNA synthesis in cancer cells is currently not well understood. Here we show that acute lymphoblastic leukemia (ALL) cells avoid lethal replication stress following thymidine-induced inhibition of DNP dCTP synthesis by switching to NSP-mediated dCTP production. The metabolic switch in dCTP production triggered by DNP inhibition is accompanied by NSP upregulation and can be prevented using DI-39, a new high-affinity small-molecule inhibitor of the NSP rate-limiting enzyme deoxycytidine kinase (dCK). Positron emission tomography (PET) imaging was useful for following both the duration and degree of dCK inhibition by DI-39 treatment in vivo, thus providing a companion pharmacodynamic biomarker. Pharmacological co-targeting of the DNP with thymidine and the NSP with DI-39 was efficacious against ALL models in mice, without detectable host toxicity. These findings advance our understanding of nucleotide metabolism in leukemic cells, and identify dCTP biosynthesis as a potential new therapeutic target for metabolic interventions in ALL and possibly other hematological malignancies.

Introduction

The ability to reprogram cellular metabolism, a hallmark of cancer first noted long ago (Warburg et al., 1927) and recently re-appreciated, is essential for tumor progression (Hanahan and Weinberg, 2011). While cancer-initiated metabolic reprogramming processes are promising therapeutic targets (Vander Heiden, 2011), the existence of alternative, compensatory biosynthetic pathways presents a significant challenge for developing such therapies. For example, in lipid metabolism, cancer cells scavenge extracellular lipids as an alternative to energy-requiring *de novo* fatty acid biosynthesis (Kamphorst et al., 2011). In amino acid metabolism, glycine and serine required for tumor growth can be produced *de novo* and can also be scavenged from the extracellular environment (Jain et al., 2012; Maddocks et al., 2012).

Nucleotide metabolism also involves redundant and convergent biosynthetic pathways. Deoxyribonucleotide triphosphate (dNTP) pools required for DNA replication and repair can be produced by the *de novo* pathway (DNP) or by the nucleoside salvage pathway (NSP) (Fig. 4.1 A) (Reichard, 1988). The DNP uses glucose and amino acids to generate ribonucleotide disphosphates (NDPs), which are converted to deoxyribonucleotide diphosphates (dNDPs) by ribonucleotide reductase (RNR). The same dNDPs can also be produced via the NSP (Reichard, 1988) starting with extracellular deoxyribonucleosides (dNs) which are imported in the cell via specialized transporters. The first enzymatic steps in the cytosolic NSP are catalyzed by two kinases: thymidine kinase 1 (TK1) phosphorylates thymidine (dT), while deoxycytidine kinase (dCK) phosphorylates deoxycytidine (dC), deoxyadenosine (dA) and deoxyguanosine (dG) (Reichard, 1988). The relevance of these two NSP kinases for

dNTP production in normal and malignant cells is yet to be defined. Since dN substrates for the NSP kinases are absent from most cell culture media, it has been assumed that the NSP is dispensable for DNA replication (Xu et al., 1995). However, recent in vivo findings have challenged this assumption. For example, we reported impaired hematopoiesis in *dCK*$^{-/-}$ mice, due to dCTP pool deficiency, resulting in replication stress (RS), S-phase arrest and DNA damage in hematopoietic progenitors (Austin et al., 2012; Toy et al., 2010). Analyses of *dCK*/*TK1* double-knockout mice showed that NSP-derived dCTP synthesis is required to compensate for the inhibition of *de novo* dCTP production (Austin et al., 2012) (Fig. 4.1 A). The mechanism of DNP inhibition involves allosteric regulation of RNR-mediated reduction of cytidine diphosphate (CDP) to deoxycytidine disphosphate (dCDP) by dTTP produced via TK1 from endogenous dT (Austin et al., 2012) (Fig. 4.1 A).

Production of dNTPs by the NSP may be therapeutically relevant in cancer. For example, the ability of cancer cells to switch their dCTP synthesis from the DNP to the NSP may explain why dT given as a single dCTP-depleting agent showed limited efficacy in clinical trials (Chiuten et al., 1980; Kufe et al., 1980; Kufe et al., 1981). If correct, this hypothesis suggests that a combination of dT (to inhibit DNP mediated dCTP production) along with a dCK inhibitor (to co-target dCTP production by the NSP), would be more efficacious in killing tumor cells than either treatment alone. Here we investigate this possibility in the context of acute lymphoblastic leukemia (ALL). We demonstrate that co-targeting both *de novo* and salvage pathways for dCTP biosynthesis is well-tolerated in mice, and is efficacious in T-ALL and B-ALL models. We also describe a Positron Emission Tomography (PET)-based assay to non-

invasively monitor in vivo pharmacological targeting of dCTP biosynthesis in cancer cells.

Materials and Methods

Cell lines and culture conditions

Human cell lines CCRF-CEM, Jurkat, MOLT-4, RSR4;11 and TF-1, cells were obtained from ATCC. NALM-6 and L1210-10K cells were a kind gift from Michael Teitell (UCLA) and Charles Dumontet (Universite´ Claude Bernard Lyon I, Lyon, France), respectively. All cell lines were maintained in 5% FBS in RPMI-1640 and were grown at 37°C, 20% O_2, and 5% CO_2.

Animals

Mice were bred and housed under specific pathogen-free conditions and were treated in accordance with the UCLA Animal Research Committee protocol guidelines. The *dCK*$^{-/-}$ were generated and bred as previously described and backcrossed to C57BL/6 mice for *n*=7 generations (Austin et al., 2012; Toy et al., 2010). Age-matched (5-12 wk-old) WT and *dCK*$^{-/-}$ littermates were used to assess RS induction by dT in BM myeloid cells.

Reagents, antibodies, immunoblotting and flow cytometry

Thymidine, 2'-deoxycytidine, hydroxyurea, 5-FU and cisplatin were purchased from Sigma-Aldrich and were prepared in DMSO or water. Lentiviral shRNA constructs against dCK and non-targeting control were from Sigma-Aldrich. For cell culture assays, dCK inhibitors were resuspended in DMSO. Immunoblotting was performed as previously described (Austin et al., 2012). Antibodies and reagents for immunoblotting were purchased from the following vendors: Cell Signaling Technology, phospho-Chk1 Ser345, phospho-Chk2 Thr68, Chk1, Chk2, anti-mouse HRP-conjugated IgG , anti-rabbit HRP-conjugated IgG; Sigma-Aldrich, dCK, Beta-Actin; Abcam, TK1. Bound

antibody was detected with using chemiluminescence immunoblotting detection reagents (Pierce). Isolation and FACS phenotyping of hematopoietic stem cells, EryA and myeloid was performed as previously described (Austin et al., 2012). The $p185^{BCR\text{-}ABL}/Arf^{-/-}$ cells were identified using an anti-CD19 (APC) antibody. For cell cycle analyses, total DNA content was determined using 1 µg/mL of DAPI or 20 µg/mL propidium iodide containing 5 µg/mL RNAase A. Annexin V staining was performed according to the manufacturer's protocol (BD Biosciences). For the micronucleus assay, isolated bone marrow cells were stained with the following antibodies from eBioscience: Ter119 PerCP-Cy5.5 (TER-119), CD71 APC (R17217), CD45 PE-Cy7 (30-F11), CD61 PE (2C9.G3), CD11b APC-eFluor780 (M1/70). Cells were stained, washed and fixed with Cytofix/Cytoperm solution (BD Biosciences). Cells were then washed and stained with 1 µg/mL DAPI in PBS/2% FBS. All flow cytometry data were acquired on a four-laser LSRII cytometer (BD Biosciences) and analyzed using FlowJo (Tree Star).

Measurements of dT and DI-39 pharmacokinetics in mice

NOD SCID gamma (NSG) mice were injected with 2 g/kg dT intraperitoneally; 75 µL of whole blood was obtained at 0, 2, 4, and 8 hr through retro-orbital sinus bleed using hematocrit capillary tubes. Whole blood was immediately centrifuged at 3000x*g* for 5 min to isolate serum; 30 µL of serum was mixed with 1 mL methanol:acetonitrile (1:9), vortexed for 2 min, centrifuged at 14,000x*g* for 4 min at 4^{o} C. Extraction was repeated and the pooled supernatant was dried under vacuum centrifugation. The residue was dissolved in 100 µL water, filtered and eluted through a Waters microBondapak C18 column under a gradient mobile phase from 2% methanol to 50% methanol over ten

minutes at a flow rate of 1.5 mL/min. Thymidine was detected by absorbance intensity (254 nm), and concentrations were interpolated from standard curves.

To determine the pharmacokinetic profile of DI-39, C57Bl/6 female mice were dosed with DI-39 via intraperitoneal injection following the protocol that was described previously (Murphy et al., 2013). Dose formulation include 10% DMSO and 40% Captisol (SBE-β-CD, a polyanionic variably substituted sulfobutyl ether of β-cyclodextrin, (Stella and He, 2008)) in water. Approximately 75 µL of whole blood was obtained at various time points starting 5 to 360 minutes through retro-orbital sinus bleed using hematocrit capillary tubes. Approximated values of the Area Under the Curve (AUC), clearance rate (CL), half-life ($T_{1/2}$), maximum concentration in the plasma (C_{max}) and time to reach the maximum concentration (T_{max}) were calculated using Boomer/Multi-Forte PK Functions from Microsoft Excel.

For the DI-39 tumoral and plasma uptake study using LC/MS/MS-MRM, tumor-bearing NSG mice were injected with 50 mg/kg DI-39 intraperitoneally at 0, 2, 4, 8 and 12 hours prior to sacrifice. Whole tumors were excised, weighed and homogenized with an equal volume of 2 mm-diameter stainless steel beads (Next Advance) in 1 mL ice-cold acetonitrile/water (50/50, v/v) containing 0.5 pmol/µL of the internal standard DI-70 (2-(((2-(4-methoxy-3-(2-(2-(2-methoxyethoxy)ethoxy)ethoxy)phenyl)-5-propylthiazol-4-yl)methyl)thio)pyrimidine-4,6-diamine, $C_{25}H_{35}N_5O_5S_2$, MW = 549.2 g/mol, an in-house synthesized DI-39 analog) in a Bullet Blender homogenizer (Next Advance). Tissue homogenates were left overnight at 4^{o} C on a shaker and the next day centrifuged at

20,000x*g* for 10 min. The supernatant (700 µL) was transferred to a clean tube and was evaporated to dryness in a vacuum centrifuge. The residue was reconstituted in 100 µL acetonitrile/water (50/50, v/v). For plasma measurements, ~100 µL of blood was collected through a retro-orbital sinus bleed using capillary blood collection tubes. Samples were centrifuged at 20,000x*g* for 5 min, and 30 µL of the supernatant was transferred into a clean tube. The sample was mixed with 500 µL ice-cold acetonitrile/water (50/50, v/v) containing the internal standard and processed in the same way as the tumor homogenates. Calibration standards were prepared by spiking working stock solution of DI-39 in tumor homogenates and plasma from untreated mice to give the following ranges: 0.02 to 20 pmol/µL. Samples (5 µL) were injected onto a reverse phase column (Agilent ZORBAX Rapid Resolution High Definition (RRHD) Eclipse Plus C18, 2.1 x 50 mm, 1.8 µm) equilibrated in water/acetonitrile/formic acid, 95/5/0.1 and eluted (200 µL/min) with and increasing concentration of solvent B (acetonitrile/formic acid, 100/0.1, v/v: min/% acetonitrile; 0/5, 0/5, 2/5, 8/80, 9/80, 10/5, 12/5). The effluent from the column was directed to an electrospray ion source (Agilent Jet Stream) connected to a triple quadrupole mass spectrometer (Agilent 6460 QQQ) operating in the positive ion MRM mode. The ion transitions for DI-39 and DI-70 (525.2→383.3 and 550.2→408.2 respectively) were recorded under previously optimized conditions. The DI-39 peak areas were normalized to the internal standard and tumor weight.

The experiment using CCRF-CEM cells to measure the uptake of DI-39 in cell culture followed a similar protocol as the one described above. CCRF-CEM cells were cultured

in 5% FBS in RPMI-1640 media supplemented with 1 μM of DI-39 for 10, 30, 40, and 60 min before cell extraction. For some samples, the media with 1 μM DI-39 was removed and the cells were washed three times in PBS before adding fresh media without DI-39 for 60 minutes. The cells were extracted and homogenized in 1 mL ice-cold acetonitrile/water (50/50, v/v) containing 0.5 pmol/μL of the same internal standard as mentioned before. The cell extract was left overnight at 4^{o} C on a shaker and the next day centrifuged at 20,000x*g* for 10 min. The supernatant was transferred to a clean tube and was evaporated to dryness in a vacuum centrifuge. The residue was reconstituted in 100 μL acetonitrile/water (50/50, v/v). DI-39 was quantified as described above.

Incorporation of stable isotope labeled glucose and deoxycytidine into the free dCTP pool and into DNA

CEM cells were transferred into RPMI supplemented with 5% dialyzed FCS containing 10 μM uniformly labeled [U-^{13}C/^{15}N]-deoxycytidine (Cambridge Isotopes), 2 g/L uniformly-labeled [U-^{13}C]-glucose (Cambridge Isotopes) and 0, 50 or 250 μM dT. For the dNTP analysis, the cells were extracted overnight at -20 ºC with 75% methanol. The extracts were then heated in boiling water for 3 min, pelleted, and the supernatants were transferred and dried under vacuum centrifugation. For DNA analysis, cells were collected and genomic DNA was extracted using the Quick-gDNA MiniPrep kit (Zymo Research). Genomic DNA was then digested to nucleosides using the DNA Degradase Plus kit (Zymo Research).

For the in vivo studies, tumor-bearing mice were injected with 200 μL of 2.5 mM [U-^{13}C/^{15}N]-deoxycytidine 30 min prior to sacrifice. Tumors were harvested, mechanically

digested into single cells, and cell counts were obtained. DNA extraction was carried out as described above.

DNA hydrolysis samples were diluted 1/1 with solvent A (water/formic acid, 100/0.2, v/v) and analyzed using a modified version of a previously reported method (Cohen et al., 2009) in which aliquots of the solution (10 µL) were injected onto a porous graphitic carbon column (Thermo Hypercarb, 100 x 2.1 mm, 3 micron particle size) equilibrated in solvent A and eluted (300 µL/min) with an increasing concentration of solvent B (acetonitrile/min/% B; 0/0, 6/60, 6.1/100, 9/100, 9.1/0, 10/0). The effluent from the column was directed to Agilent Jet Stream connected Agilent 6460 QQQ operating in the positive ion MRM mode. After verification of retention times using authentic standards, the peak areas of the $MH^+ \rightarrow$fragment ion transitions for the dC isotopomers (M_0, 228.1→112.1; M_1, 229.1→112.1; M_2, 230.1→112.1; M_3, 231.1→112.1; M_4, 232.1→112.1; M_5, 233.1→112.1; M_6, 234.1→113.1; M_7, 235.1→114.1; M_8, 236.1→115.1; 236.1→115.1; M_{11}, 239.1→118.1; and M_{12}, 240.1→119.1) were recorded with instrument manufacturer-supplied software (Agilent MassHunter), and normalized to cell number. The dC isotopomers of M_3 through M_8 for the DNP and M_{11} through M_{12} for NSP were detected and used for data analysis.

For free dNTP analysis a modified version of the same previously reported method (Cohen et al., 2009) was used in which dried samples were re-dissolved in solvent C (100 µL, 5 mM hexylamine, 0.5% mM diethylamine, pH 10.0) and aliquots (10 µL) were injected onto porous graphitic carbon column (Thermo Hypercarb, 150 x 2.1 mm, 3

micron particle size) equilibrated in solvent C and eluted (150 µL/min) with an increasing concentration of solvent D (acetonitrile/min/% D; 0/0. 5/0, 25/40, 25.1/100, 30/100, 30.1/0, 40/0). The effluent from the column was directed to the same instrument described above, operating in the negative ion mode. After verification of retention times using authentic standards, the intensities of pre-selected $(M-H)^-$→fragment ion transitions for various dCTP isotopmers (M_0, 466.0→159.0; M_1, 467.0→159.0; M_2, 468.0→159.0; M_3, 469.0→159.0; M_4, 470.0→159.0; M_5, 471.0→159.0; M_6, 472.0→159.0; M_7, 473.0→159.0; M_8, 474.0→159.0; M_{10}, 478.0→159.0; M_{11}, 479.0→159.0; and M_{12}, 478.0→159.0) were recorded, again with instrument manufacturer-supplied software (Agilent MassHunter), and normalized to cell number. The dCTP isotopomers of M_5 through M_8 for the DNP and M_{12} for NSP were detected and used for data analysis. The M_3 and M_4, isotopomers were not detected.

dNTP pool measurements

Intracellular dNTP pool measurements were conducted as previously described (Austin et al., 2012).

Comet assay

The comet assay was performed following the Trevigen CometAssay reagent kit protocol under alkaline conditions. For quantification, four random sections of each slide containing >100 cells were imaged and Olive Tail Moment obtained using TriTek Cometscore software.

Generation of luciferase viral construct and retroviral gene transduction

The gene encoding humanized secreted *Gaussia* luciferase (sGluc), pCMV-GLuc-1 (Nanolight Technology), was subcloned into the MSCV-IRES-GFP retroviral vector. Pheonix-Ampho cells were transfected with the generated vector using Lipofectamine transfection reagent (Invitrogen, Grand Island, NY). Forty-eight hours after transfection, virus was harvested and used to transduce CEM dCK^{wt} and CEM dCK^{low} cells. GFP positive cells were sorted with a FACSAria II cell sorter (BD Biosciences).

Crystallization of DI-39 in complex with dCK and UDP

The C4S S74E dCK variant used for crystallographic studies was expressed and purified as described elsewhere.(Nomme et al., 2014). Crystallization, X-ray data collection and refinement were also performed as described in Nomme et *al.* Briefly, crystals of dCK in complex with UDP, $MgCl_2$ and a 2.5-fold excess of the DI-39 inhibitor were grown using the hanging drop vapor diffusion method at 12 ºC. The reservoir solution contained 0.9-1.5 M trisodium citrate dehydrate and 25 mM HEPES (pH 7.5). Diffraction data were collected at the Advanced Photon Source, Argonne National Laboratory on Life Sciences-Collaborative Access Team (LS-CAT) beamlines 21 ID-G.

Mouse xenograft tumor models and treatments

CEM xenograft tumors were developed in 8 to 12 week old female NSG mice by implanting 2 x 10^6 CEM dCK^{wt}-sGluc-GFP and/or dCK^{low}-sGluc-GFP cells in 100 µL of equal volume Matrigel (BD Biosciences) and RPMI subcutaneously in the flanks. Tumor growth was monitored daily by caliper measurements ([(length x $width^2$)/2]) and blood *Gaussia* luciferase (GLuc) assay (Tannous, 2009). Ten µL of blood was collected via tail vein nick and mixed with 2 µL 50 mM EDTA. One µL of blood was mixed with 99 µL

PBS and transferred to a 96 well OptiPlate (Perkin Elmer). One hundred µL of 20 µM coelenterazine substrate was mixed and luciferase activity was measured using a plate luminescence microplate reader SpectraMax L (Molecular Devices). Systemic tumor models were established by intravenous injection of 10^6 CEM dCK^{wt}-sGluc-GFP or dCK^{low}-sGluc-GFP in 100 µL RPMI. Thymidine (2 g/kg) was administered in saline and DI-39 in a mixture of 1.4% DMSO and 40% Captisol (Ligand Pharmaceuticals) mixture.

TUNEL assay

Tumors from CEM xenografts were harvested and fixed overnight in 10% buffered formalin solution. Samples were then paraffin-embedded and 5 µm sections were mounted on glass slides. TUNEL staining was performed according to the manufacturer's protocol (Roche Applied Science). Stained slides were subsequently scanned on an Aperio ScanScope AT (Aperio) and analysis was conducted using Definiens Tissue Studio 64 (Dual) 3.5 (Definiens AG).

dCK kinase and uptake assays

These assays were performed as previously described (Shu et al., 2010).

Peripheral blood counts

All mice were anesthetized and whole blood was obtained through cardiac puncture. For peripheral blood counts, samples were collected in tubes containing EDTA and submitted to UCLA Division of Lab Animal Medicine for analysis.

PET imaging

PET/CT studies were performed as previously described (Radu et al., 2008; Shu et al., 2010).

Pharmacokinetic studies of DI-39 in mice.

This assay was performed as previously described (Murphy et al., 2013).

Statistical analyses

All statistics presented as averages of biological replicates with standard error of the mean (± SEM), unless indicated. *P* value significances were calculated from multiple replicates within a data set representative of multiple independent experiments, as indicated, using one sample t-test function in GraphPad Prism 5 (GraphPad Software).

Results

Deoxycytidine salvage *via* dCK prevents dT-induced lethal replication stress in T-ALL cells

Treatment with dT increases cytosolic dTTP concentration, resulting in allosteric inhibition of dCTP production via the DNP (Fig. 4.1 A) (Reichard, 1988). Accordingly, in CCRF-CEM (CEM) human T-ALL cells, dT increased dTTP and decreased dCTP in a dose-dependent manner (Fig. 4.1 B). Early S-arrest (Fig. 4.1 C) was induced by concentrations of dT as low as 50 μM, which increased dTTP ~20-fold and reduced dCTP ~5-fold (Fig. 4.1 B). Supplementation of CEM cultures with 2.5 μM dC completely prevented dT-induced S-phase arrest (Fig. 4.1 C). Addition of dC did not prevent S-phase arrest in CEM cells treated with the RNR inhibitor hydroxyurea, 5-fluorouracil (5-FU) or cisplatin (Fig. 4.1 D), indicating that dC salvage plays a specific role in counteracting dT-induced S-phase arrest.

To study the role of dCK in the prevention of dT-induced S-phase arrest by dC addition, we generated CEM dCK^{low} cells (Fig. 4.1 E) using a dCK-targeted shRNA vector. Knocking down dCK reduced ^{3}H-deoxycytidine uptake by ~95% (Fig. 4.1 F) and decreased cytosolic dCTP levels by ~30% (Fig. 4.1 G), but did not perturb normal cell cycle progression (Fig. 4.1 H). Supplementation of cell culture media with 2.5 μM dC restored the dCTP pool in dT-treated dCK^{wt} cells to ~55% of its baseline value, but had no effect on dT-induced dCTP pool depletion in dCK^{low} cells (Fig. 4.1 G). Consequently, dC addition prevented dT-induced S-phase arrest only in CEM dCK^{wt} cells (Fig. 4.1 C), but not in CEM dCK^{low} cells (Fig. 4.1 H). Accordingly, in the presence of both dT and dC, only dCK^{low} but not dCK^{wt} CEM cells displayed (i) activation of the RS response marker

Chk1 phosphorylated on Ser345 (pChk1) (Fig. 4.1 I), (ii) induction of DNA damage, as determined by activation of Chk2 phosphorylated on Thr68 (pChk2) (Fig. 4.1 I), pH2A.X staining by flow cytometry (Fig. 4.1 J), as well as by comet assay (Fig. 4.1 K) and (iii) apoptosis (Fig. 4.1 L). Thus, downregulation of dCK expression in CEM cells abolished their ability to compensate for dT-mediated inhibition of dCTP production via the DNP, resulting in dCTP depletion, stalled DNA replication, RS, DNA damage and apoptosis.

In T-ALL cells dT triggers a metabolic switch to NSP dCTP production and upregulates dC salvage

To investigate the biochemical mechanism by which the NSP compensates for dT-mediated DNP inhibition, we quantified the contributions of each dCTP biosynthetic pathway to both the free cytosolic dCTP and the dCTP incorporated into the DNA. CEM cells were incubated for 12 hr with [U-^{13}C]-glucose, the substrate for the DNP, and with [U-^{13}C/^{15}N]-dC, the substrate for the NSP (Fig. 4.2 A). Heavy isotope labeled dCTP species were detected by combined liquid chromatography-tandem mass spectrometry in the multiple reaction-monitoring mode (LC/MS/MS-MRM). Mass additions between 3 and 8 identified dCTP produced from [U-^{13}C]-glucose via the DNP, while mass additions between 11 and 12 identified dCTP produced from [U-^{13}C/^{15}N]-dC via the NSP (Fig. 4.2 A).

In untreated CEM cells, the free dCTP pool produced from dC via the NSP over a 12 hr labeling period was ~5-fold larger than the free dCTP pool originating from glucose via the DNP (Fig. 4.2 B). However, ~2.5 fold more dCTP incorporated into DNA was produced by the DNP than by the NSP (Fig. 4.2 B). Treatment with dT decreased dCTP

production from glucose via the DNP, in both the free cytosolic and DNA dCTP pools (Fig. 4.2 B). Moreover, dT increased the utilization of the NSP-produced dCTP for DNA synthesis more than 3-fold over baseline values (Fig. 4.2 B). These findings support previous observations that, under basal conditions, DNA synthesis relies primarily on the DNP-produced dCTP (Xu et al., 1995). Accordingly, the large size of the NSP-derived free dCTP pool in untreated CEM cells (Fig. 4.2 B) likely reflects its inefficient utilization for DNA replication under basal conditions. Notably, the NSP-derived free dCTP pool did not decrease in dT treated cells, even though the utilization of this pool for DNA synthesis increased significantly (Fig. 4.2 B). This finding, suggests that dT upregulates dCTP production via the NSP, which is consistent with a marked increase in dCK activity (Fig. 4.2 C) and in dC uptake (Fig. 4.2 D) in dT-treated CEM cells.

In vivo, salvage of endogenous dC rescues T-ALL cells from RS induced by dT treatment

To examine whether findings from cell culture studies (Fig. 4.1; Fig. 4.2) can be recapitulated in vivo, subcutaneous (s.c.) CEM dCK^{wt} and dCK^{low} xenografts were established in NOD SCID gamma (NSG) mice. Plasma dT peaked at ~1.5 mM two hours after treatment with a single dT injection (2 g/kg, intraperitoneally) and then rapidly declined to baseline values (~10 μM) at 8 hr (Fig. 4.3 A). Intratumoral dTTP increased in both dCK^{wt} and dCK^{low} tumors for at least 4 hr after dT administration (Fig. 4.3 A). In dCK^{wt} tumors, dT induced a slight and transient upregulation of pChk1 at the 2 and 4 hr time points (Fig. 4.3 B). In marked contrast, a more pronounced and sustained pChk1 upregulation was induced by dT treatment in dCK^{low} tumors (Fig. 4.3 B). These

findings suggest that dCK is required to enable CEM cells to resist RS induced by dT treatment in vivo.

To understand the role of dCK in dCTP production and utilization in tumors from dT treated mice, we measured the free dCTP pool and incorporation of NSP-produced dCTP into the DNA. During the 0-4 hr timeframe, dCTP decreased several fold in both CEM dCK^{wt} and dCK^{low} xenografts and then started to recover as plasma dT dropped to baseline values (Fig. 4.3 C). Notably, intratumoral dCTP recovery occurred significantly slower in the dCK^{low} xenografts than in their wild type counterparts (Fig. 4.3 C). To quantify the effects of dT treatment on the utilization of the NSP-produced dCTP for DNA synthesis, tumor-bearing mice were treated with dT or vehicle for 3.5 hr and were then pulsed with [U-^{13}C/^{15}N]-labeled dC. Thirty minutes later, mice were sacrificed to measure the incorporation of dCTP produced from labeled dC into tumor DNA by LC/MS/MS-MRM (Fig. 4.3 D). In tumors from vehicle treated mice, ~2-fold less dCTP produced from [U-^{13}C/^{15}N]-labeled dC was incorporated into the DNA of dCK^{low} tumors than in the DNA of their dCK^{wt} counterparts (Fig. 4.3 E). In dT treated mice, labeled dCTP incorporation into DNA increased ~3-fold in dCK^{wt} tumors, but remained unchanged in the dCK^{low} xenografts (Fig. 4.3 E). Together with the pattern of pChk1 upregulation shown in Fig. 4.3 B, these findings suggest that upon dT treatment in vivo, dCK activity is required to maintain tumor DNA replication, thereby preventing RS induction. Moreover, similar to in vitro findings (Fig. 4.2B), dT treatment in vivo increases the incorporation of NSP-produced dCTP into tumor DNA.

To determine if the increase in the utilization of the NSP-produced dCTP for DNA synthesis in tumors from dT treated mice is also associated with an upregulation of the NSP as shown in vitro (Fig. 4.2, C and D), we took advantage of ^{18}F-L-FAC (1-L-(2' deoxy-2',-^{18}Fluoroarabinofuranosyl) cytosine), a fluorinated dC analog (Radu et al., 2008; Shu et al., 2010). ^{18}F-L-FAC crosses the cell membrane via nucleoside transporters and accumulates specifically in dCK expressing cells by a phosphorylation-dependent mechanism (Fig. 4.3 F); dCK-dependent phosphorylated ^{18}F-L-FAC retention in living animals can be imaged and quantified non-invasively by Positron Emission Tomography (PET). As anticipated, dCK^{low} tumors accumulated ~40% less ^{18}F-L-FAC than dCK^{wt} tumors (Fig. 4.3 F). Four hours after dT treatment, ^{18}F-L-FAC accumulation increased by ~20% in dCK^{wt} tumors (Fig. 4.3 G). ^{18}F-L-FAC accumulation also increased in dCK^{low} tumors (Fig. 4.3 G), likely because of their residual dCK activity. However, the NSP upregulation in the dCK^{low} tumors was insufficient to maintain DNA synthesis and prevent RS induction, as indicated by both the marked and sustained pChk1 upregulation in dCK^{low} tumors from dT treated mice (Fig. 4.3 B) and by the low incorporation in dCK^{low} tumors of stable isotope labeled dCTP into the DNA (Fig. 4.3 E).

The NSP mediates T-ALL cell resistance to dT treatment in vivo

Since the NSP is required to prevent dT-induced RS in T-ALL cells in culture (Fig. 4.1 I) and in vivo (Fig. 4.3 C), we determined if downregulation of dCK expression synergizes with dT treatment to induce tumor regression in mice. CEM dCK^{wt} and dCK^{low} s.c. tumor-bearing mice were treated with dT (2 g/kg) twice daily for 6 days. Prolonged dT administration blocked the growth of CEM dCK^{low} tumors without affecting the dCK^{wt} xenografts, as shown by (i) serial measurements of secreted *Gaussia* luciferase, which

served as an indicator of tumor burden in peripheral blood (Tannous, 2009) (Fig. 4.4 A) and (ii) end point measurements of tumor sizes (Fig. 4.4 B) and weights (Fig. 4.4 C). The synergy between dT treatment and shRNA-mediated dCK downregulation suggests that pharmacological dCK inhibition, combined with dT administration, may provide a new therapeutic strategy in ALL.

Development of DI-39, a small molecule, high affinity dCK inhibitor which occupies the substrate binding site of the kinase

To examine whether the NSP can be exploited therapeutically through pharmacological dCK inhibition, we screened selected chemical libraries comprising ~90,000 small molecules. This high throughput screen (HTS) identified DI-0120 (Fig. 4.5 A), a dCK inhibitor with an IC_{50} of 1.4 μM in CEM cells. Subsequent structure-activity relationship (SAR) studies yielded DI-39 (Fig. 4.5 B), a cell-permeable (Fig. 4.5 C) lead candidate with an IC_{50} of 5 nM, nearly 300-fold lower than that of DI-0120 (Fig. 4.5 D and (Murphy et al., 2013)). To investigate how DI-39 inhibits dCK we obtained a 2.1 Å co-crystal structure, which showed DI-39 occupying the nucleoside-binding site of the kinase and not the nucleotide phosphoryl donor-binding site (Fig. 4.5 E). This mode of binding suggested that DI-39 is highly specific inhibitor of dCK.

To evaluate DI-39 further, we measured its effects on the dCTP pool of CEM cells. While treatment with either DI-39 (1 μM) or dT (50 μM) decreased dCTP by ~30%, the DI-39/dT combination was synergistic, reducing dCTP in CEM cells by ~70% (Fig. 4.5 F). While in the presence of dC neither dT nor DI-39 alone induced RS or apoptosis in CEM cells, the DI-39/dT combination triggered both RS, as measured by pChk1

upregulation (Fig. 4.5 G) and apoptosis, as measured by Annexin V staining (Fig. 4.5 H). Notably, when the dCK-null leukemia cell line L1210-10K (Jordheim et al., 2004) was treated with increasing concentrations of DI-39 far above those required to inhibit dCK activity or to kill CEM cells when combined with dT, it did not induce apoptosis, further supporting the selectivity of DI-39 for dCK (Fig. 4.5 I). The DI-39/dT combination also induced RS (Fig. 4.5 J) and apoptosis (Fig. 4.5 K) in four other ALL cell lines (Jurkat, MOLT-4, RS4;11, NALM-6) as well as in an erythroleukemia cell line (TF-1). In summary, DI-39 enters cells, inhibits the NSP-dependent dCTP production, and synergizes with dT to induce lethal RS in multiple leukemia cell lines.

DI-39 inhibits tumor dCK activity in vivo and promotes RS when combined with dT

To evaluate DI-39 in vivo, we determined its pharmacokinetics (PK) in plasma and in tumor tissues. The plasma half-life of DI-39 was ~50 min (Fig. 4.6 A) and detectable amounts of drug (~15 nM) were present in tumor tissues 8 hr after single dose administration (Fig. 4.6 B). To correlate the amount of DI-39 in plasma and tumor at 2, 4, 8 and 12 hr following administration of the drug with the pharmacodynamic (PD) effect of DI-39 (i.e. inhibition of tumor dCK activity), we performed ^{18}F-FAC PET/CT scans of CEM tumor-bearing mice at these time points (Fig. 4.6 C). DI-39 (50 mg/kg, administered intraperitoneally) reduced ^{18}F-FAC accumulation in tumors by ~30% for up to 8 hr (Fig. 4.6 D). This level of reduction was comparable with that obtained in the dCK knockdown model (Fig. 4.3 E). The timing of recovery of tumor dCK activity, determined with PET, following DI-39 administration, indicates that sustained target

inhibition could be obtained by administering DI-39 every 12 hr. Notably, this information could not be obtained from conventional plasma PK measurements (Fig. 4.6 A).

To further investigate the effects of DI-39 on tumor dCTP metabolism, 5.5 hr after treatment with dT and/or DI-39, CEM tumor-bearing mice were pulsed for 30 min with [U-^{13}C/^{15}N]-dC. LC/MS/MS-MRM was used to quantify label incorporation into DNA. Analogous to our dCK knockdown results (Fig. 4.3 F), DI-39 significantly reduced [U-^{13}C/^{15}N]-dC incorporation into the DNA of CEM cells (Fig. 4.6 E). Moreover, the DI-39/dT combination promoted RS in CEM tumors, as evidenced by pChk1 upregulation (Fig. 4.6 F). Together, these findings indicate that (i) DI-39 efficiently inhibits tumor dCK activity in vivo for up to 12 hr, (ii) the DI-39/dT combination induces RS in CEM cells in vivo and (iii), PET imaging provides a useful PD companion biomarker for DI-39.

Pharmacological co-targeting of DNP and NSP dCTP biosynthesis with DI-39 and dT blocks the growth of T-ALL xenografts in mice

The therapeutic efficacy of the DI-39/dT combination was first tested in mice bearing established s.c. CEM xenografts. Only the combination therapy dramatically reduced tumor burden in these mice, as indicated by end point tumor sizes (Fig. 4.7 A) and weights (Fig. 4.7 B). In addition, TUNEL staining from harvested tumors indicated significant induction of DNA breaks only with the DI-39/dT combination (Fig. 4.7 C). In contrast to findings shown in Fig. 4.4, dT treatment alone had a small but significant effect on the size and weight of CEM tumors (Fig. 4.7, A and B). This difference is likely explained by a slight increase in dT PK by the Captisol/DMSO formulation used to co-administer DI-39 with dT; DI-39 has limited solubility in aqueous saline solutions. The

therapeutic efficacy of the DI-39/dT combination was further confirmed in a systemic T-ALL model, in which CEM cells were injected intravenously. In the systemic T-ALL model, treatment with dT alone induced an ~7-fold reduction in the percentage of leukemic cells in bone marrow (BM) relative to vehicle and DI-39 treated groups (Fig. 4.7 D). This finding suggests that BM-resident leukemic cells are more susceptible to dT in vivo than they are in cell culture. However, the DI-39/dT combination reduced tumor burden by an additional 100-fold relative to dT alone, indicating strong synergy between these two therapeutic agents (Fig. 4.7 D). Therefore, pharmacological co-targeting of both the DNP and NSP dCTP biosynthetic pathways is highly effective against CEM leukemic cells in vivo.

The combination therapy is effective against a primary B-ALL systemic model and has minimal effects on the normal hematopoietic progenitor pool

We next assessed the efficacy of the DI-39/dT combination therapy against short-term cultures of murine BCR-ABL (p185), $Arf^{-/-}$ pre-B ALL cells ($p185^{BCR-ABL}/Arf^{-/-}$) (Boulos et al., 2011; Williams et al., 2006). While primary B-ALL cells were sensitive in culture to the DI-39/dT combination, they required 4-fold more dT than the CEM T-ALL cell line for optimal induction of apoptosis (Fig. 4.8 A). This finding is consistent with previous clinical observations that B-ALL are less sensitive to dT treatment than T-ALL (Kufe et al., 1980). To evaluate the efficacy of dT and/or DI-39 in an in vivo B-ALL model, firefly luciferase marked $p185^{BCR-ABL}/Arf^{-/-}$ cells were inoculated intravenously in NSG mice. Eleven days post-inoculation, bioluminescence imaging (BLI) of firefly luciferase-marked $p185^{BCR-ABL}/Arf^{-/-}$ ALL-bearing NSG mice treated with vehicle or DI-39 (50 mg/kg) revealed substantial systemic disease with focal BM and spleen localization (Fig. 4.8 B).

While dT (2 g/kg) treatment significantly reduced BLI signals in BM and spleen, the addition of DI-39 had a more pronounced effect than dT alone (Fig. 4.8, B and C). To confirm the BLI findings, we also analyzed the leukemia burden in BM by flow cytometry using CD19 (a B cell marker which, in NSG mice, is present only on the leukemia cells) (Fig. 4.8 D). Treatment with dT induced a significant decrease in the percentage of $p185^{BCR\text{-}ABL}/Arf^{-/-}$ ALL cells relative to vehicle-treated mice (Fig. 4.8 D). The addition of DI-39 resulted in an additional ~2-fold reduction in the percentage of leukemic cells compared to dT alone (Fig. 4.8 D). These findings, using primary $p185^{BCR\text{-}ABL}/Arf^{-/-}$ cells, indicate that the DI-39/dT combination is effective against an aggressive in vivo B-ALL model.

In parallel with analyses of BM resident leukemic cells, we also assessed the effects of the combination therapy on the hematopoietic progenitor pool. We analyzed the $Lineage^{-}$ $Sca\text{-}1^{+}$ $c\text{-}Kit^{+}$ (LSK) HSC population as well as short-term (ST), long-term (LT) and multipotent progenitor (MPP) hematopoietic progenitor cells. With the exception of a minor decrease in the percentage of LSK upon dT treatment (Fig. 4.8 E), there were no significant changes between control and treated groups (Fig. 4.8, E and F). Therefore, the combination therapy preferentially targets BM-resident leukemia cells while sparing normal hematopoietic progenitors. In addition, DI-39 alone or in combination with dT, when administered twice/day for 7 days in NSG mice, did not affect body weight (Fig. 4.8 G), and had no detectable effects on RBCs, hemoglobin, platelets or neutrophils (Fig. 4.8 H).

Partial inhibition of dCK in hematopoietic tissues prevents hematological toxicity from dT and DI-39

To further investigate the potential hematological toxicity of the combination therapy, we took advantage of our *dCK*$^{-/-}$ mice (Austin et al., 2012). This approach allowed us to directly compare the effects on the hematopoietic system induced by complete loss of dCK function in the *dCK*$^{-/-}$ mice with the effects induced pharmacologically in *dCK* wild type mice (*dCK*$^{+/+}$) by DI-39 and dT. In the erythroid lineage, the DI-39/dT combination induced markedly less DNA damage and genotoxicity in the *dCK*$^{+/+}$ mice, as measured by pH2A.X staining (Fig. 4.9 A) and the micronucleus assay, respectively (Fig. 4.9 B), than did *dCK* gene elimination alone in *dCK*$^{-/-}$ mice. These findings indicate that pharmacological inhibition of dCK activity by DI-39, alone or in combination with dT treatment, is better tolerated than complete elimination of dCK enzymatic activity by genetic *dCK* gene inactivation.

Discussion

We demonstrate here a requirement for a functional nucleoside salvage pathway in T-ALL and B-ALL cells to prevent dCTP pool insufficiency, RS and apoptosis following pharmacological inhibition of *de novo* dCTP synthesis. We introduce DI-39, a new small molecule inhibitor of dCK; dCK is the kinase required for the compensatory metabolic switch, triggered by dT-mediated DNP inhibition, to NSP-dependent dCTP biosynthesis. We elucidate how DI-39 inhibits dCK by obtaining a high-resolution crystal structure of the inhibitor-dCK complex. We demonstrate the therapeutic efficacy of co-targeting both the DNP and NSP dCTP biosynthetic pathways, using in vivo models of T-ALL and B-ALL, without detectable toxicity against normal hematopoietic progenitors. We also

describe a companion pharmacodynamic PET assay of dCK enzyme activity, which allows non-invasive in vivo imaging of pharmacological interventions targeting dCTP biosynthesis.

Selectivity of the DI-39/dT combination therapy for leukemic cells relative to normal hematopoietic progenitors

Our current working model to explain the mechanism and observed selectivity of the combination therapy for leukemia cells relative to normal hematopoietic progenitors is depicted schematically in Fig. 4.9, C and D. According to this model, pharmacological co-targeting of the DNP (by dT) and of the NSP (by DI-39) is highly effective at inducing lethal RS against T- and B-ALL cells and has minimal effects on normal hematopoietic cells. As indicated by ^{18}F-FAC PET imaging of dCK activity (Fig. 4.6 D; Fig. 4.9D), DI-39 induced partial inhibition of dCK in normal BM cells compared with the complete loss of dCK activity in *dCK*$^{-/-}$ mice (Austin et al., 2012; Toy et al., 2010). The residual dCK activity in BM cells following DI-39 treatment may be sufficient to prevent the more substantial reductions observed for the dCTP pools of hematopoietic progenitors in the *dCK*$^{-/-}$ mice. This model of low or absent toxicity due to partial inhibition of the therapeutic target is reminiscent of recent work in which hypomorphic ATR suppression was lethal to tumor tissues exposed to oncogenic stress, yet had only minimal toxicity to normal tissues (Bartek et al., 2012; Schoppy et al., 2012). Furthermore, the enhanced susceptibility of ALL cells to a reduced supply of dCTP could reflect the inherent inability of these leukemic cells to mount an efficient RS response. While additional studies are required to precisely identify the defects in cell cycle checkpoints that increase the susceptibility of ALL cells to RS induced by dNTP insufficiency, when compared to

normal hematopoietic progenitor cells, we note the presence of inactivating *TP53* mutations in several tested ALL cell lines. In this context, it has been suggested that, in normal cells with wild type p53, the skewing in dNTP pools induced by inhibition of *de novo* pyrimidine synthesis by N-(phosphonacetyl)-L-aspartate (PALA) creates reversible DNA damage, sufficient to activate p53 and induce the expression of proteins that provide protective arrest at multiple cell cycle checkpoints (Hastak et al., 2008). In cancer cells with defects in p53 or in its downstream effectors, failure to arrest DNA synthesis when pyrimidine dNTP pools are depleted leads to irreversible DNA damage that eventually causes apoptosis (Hastak et al., 2008).

Potential clinical implications

High avidity for dT has been previously identified as a potential metabolic liability of certain cancers, leading to clinical studies using high dT doses as a potential therapeutic (O'Dwyer et al., 1987). Prolonged (over 5 days) dT infusions have shown responses in heavily pre-treated T-ALL and cutaneous T-cell lymphoma patients, with the side effects encountered being tolerable, manageable, and reversible (Chiuten et al., 1980; Kufe et al., 1980; Kufe et al., 1981). However, therapeutic responses to dT in these patients were, in general, limited and transient, potentially reflecting the ability of the NSP, via dCK, to compensate for the dCTP-depleting effect of dT. Since potent small molecule inhibitors of dCK have recently been described (Murphy et al., 2013; Yu et al., 2010), future clinical studies can determine if the anti-leukemic activity of dT reported in T-ALL and cutaneous T cell-lymphoma patients can be significantly improved by pharmacological blockade of the deoxycytidine salvage pathway.

Companion diagnostics for therapies targeting dCTP biosynthetic pathways in cancer

The data presented here provide examples of both in vivo and in vitro companion diagnostics (or biomarkers) that could assist the clinical translation of the DI-39/dT combination therapy. For example, direct assessments of temporal changes in tumor dCK activity in vivo with PET were more useful than conventional plasma pharmacokinetic measurements for identifying the optimal schedule for the DI-39/dT combination therapy (Fig. 4.6). Since our PET assays for monitoring dCK activity have already been translated to humans (Schwarzenberg et al., 2011), approaches similar to those described in our pre-clinical experiments could be used in future clinical trials to non-invasively monitor dCK inhibition in target tissues in vivo. Upregulation of pChk1 and pH2A.X levels by leukemia cells upon DI-39/dT treatment (Fig. 4.6 F) could provide additional pharmacodynamic biomarkers of DNA damage, as shown previously for PARP inhibitors (Fong et al., 2009). Furthermore, since the efficacy of the DI-39/dT therapy depends on the capacity of tumors cells to take up large amounts of dT and convert it to dTTP, PET imaging using ^{18}F-FLT (3'-deoxy-3'-fluorothymidine), a probe for dT metabolism (Shields et al., 1998), may enable the identification of tumors with unusually high avidity for dT. Thus, ^{18}F-FLT PET may match the proposed definition of a predictive or enrichment biomarker (de Bono and Ashworth, 2010) for dT-based therapies.

Regulation of the NSP by the DNA damage response pathway

Our in vitro (Fig. 4.2 C) and in vivo data (Fig. 4.3, E and F) indicate that, in CEM T-ALL cells, dT treatment upregulated the activity of the NSP. While NSP upregulation by dT

treatment may result from a decrease in the negative feedback by dCTP on dCK activity (Datta et al., 1989), additional mechanisms could also be involved. For example, dCK activity is increased by treatment with DNA damaging agents that do not affect dCTP production via the DNP (Csapo et al., 2003; Ooi et al., 1996). Moreover, dCK activation following DNA damage involves phosphorylation of the kinase on serine 74 (Yang et al., 2012). This serine is part of an SQ/TQ motif, which is a typical phosphorylation site for ATM and ATR kinases in the DNA damage response (DDR) pathway. Indeed, dCK has been identified as a direct target of these kinases (Matsuoka et al., 2007). Therefore, following DNA damage induced by high dose dT, and, potentially, by other genotoxic therapies, the DDR pathway may promote NSP upregulation via post-translational regulation of dCK in order to expand dNTP pools and facilitate DNA repair. If correct, this model provides a rationale for testing dCK inhibitors in combination with radiation therapy and other genotoxic therapies.

In summary, our results provide new insight into the nucleotide metabolism of leukemic cells and also demonstrate a new therapeutic strategy to overcome the redundancy and adaptability of nucleotide metabolism in ALL and, possibly, in other hematological malignancies in which uncontrolled expansion of the dTTP pool by dT treatment results in a potential metabolic liability. Similar approaches, which fit within the conceptual framework of targeting non-oncogene addiction (Luo et al., 2009), may be applicable to other redundant biosynthetic pathways that provide survival advantages to tumor cells.

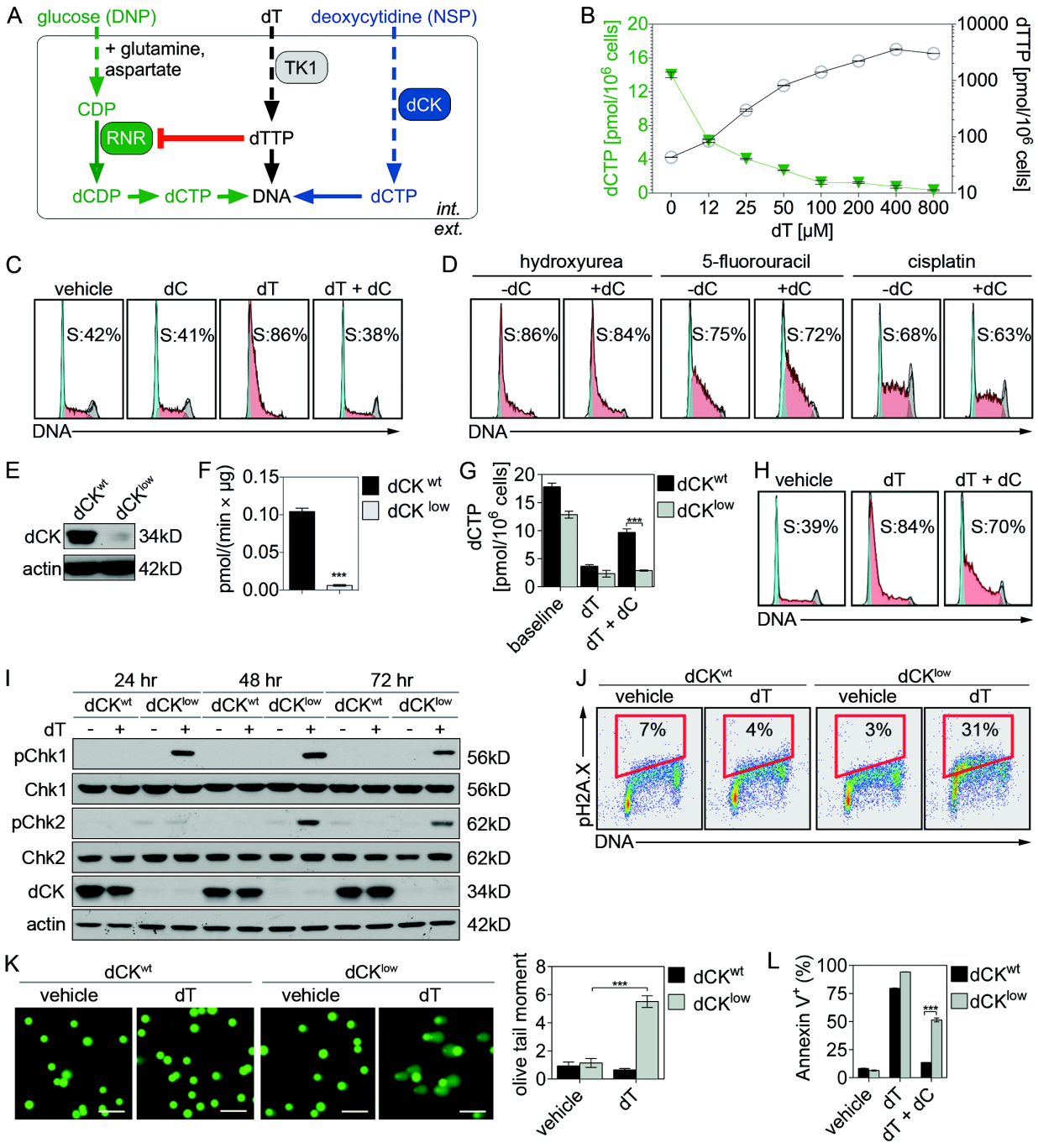

Figure 4.1. Deoxycytidine (dC) salvage via dCK prevents thymidine (dT)-induced lethal replication stress (RS) in T-ALL cells.

(**A**) Allosteric control of DNP dCTP production by dT via dTTP. RNR: ribonucleotide reductase. (**B**) Effects of dT treatment (24 hr) on dCTP and dTTP pools. Values represent mean ± SEM. (**C**) CEM cell cycle analysis following treatment with vehicle or dT (50 μM) -/+ 2.5 μM dC for 24 hr. (**D**) CEM cell cycle analysis following treatment with

hydroxyurea (50 μM), 5-fluorouracil (15 μM) or cisplatin (1.6 μM) for 24 hr -/+ 2.5 μM dC. (**E**) Representative immunoblots of dCK and actin expression and (**F**) dCK kinase assay in CEM dCK^{wt} (scrambled shRNA) cells and dCK^{low} (shRNA against dCK) cells. Values are mean ± SEM, *** $P<0.001$ (**G**) dCTP levels in CEM dCK^{wt} and dCK^{low} cells treated for 24 hr with vehicle or dT (50 μM) -/+ dC (2.5 μM). Values are mean ± SEM, *** $P<0.001$ (**H**) Cell cycle analysis of CEM dCK^{low} cells treated with vehicle or dT (50 μM) -/+ 2.5 μM dC for 24 hr. (**I**) Representative immunoblots detecting Chk1, pChk1 (Ser345), Chk2, pChk2 (Thr68), dCK and actin in CEM dCK^{wt} and dCK^{low} cells treated with vehicle or dT (50 μM) in the presence of 2.5 μM dC for 24, 48 and 72 hr. (**J**) pH2A.X (Ser139) and DNA content (DAPI) in CEM dCK^{wt} and dCK^{low} cells treated with vehicle or dT (50 μM) in the presence of 2.5 μM dC for 24 hr. (**K**) Representative images and quantification of the COMET assay conducted on CEM dCK^{wt} and dCK^{low} cells 48 hr after treatment with vehicle or dT (50 μM) in the presence of 2.5 μM dC. Values represent the mean Olive Tail Moment ± SEM from 100 cells per image x 4 images/group; $n=2$ independent experiments. *** $P<0.001$. Magnification: 4x. (**L**) Annexin V staining of CEM dCK^{wt} and dCK^{low} cells following treatment with vehicle, dC (2.5 μM), dT (50 μM) or dC + dT for 72 hr. All values are mean ± SEM from at least three replicates/data point. *** $P<0.001$. All data in Fig. 4.1 are representative of $n=3$ independent experiments, unless indicated.

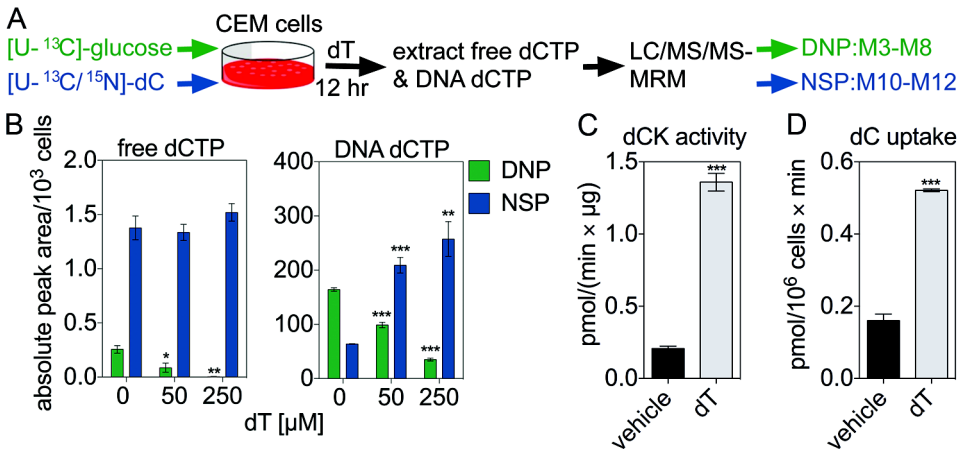

Figure 4.2. Treatment with dT triggers a metabolic switch to NSP-mediated dCTP biosynthesis in T-ALL cells and upregulates the NSP

(**A**) Schematic of the [U-^{13}C]-glucose and [U-^{13}C/^{15}N]-deoxycytidine (dC) stable isotope labeling approach used to determine the source (DNP or NSP) of the free dCTP pool and of the dCTP incorporated into the DNA of CEM cells treated with various dT concentrations. (**B**) dCTP derived from [U-^{13}C]-glucose (DNP) and [U-^{13}C/^{15}N]-dC (NSP) in the free dCTP pool and incorporated into the DNA of CEM cells after 12 hr of incubation with stable isotope-labeled DNP and NSP precursors, in the presence or absence of dT. Values are the average of absolute peak area/10^3 cells ± SEM, * P< 0.05, ** P<0.01, *** P<0.001, compared with 0 μM dT control. Data are representative of n=2 independent experiments. (**C**) Quantification of dCK kinase activity in CEM cells at baseline and after 8 hr of treatment with 50 μM dT. Data are representative of n=2 independent experiments. Values are mean ± SEM, *** P<0.001. (**D**). Quantification of the uptake of ^{3}H-labeled deoxycytidine (dC) by CEM cells at baseline and after 4 hr of treatment with 50 μM dT. Data are representative of n=2 independent experiments. Values represent mean ± SEM, *** P<0.001.

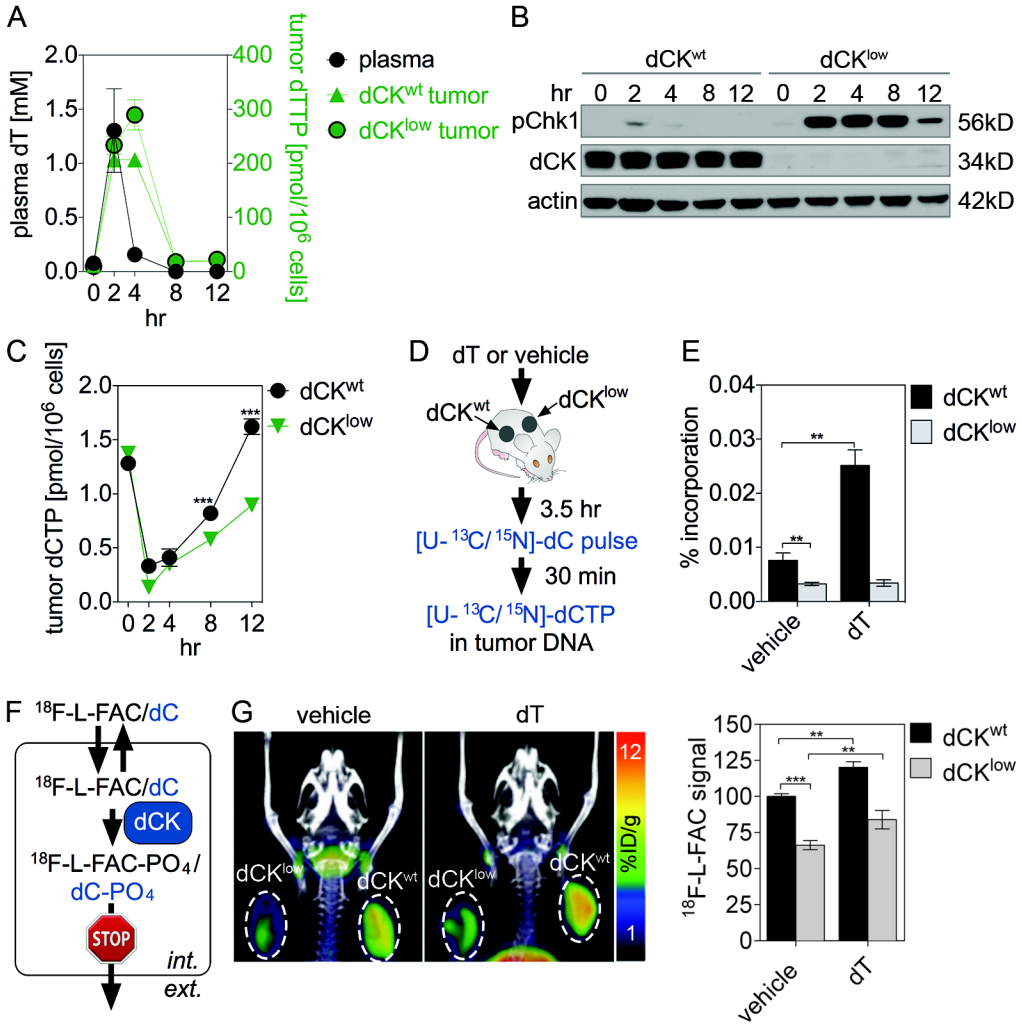

Figure 4.3. In vivo, salvage of endogenous dC rescues T-ALL cells from RS induced by dT treatment.

(A) *Left axis*: Plasma dT levels in NSG mice treated with dT (2 g/kg; single-dose). Values are mean ± SEM from *n*=3 mice/time point; *n*=2 independent experiments. *Right axis*: dTTP concentrations from CEM dCK^{wt} and dCK^{low} tumors at various time points following single-dose dT (2 g/kg) treatment; values are mean ± SEM, *n*=4 mice/time point; *n*=2 independent experiments. (**B**) Representative immunoblot (*n*=3 independent experiments) showing pChk1 (Ser345) levels at various time points in bilateral s.c. CEM dCK^{wt} and dCK^{low} tumors implanted in NSG mice treated with dT (2 g/kg; single-dose). (**C**) dCTP concentrations from CEM dCK^{wt} and dCK^{low} tumors at various time points following single-dose dT (2 g/kg) treatment; values are mean ± SEM, *n*=5 mice/time point; *n*=2 independent experiments. *** *P*<0.001. (**D**) Schematic of experimental design

for quantifying the incorporation of [U-^{13}C/^{15}N]-dC into the DNA of dCK^{wt} and dCK^{low} CEM tumors 4 hr after single-dose treatment with 2 g/kg dT or vehicle. (**E**) Quantification of the LC/MS/MS-MRM data for labeled dCTP incorporation into the DNA. Data are mean ± SEM of *n*=6 mice/group; *n*=2 independent experiments. ** *P*<0.01. (**F**) Schematic of the in vivo PET assay of dCK activity. (**G**) ^{18}F-L-FAC uptake in s.c. CEM dCK^{wt} and dCK^{low} tumor xenografts 4 hr following vehicle or dT injection. Values represent the mean % decrease in ^{18}F-FAC signal relative to dCK^{wt} vehicle ± SEM, *n*=4 mice/group; *n*=2 independent experiments. ** *P*<0.01, *** *P*<0.001.

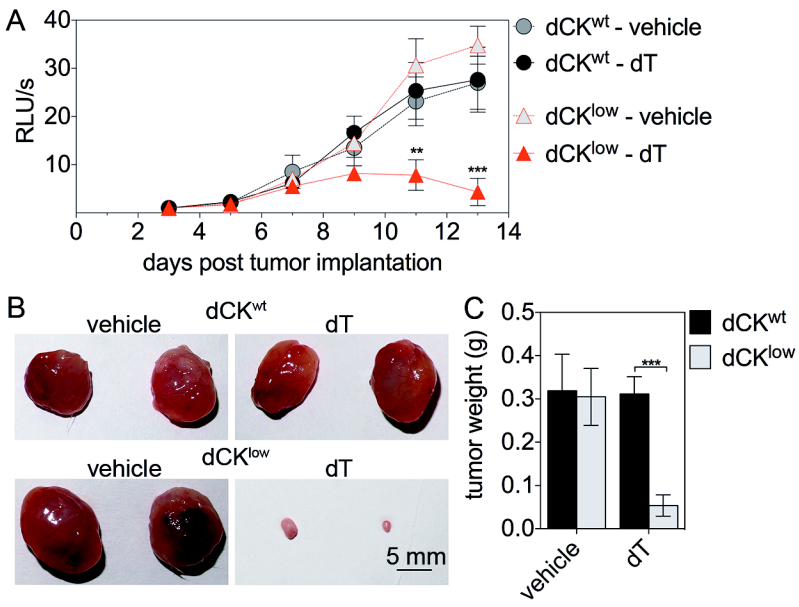

Figure 4.4. dCK mediates resistance to dT in T-ALL cells in vivo

(**A**) Serial secreted *Gaussia* luciferase measurements of peripheral blood from NSG mice bearing CEM dCK^{wt} or dCK^{low} s.c. tumors (*n*=6 mice/condition) treated every 12 hours with vehicle or dT (2 g/kg) starting at day 7 post-tumor implantation until day 13. Values represent mean ± SEM; *n*=2 independent experiments. ** *P*< 0.01, *** *P*<0.001 compared with dCK^{low} vehicle at indicated time point (**B**) CEM dCK^{wt} and dCK^{low} tumors from vehicle or dT-treated mice from (**A**). (**C**) Tumor weights (mg) from (**A**). Values represent the mean ± SEM; *n*=2 independent experiments. *** *P*<0.001.

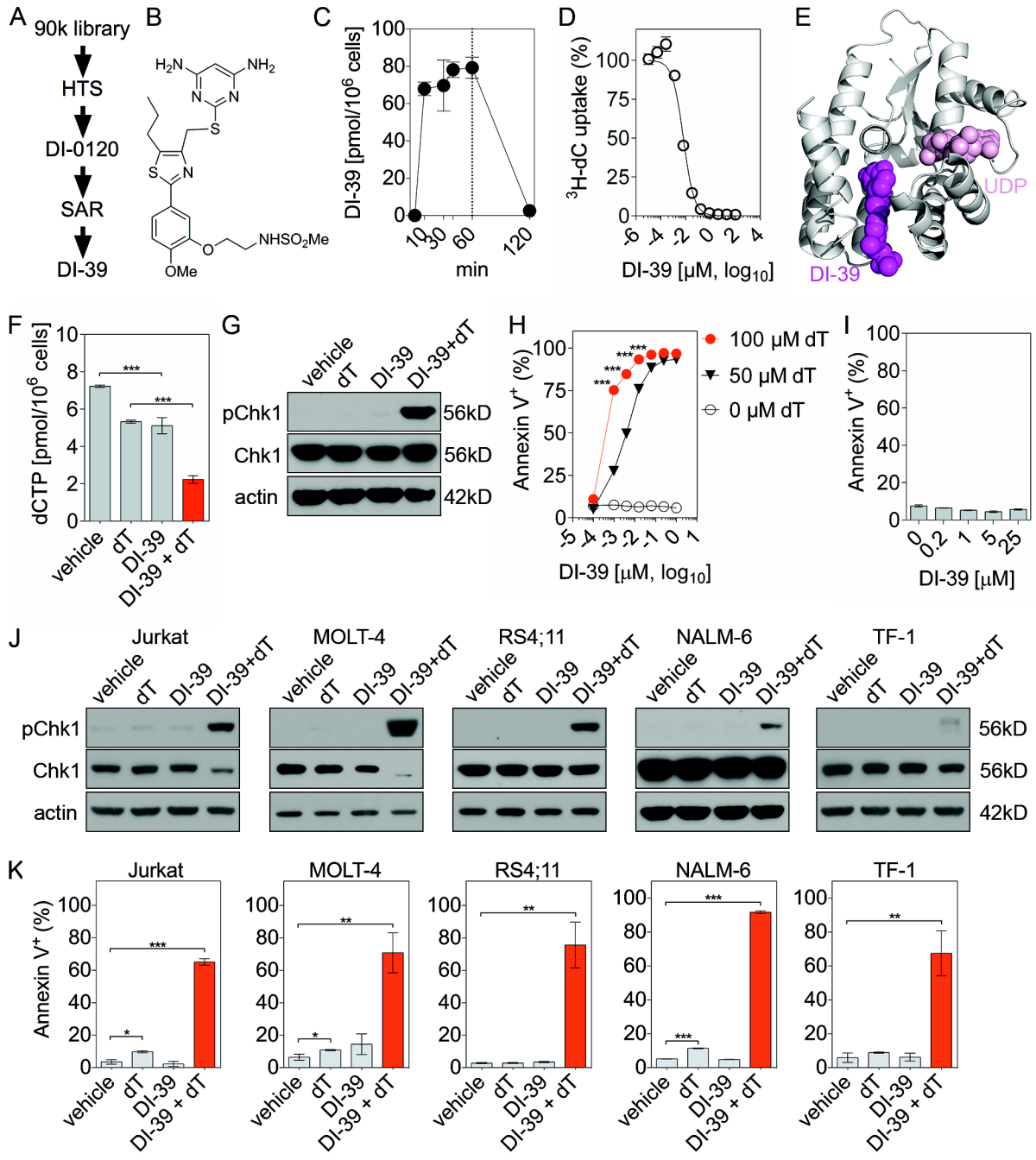

Figure 4.5. Development of DI-39, a small molecule dCK inhibitor that synergizes with inhibition of *de novo* dCTP biosynthesis in leukemic cells

(A) Schematic illustrating the development of DI-39, beginning with high-throughput screen (HTS) of a 90,000 compound library, which provided the initial hit DI-0120. Further structural activity relationship (SAR) yielded 80 novel compounds including DI-

39. (**B**) Chemical structure of DI-39. (**C**) LC/MS/MS-MRM measurements of DI-39 in CEM cells exposed to 1 μM drug for indicated periods of time. Cells were washed three times after 60 min (indicated by vertical line) and cellular drug retention was measured again 60 min later. Values represent mean ± SEM (**D**) IC_{50} value of DI-39 determined by % inhibition of ^{3}H-dC uptake by CEM cells. Values represent mean ± SEM (**E**) 2.1 Å crystal structure of dCK with bound DI-39 and uridine diphosphate (UDP). (**F**) Intracellular dCTP concentrations in cultured CEM dCK^{wt} cells treated with vehicle, dT (50 μM), DI-39 (1 μM) or DI-39 + dT for 24 hr. Values represent the mean ± SEM; *n*=2 independent experiments. *** *P*<0.001. (**G**) Representative immunoblots detecting Chk1, pChk1 (Ser345), and actin in CEM cells treated with vehicle, dT (1 mM), DI-39 (100 nM) or DI-39 + dT in the presence of 2.5 μM dC for 24 hr. (**H**) Annexin V staining of CEM cells treated for 72 hr with indicated concentrations of DI-39 and dT in the presence of 2.5 μM dC. Values are mean ± SEM; *n*=2 independent experiments, *** *P*<0.001 compared with 50 μM dT. (**I**) Annexin V staining of L1210-10 dCK null cells treated for 72 hr with indicated concentrations of DI-39. Values represent the mean % cells staining positive for Annexin V ± SEM; *n*=2 independent experiments. (**J**). Representative immunoblots of Jurkat, MOLT-4, RSR4;11, NALM-6 and TF-1 leukemia cells treated with vehicle, dT (1 mM), DI-39 (100 nM) or DI-39 + dT in the presence of 2.5 μM dC for 24 hr (NALM-6) or 72 hr (Jurkat, MOLT-4, RSR4;11, TF-1). (**K**) Annexin V staining of the same panel of leukemia cell lines as in (**J**) treated for 72 hr with vehicle, dT (1 mM), DI-39 (100 nM), or DI-39 + dT. Cultures were supplemented with 2.5 μM dC. Values represent mean % cells staining positive for Annexin V ± SEM; *n*=3 independent experiments. * *P*<0.05, ** *P*<0.01, *** *P*<0.001.

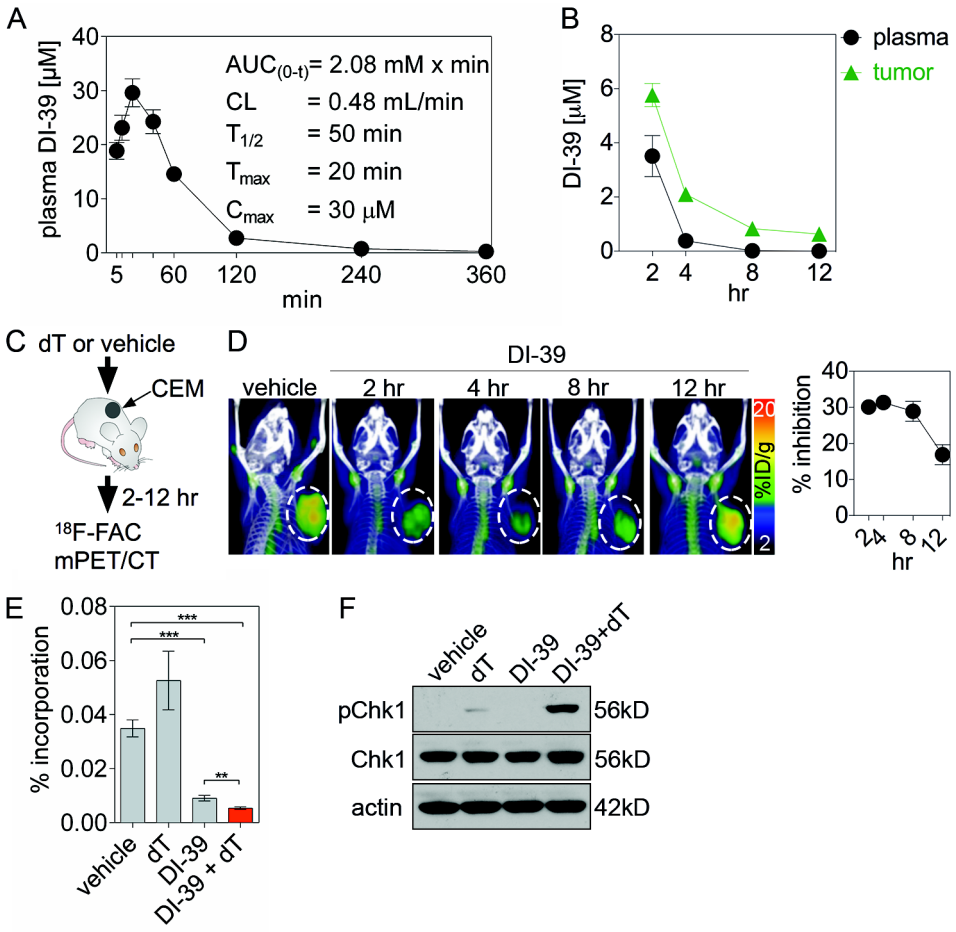

Figure 4.6. DI-39 inhibits dCK activity in vivo as determined by ^{18}F-FAC PET and promotes RS when combined with dT

(**A**) Pharmacokinetic profile of DI-39. C57Bl/6 mice were dosed with DI-39 via intraperitoneal injection. Dose formulation: 10% DMSO and 40% Captisol (SBE-β-CD, a polyanionic variably substituted sulfobutyl ether of β-cyclodextrin, (Stella and He, 2008) in water. Approximated values of the Area Under the Curve (AUC), clearance rate (CL), half-life ($T_{1/2}$), maximum concentration in the plasma (C_{max}) and time to reach the maximum concentration (T_{max}) were calculated using Boomer/Multi-Forte PK Functions for Microsoft Excel. Values represent the mean ± SD, *n*=4/time point; *n*=2 independent experiments**.** (**B**) LC/MS/MS-MRM quantification of DI-39 concentrations in plasma and CEM tumors at various time points after treatment. See Methods for details. Values represent the mean ± SD, *n*=4/group. (**C**) Schematic illustration of the ^{18}F-FAC PET/CT study to determine in vivo dCK inhibition by DI-39 in CEM s.c. xenografts. (**D**) Time course of in vivo ^{18}F-FAC PET/CT scans to determine dCK inhibition by DI-39 (single

intraperitoneal injection, 50 mg/kg). Values represent the mean % decrease in ^{18}F-FAC signal ± SD, *n*=4 mice/group; *n*=2 independent experiments. **(E**) % incorporation of [U-^{13}C/^{15}N]-dC into the DNA of CEM xenografts 5.5 hr after single-dose treatment with vehicle, DI-39 (50 mg/kg), dT (2 g/kg) or DI-39 + dT; mice were pulsed with the stable isotope-labeled dC for 30 min before sacrifice. Values represent mean ± SEM, *n*=4/group; *n*=2 independent experiments. ** *P*<0.01, *** *P*<0.001. (**F**) Representative immunoblots of pChk1 (Ser345), Chk1, and actin in tumor tissues collected from mice 6 hr following treatment with DI-39 (50 mg/kg), dT (2 g/kg) or both agents; *n*=3 independent experiments.

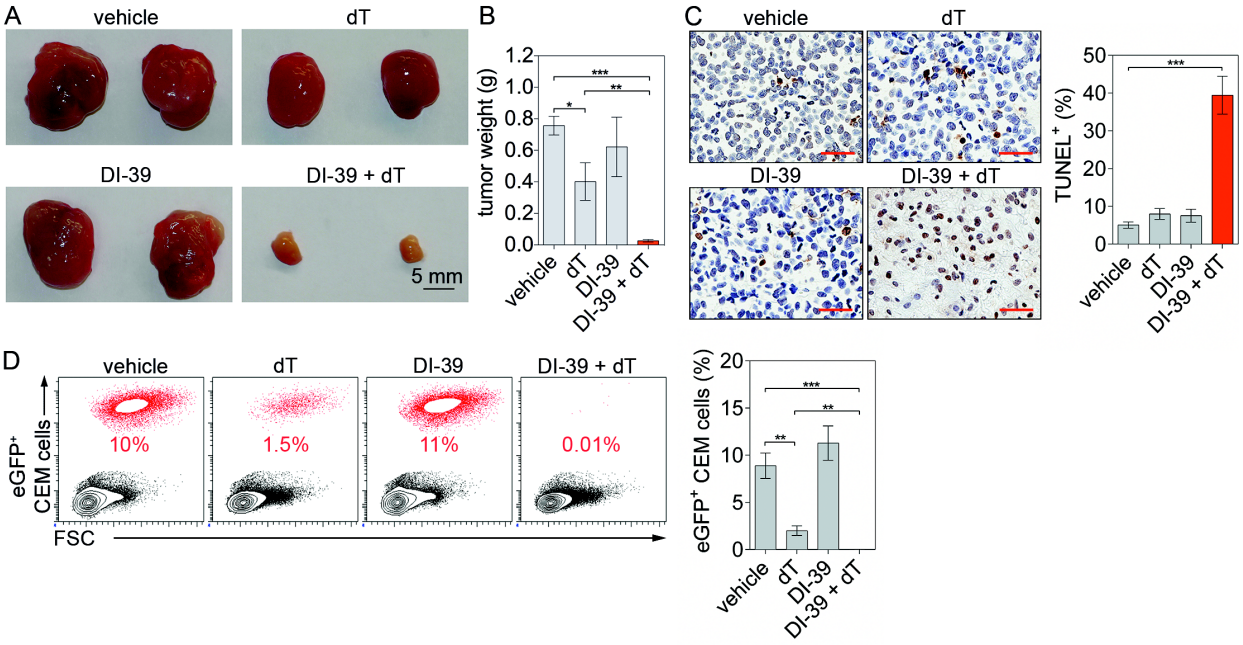

Figure 4.7. Pharmacological co-targeting of DNP and NSP dCTP production is effective against T-ALL cells in vivo

(**A**) Representative images of CEM xenografts isolated from mice treated with vehicle, dT (2 g/kg), DI-39 (50 mg/kg) or DI-39 + dT every 12 hr beginning at day 7 post inoculation and continuing to day 14. *n*=6 mice/group; *n*=2 independent experiments. (**B**) Tumor weights from (**A**). Values represent mean ± SEM; *n*=2 independent experiments, *n*=6 mice/group. * *P*<0.05, ** *P*<0.01, *** *P*<0.001. (**C**) Representative images and quantification of TUNEL staining of tumor samples from (**A**). Magnification: 20x. Values represent mean ± SEM. *n*=6 mice/group. *** *P*<0.001. (**D**) Representative FACS plots and quantification of eGFP+ CEM leukemia cells in the bone marrow of NSG mice treated with vehicle, dT (2 g/kg), DI-39 (50 mg/kg) or DI-39 + dT. Mice (*n*=6/group) were treated every 12 hr beginning at day 3 post inoculation with $1.0x10^6$ CEM cells. Values represent mean ± SEM; *n*=2 independent experiments. ** *P*<0.01,, *** *P*<0.001.

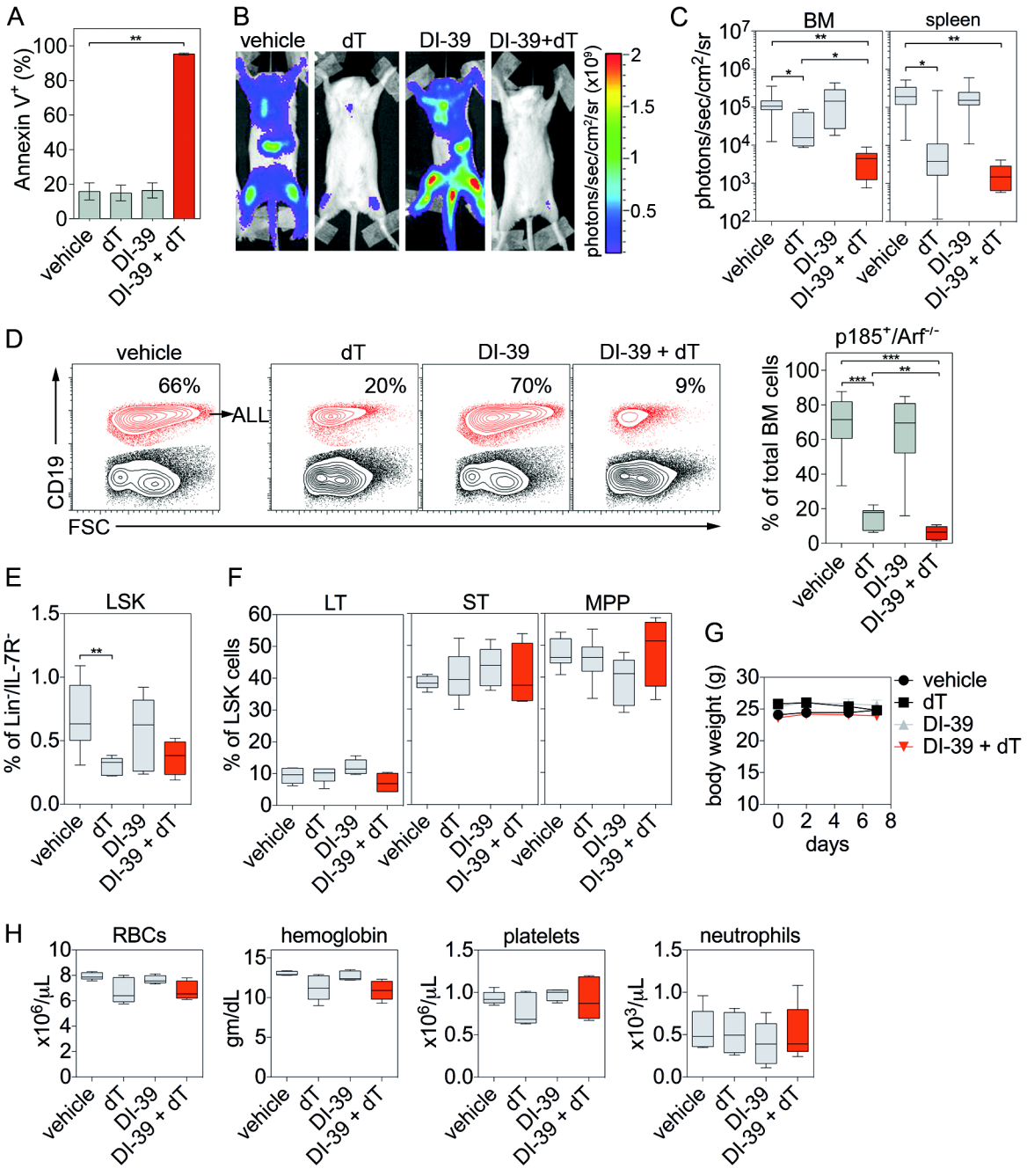

Figure 4.8. Pharmacological co-targeting of the DNP and NSP is efficacious against primary mouse p185$^{BCR-ABL}$ *Arf* $^{-/-}$ Pre-B ALL cells, while sparing the hematopoietic progenitor pool

(**A**) Annexin V staining of p185$^{BCR-ABL}$ *Arf* $^{-/-}$ pre-B cells following 48 hr treatment with vehicle, dT (200 µM), DI-39 (100 nM), or DI-39 + dT in the presence of 2.5 µM dC. Values are mean ± SEM; *n*=2 independent experiments. ** *P*<0.01. (**B**) Representative

bioluminescent images (BLI) of mice (*n*=6/group) treated with vehicle, dT (2 g/kg), DI-39 (50 mg/kg) or DI-39 + dT at day 14 post intravenous injection of $2.0x10^4$ pre-B leukemia cells/mouse. (**C**) Quantification of BLI from in BM and spleen. * *P*<0.05, ** *P*<0.01. (**D**) Representative FACS analyses and quantification of CD19+ leukemic cells in the BM of treated mice. ** *P*<0.01, *** *P*<0.001. (**E**) Quantification of Lineage$^-$ Sca-1$^+$ c-Kit$^+$ (LSK) populations from treated mice. ** *P* <0.01. (**F**) LSK cells from BM of treated mice were analyzed for expression of CD34 and Flt3 to identify and quantify long-term (LT, CD34$^-$, Flt3$^-$), short-term (ST, CD34$^+$, Flt3$^-$), and multipotent progenitor (MPP, CD34$^+$, Flt3$^+$) stem cells. (**G**) Body weights as well as RBC, hemoglobin, platelet, and neutrophil measurements (**H**) of NSG mice (*n*=6/group) treated with vehicle, dT (2 g/kg), DI-39 (50 mg/kg), or DI-39 + dT every 12 hr for 7 days. Data represent mean ± SEM. All data are representative of at least two independent experiments.

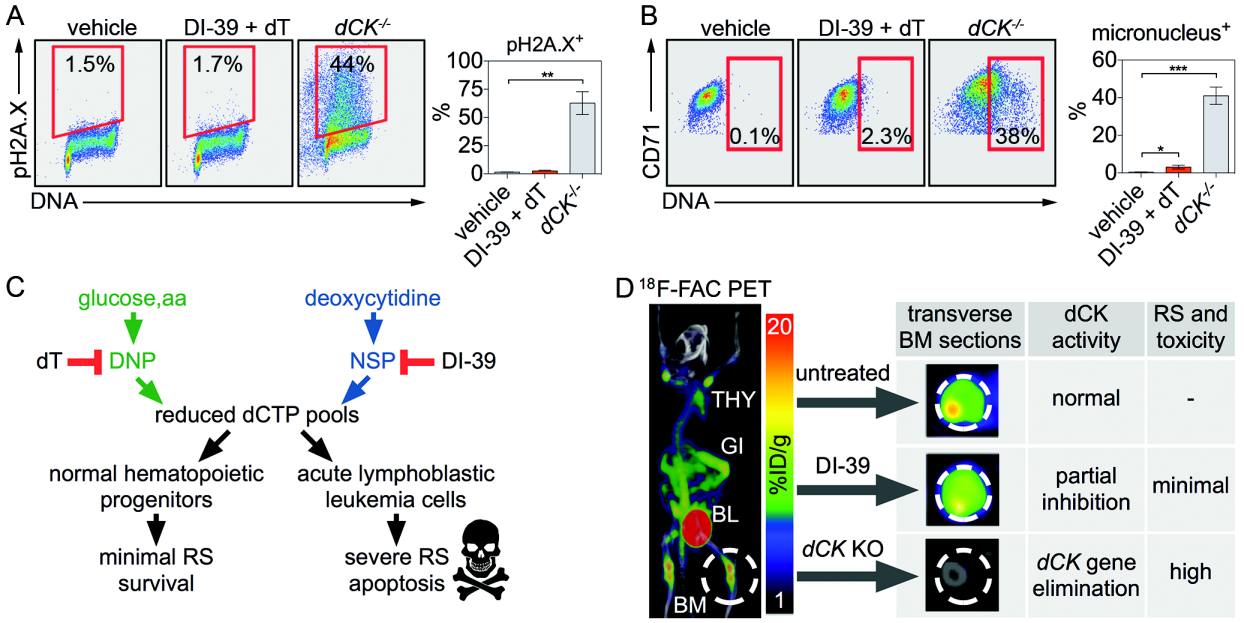

Figure 4.9. Assessment of potential toxicity of the DI-39/dT combination therapy and model

(**A**) Representative FACS staining of pH2A.X and data quantification in EryA ($CD71^{+}$/ high forward scatter) erythroblasts to estimate endogenous (for $dCK^{-/-}$ mice, *n*=4 mice/group) or potential pharmacologically-induced (DI-39 + dT) genotoxic stress. NSG mice (*n*=5 mice/group) were treated with vehicle or combination of DI-39 (50 mg/kg) and dT (2 g/kg) every 12 hr for 8 days. Values are mean ± SEM. ** *P*<0.01. (**B**) Representative FACS plots and quantification of micronucleated erythrocytes indicative of endogenous (for $dCK^{-/-}$ mice) or potential pharmacologically-induced (DI-39 + dT) genotoxic stress. Values represent mean ± SEM from *n*=2 independent experiments. * *P*<0.05, *** *P* <0.001. (**C**, **D**) Proposed rationale for explaining the selectivity of the combination therapy for leukemia cells relative to normal hematopoietic progenitors (see text for details).

References

Austin, W.R., A.L. Armijo, D.O. Campbell, A.S. Singh, T. Hsieh, D. Nathanson, H.R. Herschman, M.E. Phelps, O.N. Witte, J. Czernin, and C.G. Radu. 2012. Nucleoside salvage pathway kinases regulate hematopoiesis by linking nucleotide metabolism with replication stress. *J Exp Med*. 209:2215-28.

Bartek, J., M. Mistrik, and J. Bartkova. 2012. Thresholds of replication stress signaling in cancer development and treatment. *Nature structural & molecular biology*. 19:5-7.

Boulos, N., H.L. Mulder, C.R. Calabrese, J.B. Morrison, J.E. Rehg, M.V. Relling, C.J. Sherr, and R.T. Williams. 2011. Chemotherapeutic agents circumvent emergence of dasatinib-resistant BCR-ABL kinase mutations in a precise mouse model of Philadelphia chromosome-positive acute lymphoblastic leukemia. *Blood*. 117:3585-95.

Chiuten, D.F., P.H. Wiernik, D.S. Zaharko, and L. Edwards. 1980. Clinical phase I-II and pharmacokinetic study of high-dose thymidine given by continuous intravenous infusion. *Cancer Res*. 40:818-22.

Cohen, S., M. Megherbi, L.P. Jordheim, I. Lefebvre, C. Perigaud, C. Dumontet, and J. Guitton. 2009. Simultaneous analysis of eight nucleoside triphosphates in cell lines by liquid chromatography coupled with tandem mass spectrometry. *J Chromatogr B Analyt Technol Biomed Life Sci*. 877:3831-40.

Csapo, Z., G. Keszler, G. Safrany, T. Spasokoukotskaja, I. Talianidis, M. Staub, and M. Sasvari-Szekely. 2003. Activation of deoxycytidine kinase by gamma-irradiation and inactivation by hyperosmotic shock in human lymphocytes. *Biochem Pharmacol*. 65:2031-9.

Datta, N.S., D.S. Shewach, B.S. Mitchell, and I.H. Fox. 1989. Kinetic properties and inhibition of human T lymphoblast deoxycytidine kinase. *J Biol Chem*. 264:9359-64.

de Bono, J.S., and A. Ashworth. 2010. Translating cancer research into targeted therapeutics. *Nature*. 467:543-9.

Fong, P.C., D.S. Boss, T.A. Yap, A. Tutt, P. Wu, M. Mergui-Roelvink, P. Mortimer, H. Swaisland, A. Lau, M.J. O'Connor, A. Ashworth, J. Carmichael, S.B. Kaye, J.H. Schellens, and J.S. de Bono. 2009. Inhibition of poly(ADP-ribose) polymerase in tumors from BRCA mutation carriers. *The New England journal of medicine*. 361:123-34.

Hanahan, D., and R.A. Weinberg. 2011. Hallmarks of cancer: the next generation. *Cell*. 144:646-74.

Hastak, K., R.K. Paul, M.K. Agarwal, V.S. Thakur, A.R. Amin, S. Agrawal, R.M. Sramkoski, J.W. Jacobberger, M.W. Jackson, G.R. Stark, and M.L. Agarwal. 2008. DNA synthesis from unbalanced nucleotide pools causes limited DNA damage that triggers ATR-CHK1-dependent p53 activation. *Proc Natl Acad Sci U S A*. 105:6314-9.

Jain, M., R. Nilsson, S. Sharma, N. Madhusudhan, T. Kitami, A.L. Souza, R. Kafri, M.W. Kirschner, C.B. Clish, and V.K. Mootha. 2012. Metabolite profiling identifies a key role for glycine in rapid cancer cell proliferation. *Science*. 336:1040-4.

Jordheim, L.P., E. Cros, M.H. Gouy, C.M. Galmarini, S. Peyrottes, J. Mackey, C. Perigaud, and C. Dumontet. 2004. Characterization of a gemcitabine-resistant murine leukemic cell line: reversion of in vitro resistance by a mononucleotide prodrug. *Clin Cancer Res*. 10:5614-21.

Kamphorst, J.J., J. Fan, W. Lu, E. White, and J.D. Rabinowitz. 2011. Liquid chromatography-high resolution mass spectrometry analysis of fatty acid metabolism. *Anal Chem*. 83:9114-22.

Kufe, D.W., P. Beardsley, D. Karp, L. Parker, A. Rosowsky, G. Canellos, and E. Frei, 3rd. 1980. High-dose thymidine infusions in patients with leukemia and lymphoma. *Blood*. 55:580-9.

Kufe, D.W., M.M. Wick, S. Moschella, and P. Major. 1981. Effect of high-dose thymidine infusions in patients with mycosis fungoides. *Cancer*. 48:1513-6.

Luo, J., N.L. Solimini, and S.J. Elledge. 2009. Principles of cancer therapy: oncogene and non-oncogene addiction. *Cell*. 136:823-37.

Maddocks, O.D., C.R. Berkers, S.M. Mason, L. Zheng, K. Blyth, E. Gottlieb, and K.H. Vousden. 2012. Serine starvation induces stress and p53-dependent metabolic remodelling in cancer cells. *Nature*. 493:542-6.

Matsuoka, S., B.A. Ballif, A. Smogorzewska, E.R. McDonald, 3rd, K.E. Hurov, J. Luo, C.E. Bakalarski, Z. Zhao, N. Solimini, Y. Lerenthal, Y. Shiloh, S.P. Gygi, and S.J. Elledge. 2007. ATM and ATR substrate analysis reveals extensive protein networks responsive to DNA damage. *Science*. 316:1160-6.

Murphy, J.M., A.L. Armijo, J. Nomme, C.H. Lee, Q.A. Smith, Z. Li, D.O. Campbell, H.I. Liao, D.A. Nathanson, W.R. Austin, J.T. Lee, R. Darvish, L. Wei, J. Wang, Y. Su, R. Damoiseaux, S. Sadeghi, M.E. Phelps, H.R. Herschman, J. Czernin, A.N.

Alexandrova, M.E. Jung, A. Lavie, and C.G. Radu. 2013. Development of new deoxycytidine kinase inhibitors and noninvasive in vivo evaluation using positron emission tomography. *J Med Chem*. 56:6696-708.

Nomme, J., J.M. Murphy, Y. Su, N.D. Sansone, A.L. Armijo, S.T. Olson, C. Radu, and A. Lavie. 2014. Structural characterization of new deoxycytidine kinase inhibitors rationalizes the affinity-determining moieties of the molecules. *Acta Crystallogr D Biol Crystallogr*. 70:68-78.

O'Dwyer, P.J., S.A. King, D.F. Hoth, and B. Leyland-Jones. 1987. Role of thymidine in biochemical modulation: a review. *Cancer Res*. 47:3911-9.

Ooi, K., T. Ohkubo, M. Higashigawa, H. Kawasaki, and M. Sakurai. 1996. Increased deoxycytidine kinase activity by etoposide in L1210 murine leukemic cells. *Biol Pharm Bull*. 19:1382-3.

Radu, C.G., C.J. Shu, E. Nair-Gill, S.M. Shelly, J.R. Barrio, N. Satyamurthy, M.E. Phelps, and O.N. Witte. 2008. Molecular imaging of lymphoid organs and immune activation by positron emission tomography with a new [18F]-labeled 2'-deoxycytidine analog. *Nat Med*. 14:783-8.

Reichard, P. 1988. Interactions between deoxyribonucleotide and DNA synthesis. *Annu. Rev. Biochem.* 57:349-374.

Schoppy, D.W., R.L. Ragland, O. Gilad, N. Shastri, A.A. Peters, M. Murga, O. Fernandez-Capetillo, J.A. Diehl, and E.J. Brown. 2012. Oncogenic stress sensitizes murine cancers to hypomorphic suppression of ATR. *The Journal of clinical investigation*. 122:241-52.

Schwarzenberg, J., C.G. Radu, M. Benz, B. Fueger, A.Q. Tran, M.E. Phelps, O.N. Witte, N. Satyamurthy, J. Czernin, and C. Schiepers. 2011. Human biodistribution and radiation dosimetry of novel PET probes targeting the deoxyribonucleoside salvage pathway. *European journal of nuclear medicine and molecular imaging*. 38:711-21.

Shields, A.F., J.R. Grierson, B.M. Dohmen, H.J. Machulla, J.C. Stayanoff, J.M. Lawhorn-Crews, J.E. Obradovich, O. Muzik, and T.J. Mangner. 1998. Imaging proliferation in vivo with [F-18]FLT and positron emission tomography. *Nature medicine*. 4:1334-6.

Shu, C.J., D.O. Campbell, J.T. Lee, A.Q. Tran, J.C. Wengrod, O.N. Witte, M.E. Phelps, N. Satyamurthy, J. Czernin, and C.G. Radu. 2010. Novel PET probes specific for deoxycytidine kinase. *J Nucl Med*. 51:1092-8.

Stella, V.J., and Q. He. 2008. Cyclodextrins. *Toxicologic pathology*. 36:30-42.

Tannous, B.A. 2009. Gaussia luciferase reporter assay for monitoring biological processes in culture and in vivo. *Nat Protoc*. 4:582-91.

Toy, G., W.R. Austin, H.I. Liao, D. Cheng, A. Singh, D.O. Campbell, T.O. Ishikawa, L.W. Lehmann, N. Satyamurthy, M.E. Phelps, H.R. Herschman, J. Czernin, O.N. Witte, and C.G. Radu. 2010. Requirement for deoxycytidine kinase in T and B lymphocyte development. *Proc Natl Acad Sci U S A*. 107:5551-6.

Vander Heiden, M.G. 2011. Targeting cancer metabolism: a therapeutic window opens. *Nat Rev Drug Discov*. 10:671-84.

Warburg, O., F. Wind, and E. Negelein. 1927. The Metabolism of Tumors in the Body. *The Journal of general physiology*. 8:519-30.

Williams, R.T., M.F. Roussel, and C.J. Sherr. 2006. Arf gene loss enhances oncogenicity and limits imatinib response in mouse models of Bcr-Abl-induced acute lymphoblastic leukemia. *Proc Natl Acad Sci U S A*. 103:6688-93.

Xu, Y.Z., P. Huang, and W. Plunkett. 1995. Functional compartmentation of dCTP pools. Preferential utilization of salvaged deoxycytidine for DNA repair in human lymphoblasts. *J Biol Chem*. 270:631-7.

Yang, C., M. Lee, J. Hao, X. Cui, X. Guo, C. Smal, F. Bontemps, S. Ma, X. Liu, D. Engler, W.B. Parker, and B. Xu. 2012. Deoxycytidine kinase regulates the G2/M checkpoint through interaction with cyclin-dependent kinase 1 in response to DNA damage. *Nucleic Acids Res*. 40:9621-32.

Yu, X.-C., M. Miranda, Z. Liu, S. Patel, N. Nguyen, K. Carson, Q. Liu, and J.C. Swaffield. 2010. Novel Potent Inhibitors of Deoxycytidine Kinase Identified and Compared by Multiple Assays. *J. Biomol. Screening*. 15:72-79.

Austin, W.R., A.L. Armijo, D.O. Campbell, A.S. Singh, T. Hsieh, D. Nathanson, H.R. Herschman, M.E. Phelps, O.N. Witte, J. Czernin, and C.G. Radu. 2012. Nucleoside salvage pathway kinases regulate hematopoiesis by linking nucleotide metabolism with replication stress. *The Journal of experimental medicine* 209:2215-2228.

Bartek, J., M. Mistrik, and J. Bartkova. 2012. Thresholds of replication stress signaling in cancer development and treatment. *Nat Struct Mol Biol* 19:5-7.

Boulos, N., H.L. Mulder, C.R. Calabrese, J.B. Morrison, J.E. Rehg, M.V. Relling, C.J. Sherr, and R.T. Williams. 2011. Chemotherapeutic agents circumvent emergence of dasatinib-resistant BCR-ABL kinase mutations in a precise mouse model of Philadelphia chromosome-positive acute lymphoblastic leukemia. *Blood* 117:3585-3595.

Chiuten, D.F., P.H. Wiernik, D.S. Zaharko, and L. Edwards. 1980. Clinical phase I-II and pharmacokinetic study of high-dose thymidine given by continuous intravenous infusion. *Cancer research* 40:818-822.

Cohen, S., M. Megherbi, L.P. Jordheim, I. Lefebvre, C. Perigaud, C. Dumontet, and J. Guitton. 2009. Simultaneous analysis of eight nucleoside triphosphates in cell lines by liquid chromatography coupled with tandem mass spectrometry. *J Chromatogr B Analyt Technol Biomed Life Sci* 877:3831-3840.

Csapo, Z., G. Keszler, G. Safrany, T. Spasokoukotskaja, I. Talianidis, M. Staub, and M. Sasvari-Szekely. 2003. Activation of deoxycytidine kinase by gamma-irradiation and inactivation by hyperosmotic shock in human lymphocytes. *Biochem Pharmacol* 65:2031-2039.

Datta, N.S., D.S. Shewach, B.S. Mitchell, and I.H. Fox. 1989. Kinetic properties and inhibition of human T lymphoblast deoxycytidine kinase. *J Biol Chem* 264:9359-9364.

de Bono, J.S., and A. Ashworth. 2010. Translating cancer research into targeted therapeutics. *Nature* 467:543-549.

Fong, P.C., D.S. Boss, T.A. Yap, A. Tutt, P. Wu, M. Mergui-Roelvink, P. Mortimer, H. Swaisland, A. Lau, M.J. O'Connor, A. Ashworth, J. Carmichael, S.B. Kaye, J.H. Schellens, and J.S. de Bono. 2009. Inhibition of poly(ADP-ribose) polymerase in tumors from BRCA mutation carriers. *N Engl J Med* 361:123-134.

Hanahan, D., and R.A. Weinberg. 2011. Hallmarks of cancer: the next generation. *Cell* 144:646-674.

Hastak, K., R.K. Paul, M.K. Agarwal, V.S. Thakur, A.R. Amin, S. Agrawal, R.M. Sramkoski, J.W. Jacobberger, M.W. Jackson, G.R. Stark, and M.L. Agarwal. 2008. DNA synthesis from unbalanced nucleotide pools causes limited DNA damage that triggers ATR-CHK1-dependent p53 activation. *Proc Natl Acad Sci U S A* 105:6314-6319.

Jain, M., R. Nilsson, S. Sharma, N. Madhusudhan, T. Kitami, A.L. Souza, R. Kafri, M.W. Kirschner, C.B. Clish, and V.K. Mootha. 2012. Metabolite profiling identifies a key role for glycine in rapid cancer cell proliferation. *Science* 336:1040-1044.

Jordheim, L.P., E. Cros, M.H. Gouy, C.M. Galmarini, S. Peyrottes, J. Mackey, C. Perigaud, and C. Dumontet. 2004. Characterization of a gemcitabine-resistant murine leukemic cell line: reversion of in vitro resistance by a mononucleotide prodrug. *Clin Cancer Res* 10:5614-5621.

Kamphorst, J.J., J. Fan, W. Lu, E. White, and J.D. Rabinowitz. 2011. Liquid chromatography-high resolution mass spectrometry analysis of fatty acid metabolism. *Anal Chem* 83:9114-9122.

Kufe, D.W., P. Beardsley, D. Karp, L. Parker, A. Rosowsky, G. Canellos, and E. Frei, 3rd. 1980. High-dose thymidine infusions in patients with leukemia and lymphoma. *Blood* 55:580-589.

Kufe, D.W., M.M. Wick, S. Moschella, and P. Major. 1981. Effect of high-dose thymidine infusions in patients with mycosis fungoides. *Cancer* 48:1513-1516.

Luo, J., N.L. Solimini, and S.J. Elledge. 2009. Principles of cancer therapy: oncogene and non-oncogene addiction. *Cell* 136:823-837.

Maddocks, O.D., C.R. Berkers, S.M. Mason, L. Zheng, K. Blyth, E. Gottlieb, and K.H. Vousden. 2012. Serine starvation induces stress and p53-dependent metabolic remodelling in cancer cells. *Nature* 493:542-546.

Matsuoka, S., B.A. Ballif, A. Smogorzewska, E.R. McDonald, 3rd, K.E. Hurov, J. Luo, C.E. Bakalarski, Z. Zhao, N. Solimini, Y. Lerenthal, Y. Shiloh, S.P. Gygi, and S.J. Elledge. 2007. ATM and ATR substrate analysis reveals extensive protein networks responsive to DNA damage. *Science* 316:1160-1166.

Murphy, J.M., A.L. Armijo, J. Nomme, C.H. Lee, Q.A. Smith, Z. Li, D.O. Campbell, H.I. Liao, D.A. Nathanson, W.R. Austin, J.T. Lee, R. Darvish, L. Wei, J. Wang, Y. Su, R. Damoiseaux, S. Sadeghi, M.E. Phelps, H.R. Herschman, J. Czernin, A.N. Alexandrova, M.E. Jung, A. Lavie, and C.G. Radu. 2013. Development of new deoxycytidine kinase inhibitors and noninvasive in vivo evaluation using positron emission tomography. *Journal of medicinal chemistry* 56:6696-6708.

Nomme, J., J.M. Murphy, Y. Su, N.D. Sansone, A.L. Armijo, S.T. Olson, C. Radu, and A. Lavie. 2014. Structural characterization of new deoxycytidine kinase inhibitors rationalizes the affinity-determining moieties of the molecules. *Acta crystallographica. Section D, Biological crystallography* 70:68-78.

O'Dwyer, P.J., S.A. King, D.F. Hoth, and B. Leyland-Jones. 1987. Role of thymidine in biochemical modulation: a review. *Cancer research* 47:3911-3919.

Ooi, K., T. Ohkubo, M. Higashigawa, H. Kawasaki, and M. Sakurai. 1996. Increased deoxycytidine kinase activity by etoposide in L1210 murine leukemic cells. *Biol Pharm Bull* 19:1382-1383.

Radu, C.G., C.J. Shu, E. Nair-Gill, S.M. Shelly, J.R. Barrio, N. Satyamurthy, M.E. Phelps, and O.N. Witte. 2008. Molecular imaging of lymphoid organs and immune activation by positron emission tomography with a new [18F]-labeled 2'-deoxycytidine analog. *Nat Med* 14:783-788.

Reichard, P. 1988. Interactions between deoxyribonucleotide and DNA synthesis. *Annu. Rev. Biochem.* 57:349-374.

Schoppy, D.W., R.L. Ragland, O. Gilad, N. Shastri, A.A. Peters, M. Murga, O. Fernandez-Capetillo, J.A. Diehl, and E.J. Brown. 2012. Oncogenic stress sensitizes murine cancers to hypomorphic suppression of ATR. *J Clin Invest* 122:241-252.

Schwarzenberg, J., C.G. Radu, M. Benz, B. Fueger, A.Q. Tran, M.E. Phelps, O.N. Witte, N. Satyamurthy, J. Czernin, and C. Schiepers. 2011. Human biodistribution and radiation dosimetry of novel PET probes targeting the deoxyribonucleoside salvage pathway. *Eur J Nucl Med Mol Imaging* 38:711-721.

Shields, A.F., J.R. Grierson, B.M. Dohmen, H.J. Machulla, J.C. Stayanoff, J.M. Lawhorn-Crews, J.E. Obradovich, O. Muzik, and T.J. Mangner. 1998. Imaging proliferation in vivo with [F-18]FLT and positron emission tomography. *Nature medicine* 4:1334-1336.

Shu, C.J., D.O. Campbell, J.T. Lee, A.Q. Tran, J.C. Wengrod, O.N. Witte, M.E. Phelps, N. Satyamurthy, J. Czernin, and C.G. Radu. 2010. Novel PET probes specific for deoxycytidine kinase. *J Nucl Med* 51:1092-1098.

Stella, V.J., and Q. He. 2008. Cyclodextrins. *Toxicol Pathol* 36:30-42.

Tannous, B.A. 2009. Gaussia luciferase reporter assay for monitoring biological processes in culture and in vivo. *Nat Protoc* 4:582-591.

Toy, G., W.R. Austin, H.I. Liao, D. Cheng, A. Singh, D.O. Campbell, T.O. Ishikawa, L.W. Lehmann, N. Satyamurthy, M.E. Phelps, H.R. Herschman, J. Czernin, O.N. Witte, and C.G. Radu. 2010. Requirement for deoxycytidine kinase in T and B lymphocyte development. *Proc Natl Acad Sci U S A* 107:5551-5556.

Vander Heiden, M.G. 2011. Targeting cancer metabolism: a therapeutic window opens. *Nat Rev Drug Discov* 10:671-684.

Warburg, O., F. Wind, and E. Negelein. 1927. The Metabolism of Tumors in the Body. *J Gen Physiol* 8:519-530.

Williams, R.T., M.F. Roussel, and C.J. Sherr. 2006. Arf gene loss enhances oncogenicity and limits imatinib response in mouse models of Bcr-Abl-induced acute lymphoblastic leukemia. *Proc Natl Acad Sci U S A* 103:6688-6693.

Xu, Y.Z., P. Huang, and W. Plunkett. 1995. Functional compartmentation of dCTP pools. Preferential utilization of salvaged deoxycytidine for DNA repair in human lymphoblasts. *J Biol Chem* 270:631-637.

Yang, C., M. Lee, J. Hao, X. Cui, X. Guo, C. Smal, F. Bontemps, S. Ma, X. Liu, D. Engler, W.B. Parker, and B. Xu. 2012. Deoxycytidine kinase regulates the G2/M checkpoint through interaction with cyclin-dependent kinase 1 in response to DNA damage. *Nucleic Acids Res* 40:9621-9632.

Yu, X.-C., M. Miranda, Z. Liu, S. Patel, N. Nguyen, K. Carson, Q. Liu, and J.C. Swaffield. 2010. Novel Potent Inhibitors of Deoxycytidine Kinase Identified and Compared by Multiple Assays. *J. Biomol. Screening* 15:72-79.

CHAPTER 5:

Conclusions

A complete understanding of the molecular mechanisms for DNA metabolism used in both normal and malignant cells is important for the development of new therapeutic strategies. In this study, we began by investigating the mechanism by which dCK contributes to the dNTP pools for DNA replication and repair in both normal and malignant hematopoietic cells. The findings of our work address an enigmatic understanding of the intricate relationship that exists between the *de novo* pathway and the nucleoside salvage pathway.

Contrary to the notion that the salvage pathway functioned only in a limited capacity to fine tune the nucleotide pools (Bianchi et al., 1986; Bianchi et al., 1987; Nicander and Reichard, 1985; Reichard, 1988) our observations indicate that dCK is vital for balanced dCTP levels. In the absence of dCK, dCTP pools are depleted in hematopoietic precursors resulting in nucleotide replication stress, cell cycle arrest, and blocked differentiation. dCK functions to counteract the inhibitory effects of dTTP on RNR via the salvage of thymidine by TK1. The results of these studies have provided valuable insight into possible therapeutic interventions of dCTP synthesis required for DNA synthesis.

Previous pre-clinical (Lockshin et al., 1985) and clinical (Blumenreich et al., 1984; Chiuten et al., 1980; Kufe et al., 1980) studies have investigated thymidine infusions as a potential therapeutic agent in the treatment of leukemias and lymphomas. Despite the tolerable and reversible side effects, therapeutic responses were limited, due to the ability of dCK to contribute to the thymidine-induced depleted dCTP pools. We hypothesized that successful thymidine therapy would require pharmacological inhibition of dCK to prevent the dCK-mediated rescue of the thymidine block of *de novo*

dCTP synthesis. To test our hypothesis we successfully developed small molecule inhibitors of dCK and evaluated the co-targeting of both *de novo* and salvage dCTP synthesis in acute lymphoblastic leukemia. With the aid of PET, we were able to non-invasively evaluate the efficacy of the inhibitors *in vivo* both during the development of the inhibitor and the therapeutic targeting of the tumors. Our studies provide further support for the utilization of imaging in the drug discovery and development process by non-invasively evaluating the drug pharmacodynamic and pharmacokinetic properties *in vivo.* In addition, our described PET assays would be available for use in future clinical trials to assess dCK inhibition in target tissues as the biomarkers have already been approved for use in humans (Schwarzenberg et al., 2011).

While we have demonstrated that the salvage pathway plays a critical role in providing dNTPs for DNA replication in lymphoid and erythroid precursors and some malignant hematological cells, it remains unclear what contributions the salvage pathway plays in mature lymphocytes. Future studies will also be required to determine the clinical applicability of the use of dCK inhibitors in the treatment of nucleotide metabolism disorders, such as adenosine deaminase deficiency (ADA). A dCK inhibitor in combination with an adenosine kinase inhibitor may prevent the deoxyadenosine-induced cell death responsible for the compromised immune system.

The studies presented in this dissertation provide strong evidence for the use of a dCKi in the treatment of hematological malignancies in the clinic. However, prior to the translation of the dCKi into the clinic further development of the inhibitor is necessary to improve the pharmacokinetic properties. Crystal structures of dCK with our inhibitors guided our efforts in the development of small molecule inhibitors with nanomolar

affinity for dCK. Unfortunately, our lead compounds demonstrate low metabolic stability when tested in a liver microsomal assay and pharmacokinetic studies in mice. Additional modifications to the current lead compounds that improve the metabolic stability while maintaining the binding affinity will be needed for utilization of such inhibitors in the clinic.

References

Bianchi, V., E. Pontis, and P. Reichard. 1986. Interrelations between substrate cycles and de novo synthesis of pyrimidine deoxyribonucleoside triphosphates in 3T6 cells. *Proceedings of the National Academy of Sciences of the United States of America* 83:986-990.

Bianchi, V., E. Pontis, and P. Reichard. 1987. Regulation of pyrimidine deoxyribonucleotide metabolism by substrate cycles in dCMP deaminase-deficient V79 hamster cells. *Molecular and cellular biology* 7:4218-4224.

Blumenreich, M.S., T.M. Woodcock, M. Andreeff, W. Hiddemann, T.C. Chou, K. Vale, M. O'Hehir, B.D. Clarkson, and C.W. Young. 1984. Effect of very high-dose thymidine infusions on leukemia and lymphoma patients. *Cancer research* 44:2203-2207.

Chiuten, D.F., P.H. Wiernik, D.S. Zaharko, and L. Edwards. 1980. Clinical phase I-II and pharmacokinetic study of high-dose thymidine given by continuous intravenous infusion. *Cancer research* 40:818-822.

Kufe, D.W., P. Beardsley, D. Karp, L. Parker, A. Rosowsky, G. Canellos, and E. Frei, 3rd. 1980. High-dose thymidine infusions in patients with leukemia and lymphoma. *Blood* 55:580-589.

Lockshin, A., B.C. Giovanella, J.S. Stehlin, Jr., T. Kozielski, C. Quian, and R.W. Apperson. 1985. Antitumor activity and minimal toxicity of concentrated thymidine infused in nude mice. *Cancer research* 45:1797-1802.

Nicander, B., and P. Reichard. 1985. Evidence for the involvement of substrate cycles in the regulation of deoxyribonucleoside triphosphate pools in 3T6 cells. *The Journal of biological chemistry* 260:9216-9222.

Reichard, P. 1988. Interactions between deoxyribonucleotide and DNA synthesis. *Annual review of biochemistry* 57:349-374.

Schwarzenberg, J., C.G. Radu, M. Benz, B. Fueger, A.Q. Tran, M.E. Phelps, O.N. Witte, N. Satyamurthy, J. Czernin, and C. Schiepers. 2011. Human biodistribution and radiation dosimetry of novel PET probes targeting the deoxyribonucleoside salvage pathway. *European journal of nuclear medicine and molecular imaging* 38:711-721.